THE UNIVERSITY OF QUEENSLAND

AUSTRALIA

Real-time optical imaging of the liver:

diagnosis and prediction of treatment response

Haolu Wang

Master of Surgery, Bachelor of Medicine

A thesis submitted for the degree of Doctor of Philosophy at

The University of Queensland in 2017

School of Medicine

Abstract

Multiphoton microscopy (MPM) has become increasingly popular and widely used in both basic and clinical liver studies over the past few years. The fluorescence lifetime imaging (FLIM) can be coupled with MPM to add additional quantitation and specificity to the detection of endogenous fluorescent species in the liver as well as exogenous molecules, nanoparticles and therapeutic cells that applied to the liver both *in vitro* and *in vivo*. These technologies provide deep penetration of live tissues with less photobleaching and phototoxicity, and help our better understanding of the cellular morphology, microenvironment, immune responses and spatiotemporal dynamics of drugs and therapeutic cells in the healthy and diseased liver.

Taking advantages of MPM-FLIM, the aim of this project is to develop novel optical imaging methods for diagnosis and prediction of treatment response in liver diseases. The main achievements obtained in this thesis are listed as below:

(1) Conventional histology with light microscopy is essential in the diagnosis of most liver diseases. Recently, a concept of real-time histology with optical biopsy has been advocated. Live mice livers (normal, with fibrosis, steatosis, hepatocellular carcinoma and ischemia-reperfusion injury) were imaged by MPM-FLIM for stain-free real-time histology. The acquired MPM-FLIM images were compared with conventional histological images. MPM-FLIM imaged subsurface cellular and subcellular histopathological hallmarks of live liver in mice models at high resolution. Additional information such as distribution of stellate cell associated autofluorescence and fluorescence lifetime changes was also gathered by MPM-FLIM simultaneously, which cannot be obtained from conventional histology. MPM-FLIM could visualise the cell morphology and microenvironment changes in diseased livers without conventional biopsy or administration of fluorescent dyes.

(2) Oxidative stress reflects an imbalance between reactive oxygen species (ROS) and antioxidants, which has been reported as an early unifying event in the development and progression of various diseases and as a direct and mechanistic indicator of treatment response. A transition-metal complex-based sensing platform was developed for *in vivo* MPM-FLIM imaging of oxidative stress at a single cell resolution. By combining fluorescence intensity and fluorescence lifetime imaging, this sensing platform accurately localised ROS and glutathione (GSH) within the liver, and quantified their changes during liver injury. This precedes changes in conventional biochemical and histological

assessments. Importantly, the optical oxidative stress index (OSI), expressed as the fluorescence intensity ratio of ROS and GSH probes, has significant implications for sensitive, spatially configured and quantitative assessment of metabolic status and drug response, which could reveal mechanistic insights and accelerate drug development studies.

(3) Although mesenchymal stem cells (MSCs) present a promising tool in cell therapy for the treatment of liver cirrhosis, the *in vivo* distribution of administered MSCs has still been poorly understood, which hampers the precise prediction and evaluation of their therapeutic efficacy. The spatiotemporal disposition of administered MSCs in the liver was directly visualized using MPM and the cell quantity was assessed using flow cytometry. A physiologically based kinetic model was developed to characterise the *in vivo* distribution of MSCs. This model was further validated with multiple external datasets, indicating potential inter-route and inter-species predictive capability. The results suggest that the targeting efficiency of MSCs is determined by the lung retention and interaction between MSCs and target organs, including cell arrest, depletion and release. By adapting specific parameters, this model can be easily applied to abnormal conditions or other types of circulating cells for designing treatment protocols and guiding future experiments.

Declaration by author

This thesis is composed of my original work, and contains no material previously published or written by another person except where due reference has been made in the text. I have clearly stated the contribution by others to jointly-authored works that I have included in my thesis.

I have clearly stated the contribution of others to my thesis as a whole, including statistical assistance, survey design, data analysis, significant technical procedures, professional editorial advice, and any other original research work used or reported in my thesis. The content of my thesis is the result of work I have carried out since the commencement of my research higher degree candidature and does not include a substantial part of work that has been submitted to qualify for the award of any other degree or diploma in any university or other tertiary institution. I have clearly stated which parts of my thesis, if any, have been submitted to qualify for another award.

I acknowledge that an electronic copy of my thesis must be lodged with the University Library and, subject to the policy and procedures of The University of Queensland, the thesis be made available for research and study in accordance with the Copyright Act 1968 unless a period of embargo has been approved by the Dean of the Graduate School.

I acknowledge that copyright of all material contained in my thesis resides with the copyright holder(s) of that material. Where appropriate I have obtained copyright permission from the copyright holder to reproduce material in this thesis.

Publications during candidature

Peer-reviewed papers

1. **Wang H**, Liang X, Gravot G, Thorling C, Crawford D, Xu ZP, Liu X, Roberts M. Visualizing liver anatomy, physiology and pharmacology using multiphoton microscopy. ***J Biophotonics***. 2017; 10(1):46-60.

2. **Wang H**, Zhang R, Bridle K, Jayachandran A, Thomas J, Zhang W, Yuan J, Xu ZP, Crawford D, Liang X, Liu X, Roberts M: Two-photon dual imaging platform for in vivo monitoring cellular oxidative stress in liver injury. ***Sci Rep***. 2017; 7: 45374.

3. **Wang H**, Liang X, Xu ZP, Crawford D, Liu X, Roberts M: A physiologically based kinetic model for elucidating the in vivo distribution of administered mesenchymal stem cells. ***Sci Rep***. 2016; 6: 22293.

4. Liang X, **Wang H***, Grice JE, Li L, Liu X, Xu ZP, Roberts M: Physiologically based pharmacokinetic model for long-circulating inorganic nanoparticles. ***Nano Lett***. 2016; 16(2):939-45 *co-first authors.

5. **Wang H**, Thorling C, Liang X, Bridle K, Grice J, Zhu Y, Crawford D, Xu ZP, Liu X, Roberts M. Diagnostic imaging and therapeutic application of nanoparticles targeting to the liver. ***J Mater Chem B***. 2015, 3, 939.

6. **Wang H**, Liang X, Mohammed Y, Thomas J, Bridle K, Thorling C, Grice J, Xu ZP, Liu X, Crawford D, Roberts M. Real-time histology in liver disease using multiphoton microscopy with fluorescence lifetime imaging. ***Biomed Opt Express***. 2015; 6(3):780-92.

7. Liang X, **Wang H**, Zhu Y, Zhang R, Cogger VC, Liu X, Xu ZP, Grice JE, Roberts MS: Short- and long-term tracking of anionic ultrasmall nanoparticles in kidney. ***ACS Nano***. 2016; 10(1):387-95.

8. Macklin R, **Wang H**, Loo D, Martin S, Cumming A, Cai N, Lane R, Ponce NS, Topkas E, Inder K, Saunders NA, Endo-Munoz L: Extracellular vesicles secreted by highly metastatic clonal variants of osteosarcoma preferentially localize to the lungs and induce metastatic behaviour in poorly metastatic clones. ***Oncotarget***. 2016; 7(28):43570-43587

9. Zhang F, Liang X, Zhang W, Wang YL, **Wang H**, Mohammed YH, Song B, Zhang R, Yuan J: A unique iridium(III) complex-based chemosensor for multi-signal detection and multi-channel imaging of hypochlorous acid in liver injury. ***Biosens Bioelectron***. 2017; 15;87:1005-1011

10. Ni Q, **Wang H**, Zhang Y, Qian L, Chi J, Liang X, Chen T, Wang J: MDCT assessment of resectability in hilar cholangiocarcinoma. ***Abdom Radiol (NY)***. 2016 Oct 21; [Epub ahead of print].

Book Chapters

1. Liu X, **Wang H**, Liang X, Roberts M: Hepatic Metabolism in Liver Health and Disease. Liver Pathophysiology. Elsevier. 2017.

2. Holmes A, Thorling C, Liang X, **Wang H**, Breunig H, Studier H, Roberts M: Revealing interaction of dyes and nanomaterials with organs by imaging. DeGruyter. 2016.

Conference Abstracts

1. **Wang H**, Endo-Munoz L, Weijs L, Liang X, Liu X, Crawford D, Roberts M: A physiologically based kinetic model to characterize and predict the biological fate of circulating tumor cells *in vivo*. ***Eur J Cancer***. 2015, S133.

2. **Wang H**, Liang X, Endo-Munoz L, Weijs L, Liu X, Crawford D, Roberts M: A physiologically based kinetic model to characterize and predict the biological fate of mesenchymal stem cells *in vivo*. ***J Gastroenterol Hepatol***. 2015, 3, 11.

3. **Wang H**, Jayachandran A, Gravot G, Liang X, Thorling C, Zhang R, Liu X, Roberts M: *In vivo* quantitative visualization of hypochlorous acid in the liver using a novel selective two-photon fluorescent probe. ***Proceedings of SPIE***. 2016, 100131G.

4. **Wang H**, Zhang R, Bridle K, Jayachandran A, Thomas J, Xu ZP, Crawford D, Liang X, Liu X, Roberts M. A novel imaging platform to quantitatively measure *in vivo* cellular ROS in the liver. United European Gastroenterology Week. Vienna, Austria, 2016.

5. Liang X, **Wang H**, Zhu Y, Grice J, Liu X, Xu Z, Roberts M. Early diagnosis of hepatocellular carcinoma by *in vivo* imaging. ***Eur J Cancer***. 2015, 51, S129–S130.

6. Liang X, **Wang H**, Liu X, Roberts M. Quantitative optical imaging of paracetamol-induced metabolism changes in the liver. ***Proceedings of SPIE***. 2016, 100131H.

7. Liu X, Liang X, **Wang H**, Roberts D, Roberts M. Multiphoton imaging for assessing renal disposition in acute kidney injury. ***Proceedings of SPIE***. 2016, 100131F.

8. Liu X, Liang X, **Wang H**, Roberts M. Developing novel mechanistic markers for managing paracetamol-induced hepatotoxicity. ASCEPT-MPGPCR Joint Scientific Meeting. Clinical Pharmacology Workshop. Melbourne, VIC, Australia, 2016.

Publications included in this thesis

1. **Wang H**, Liang X, Gravot G, Thorling C, Crawford D, Xu ZP, Liu X, Roberts M. Visualizing liver anatomy, physiology and pharmacology using multiphoton microscopy. ***J Biophotonics***. 2017; 10(1):46-60.

– incorporated as Chapter 2.

Contributor	Statement of contribution
Author: Haolu Wang	Literature search (80%) Wrote the paper (70%)
Author: Germain Gravot	Literature search (15%)
Author: Xiaowen Liang and Camilla Thorling	Literature search (5%) Wrote the paper and revised the manuscript (15%)
Author: Darrell Crawford, Zhi Ping Xu, Xin Liu and Michael Roberts	Gave comments and revised the manuscript (15%)

2. **Wang H**, Liang X, Mohammed Y, Thomas J, Bridle K, Thorling C, Grice J, Xu ZP, Liu X, Crawford D, Roberts M. Real-time histology in liver disease using multiphoton microscopy with fluorescence lifetime imaging. ***Biomed Opt Express***. 2015; 6(3):780-92.

– Incorporated as Chapter 3.

Contributor	Statement of contribution
Author: Haolu Wang	Designed experiments (80%) Animal experiments (80%) Wrote the paper (60%)
Author: Xiaowen Liang and James Thomas	Wrote the paper and revised the manuscript (20%)
Author: Zhi Ping Xu, Jeff Grice and Michael Roberts	Designed experiments (20%) Gave comments and revised the manuscript (10%)
Author: Kim Bridle	Analysed histology results
Author: Xin Liu and Darrell Crawford	Gave comments and revised the manuscript (10%)

Author: Camilla Thorling and Yousuf Mohammed	Animal experiments (20%)

3. **Wang H**, Zhang R, Bridle K, Jayachandran A, Thomas J, Zhang W, Yuan J, Xu ZP, Crawford D, Liang X, Liu X, Roberts M: Two-photon dual imaging platform for in vivo monitoring cellular oxidative stress in liver injury. ***Sci Rep***. 2017; 7: 45374.
– incorporated as Chapter 4.

Contributor	Statement of contribution
Author: Haolu Wang	Designed experiments (70%) Animal experiments (60%) Wrote the paper (60%)
Author: Run Zhang and Wenzhu Zhang	Prepared probes
Author: Xiaowen Liang, Aparna Jayachandran and James Thomas	Animal experiments (40%) Wrote the paper and revised the manuscript (15%)
Author: Xiaowen Liang, Zhi Ping Xu, Jingli Yuan and Michael Roberts	Designed experiments (30%) Gave comments and revised the manuscript (15%)
Author: Kim R. Bridle, Xin Liu and Darrell Crawford	Analysed histology results Gave comments and revised the manuscript (10%)

4. **Wang H**, Liang X, Xu ZP, Crawford D, Liu X, Roberts M: A physiologically based kinetic model for elucidating the *in vivo* distribution of administered mesenchymal stem cells. ***Sci Rep***. 2016; 6: 22293.
– incorporated as Chapter 5.

Contributor	Statement of contribution
Author: Haolu Wang	Designed experiments (90%) Developed models (70%) Wrote the paper (70%)
Author: Xiaowen Liang	Developed models (10%)
Author: Zhi Ping Xu	Wrote the paper and revised the

	manuscript (10%)
Author: Darrell Crawford and Michael Roberts	Gave comments and revised the manuscript (10%)
Author: Xin Liu	Developed models (20%) Wrote the paper (10%)

Contributions by others to the thesis

Dr Xin Liu, my principal advisor, gave continuous guidance and instructions on the direction of the research, and provided detailed comments and valuable suggestions on all the works presented in this thesis and publications.

Prof Darrell Crawford, A/Prof Zhi Ping Xu and Prof Michael Roberts as the associate advisors, provided constant help with my research knowledge, and generous support, advice and guidance in this thesis.

Statement of parts of the thesis submitted to qualify for the award of another degree

None

Acknowledgements

My deepest gratitude goes first and foremost to Dr Xin Liu, my principal advisor, who has illuminated me and led me into the field of advanced imaging. I would also like to thank Prof Darrell Crawford, A/Prof Zhi Ping Xu and Prof Michael Roberts for their serving on my advisor team and constant guidance through all the stage of my PhD study.

I would like to express my gratitude to Dr Kim Bridle and Dr Jason Steel for their expert advice and for serving on the review panel of all my PhD milestones. My sincere appreciation also goes to my colleagues in Therapeutics Research Centre and Gallipoli Medical Research Institute, Dr Camilla Thompson, Dr Yousuf Mohammed and Dr Aparna Jayachandrand for their fabulous and unwavering support.

I owe special thanks to the University of Queensland and National Health and Medical Research Council for sponsoring my research. I also would like to acknowledge Dr James Thomas for his kind advice to my research project as a clinical scientist and hepatology specialist. I am grateful for Dr Liesbeth Weijs and A/Prof Mike Doran, whose contributions to the modelling of stem cells described herein were invaluable. I wish we can continue our collaboration after my graduation.

Last but not least, I would like to express my deepest appreciation to my parents, for their forever encouragement, inspiration, and support in pursuing my PhD. Thanks to my wife, our mutual interest acted as the stimulus for me to devote into medical research in the past three years.

This thesis is dedicated to my late grandfather, Prof Zhichang Lu, Department of Mathematics, Jilin University, who enlightened me with a taste of the Pierian Spring. So I drink deep.

Keywords

Liver, multiphoton microscopy, fluorescence lifetime imaging, diagnosis, therapeutics, modelling

Australian and New Zealand Standard Research Classifications (ANZSRC)

ANZSRC code: 110307 Gastroenterology and Hepatology, 45%
ANZSRC code: 020503 Nonlinear Optics and Spectroscopy, 30%
ANZSRC code: 111501 Basic Pharmacology, 25%

Fields of Research (FoR) Classification

FoR code: 1103 Clinical sciences (Hepatology), 45%
FoR code: 0205 Optical physics, 30%
FoR code: 1115 Pharmacology and Pharmaceutical Sciences, 25%

Table of Contents

List of Figures

List of Tables

List of Abbreviations used in the thesis

3MLCT	Triplet state of metal-to-ligand charge transfer
ALT	Alanine aminotransferase
APAP	Acetaminophen
CCl_4	Carbon tetrachloride
CARS	Coherent anti-Stokes Raman scattering
CF	Fluorogenic carboxyfluorescein
CFDA	Carboxyfluorescein diacetate
CIs	Confidence intervals
CLSM	Confocal Laser Scanning Microscopy
CT	Computed tomography
ERCP	Endoscopic retrograde cholangiopancreatography
FAD	Flavin adenine dinucleotide
FG	Fluorescein mono-glucuronide
FLIM	Fluorescence lifetime imaging
GFP	Green fluorescent protein
GSH	Glutathione
H_2O_2	Hydrogen peroxide
HCC	Hepatocellular carcinoma
H&E	Hematoxylin & Eosin
HOCl	Hypochlorous acid

ICP-MS	Inductively coupled plasma-mass spectrometry
I/R	Ischemia-reperfusion
LAURDAN	6-lauroyl-2-dimethylaminonaphthalene
MAPE	Mean absolute prediction error
MDR1	P-glycoprotein
MI	Myocardial infarction
MPE	Mean prediction error
MPM	Multiphoton microscopy
MPT	Mitochondrial permeability transition
MRI	Magnetic resonance imaging
MSCs	Mesenchymal stem cells
NADH	Nicotinamide adenine dinucleotide
NPs	Nanoparticles
Oatp	Organic anion transporting polypeptide
OSI	Oxidative stress index
PBK	Physiologically based kinetic
PBPK	Physiologically based pharmacokinetic
P-GSH	GSH-detection probe
P-HA	HOCl-detection probe
P-HP	H_2O_2-detection probe
PET	Positron emission tomography / Photo-induced electron transfer

PI	Propidium iodide
QDs	Quantum dots
RFP	Red fluorescent protein
Rh123	Rhodamine 123
ROS	Reactive oxygen species
Ru	Ruthenium
SEM	Standard error of the mean
SHG	Second harmonic generation
TCSPC	Time-correlated single-photon counting
TPEF	Two-photon excited fluorescence

Chapter 1

Introduction

1.1 Significance of real-time optical imaging of the liver

Humans always want to see farther and better. "...*The medical uses of optical imaging are revolutionising medicine; optical imaging is undergoing explosive growth fuelled by advances in high-sensitivity detectors, improved optics, and developments in molecular biology*…" [1]. Because liver is the key metabolic organ of the body and is critical for survival, various imaging technologies are now used in the screening and surveillance of liver pathology, such as ultrasound for hepatocellular carcinoma in patients at high risk. Computed tomography (CT) and magnetic resonance imaging (MRI) are increasingly able to provide a sensitive macroscopic view of the liver's anatomy and physiology, enabling early liver disease detection and characterisation. Emerging newer systems that based in light excitation and detection of bioluminescence, fluorescence, reflectance and sound (photoacoustic imaging) enable function, metabolic processes and molecular information to be defined with high resolution [2]. The combination of the light based systems, such as positron emission tomography (PET), with CT or MRI scans can lead to better cancer and metastasis diagnosis [3].

The light based systems, multi-photon (MPM) and confocal laser scanning microscopy (CLSM) and fluorescence lifetime imaging (FLIM), now provide mini-invasive quantitative imaging of fluorescent molecules in *in situ* and *in vivo* biological tissues and organs - in space (three dimensions), in time, in spectra, in lifetime and in fluorescence anisotropy (total of 7 dimensions). These techniques allow dynamic and functional cellular and subcellular imaging *in vivo* and have been used widely in neuroscience for observation of neuronal plastic changes, measuring ionized-calcium dynamics in brain [4] and imaging neurovascular bundle [5], in immunology [6] for imaging of heterogeneous immune process at cellular and molecular levels [7], in cancer research for studying angiogenesis [8] and metastasis [9]. Currently, the

application of optical imaging in the liver is limited. The main aim of this project is to systemically investigate the utility of MPM-FLIM for diagnosis and prediction of treatment response in liver diseases.

1.2 Objectives of this project

The overall aim of this project is to develop novel optical imaging methods for diagnosis and prediction of treatment response in liver diseases. The specific aims include:

- To develop stain-free and real-time histology of live liver in common liver diseases using MPM-FLIM. (main work of ***chapter 3***)
- To predict treatment response during liver injury by quantification of cellular oxidative stress using MPM-FLIM. (main work of ***Chapter 4***)
- To elucidate the *in vivo* fate of administered mesenchymal stem cells (MSCs) for the treatment of liver diseases by direct visualisation and mathematic modelling. (main work of ***Chapter 5***)

1.3 Achievements of this project

This thesis is written according to the guidelines of the University of Queensland. The outcomes of this PhD thesis are presented in the form of journal publications, and the chapters are presented in the following sequence:

- **Chapter 2** gives a comprehensive overview on the principles, opportunities, applications and limitations of MPM-FLIM in hepatology.
- **Chapter 3** demonstrates that MPM-FLIM is able to visualise the cellular morphology and microenvironment of live livers in common liver diseases.
- **Chapter 4** presents a two-photon dual sensing platform for *in vivo* imaging of oxidative stress at single cell-level resolution, and reveals that changes in oxidative stress of hepatocytes precede changes in conventional biochemical and histological assessments in liver injury.
- **Chapter 5** develops a mathematical model to characterise and predict the *in vivo* kinetics of administered MSCs for the treatment of liver cirrhosis based on direct visualisation of cell spatiotemporal disposition by MPM.
- **Chapter 6** summarises the achievements of the whole project, and presents outlooks of MPM-FLIM in the biomedical field.

References

[1] Lang P, Yeow K, Nichols A, Scheer A. Cellular imaging in drug discovery. Nature reviews Drug discovery. 2006;5:343-56.

[2] Matthews PM, Rabiner I, Gunn R. Non-invasive imaging in experimental medicine for drug development. Current opinion in pharmacology. 2011;11:501-7.

[3] Kapse N, Goh V. Functional imaging of colorectal cancer: positron emission tomography, magnetic resonance imaging, and computed tomography. Clinical colorectal cancer. 2009;8:77-87.

[4] Helmchen F, Waters J. Ca2+ imaging in the mammalian brain in vivo. European journal of pharmacology. 2002;447:119-29.

[5] Rai S, Srivastava A, Sooriakumaran P, Tewari A. Advances in imaging the neurovascular bundle. Current opinion in urology. 2012;22:88-96.

[6] Ishii T, Ishii M. Intravital two-photon imaging: a versatile tool for dissecting the immune system. Annals of the rheumatic diseases. 2011;70 Suppl 1:i113-5.

[7] Miller MJ, Wei SH, Parker I, Cahalan MD. Two-photon imaging of lymphocyte motility and antigen response in intact lymph node. Science (New York, NY). 2002;296:1869-73.

[8] Brown EB, Campbell RB, Tsuzuki Y, Xu L, Carmeliet P, Fukumura D, et al. In vivo measurement of gene expression, angiogenesis and physiological function in tumors using multiphoton laser scanning microscopy. Nature medicine. 2001;7:864-8.

[9] Zhou ZN, Boimel PJ, Segall JE. Tumor-stroma: In vivo assays and intravital imaging to study cell migration and metastasis. Drug discovery today Disease models. 2011;8:95-112

Chapter 2

Literature review: visualising liver anatomy, physiology and pharmacology using multiphoton microscopy

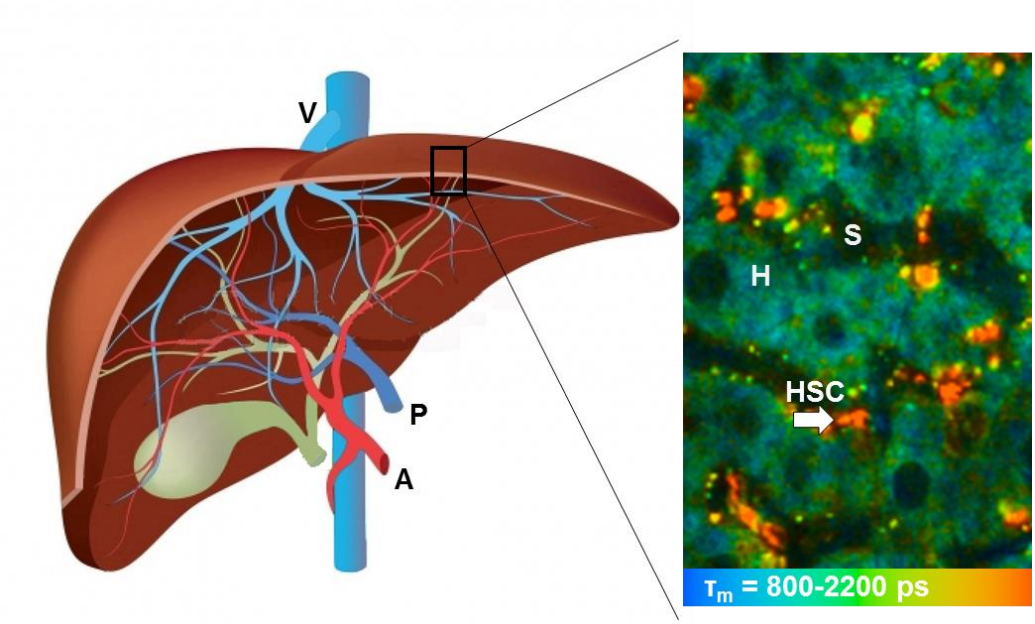

2.1 Synopsis

This chapter summarises the principles, opportunities, applications and limitations of multiphoton microscopy in hepatology. The information discussed in this chapter is essential to the development of real-time optical imaging strategies for the liver in the following chapters.

The review entitled, “Visualizing liver anatomy, physiology and pharmacology using multiphoton microscopy” has been published by *Journal of Biophotonics*, 2017; 10(1):46-60. The manuscript, figures and tables have been adjusted to fit the overall style of the Thesis and incorporated as this chapter.

2.2 Abstract

Multiphoton microscopy (MPM) has become increasingly popular and widely used in both basic and clinical liver studies over the past few years. This technology provides insights into deep live tissues with less photobleaching and phototoxicity, which helps us to better understand the cellular morphology, microenvironment, immune responses and spatiotemporal dynamics of drugs and therapeutic cells in the healthy and diseased liver. This review summarises the principles, opportunities, applications and limitations of MPM in hepatology. A key emphasis is on the use of fluorescence lifetime imaging (FLIM) to add additional quantification and specificity to the detection of endogenous fluorescent species in the liver as well as exogenous molecules and nanoparticles that are applied to the liver *in vivo*. We anticipate that in the near future MPM-FLIM will advance our understanding of the cellular and molecular mechanisms of liver diseases, and will be evaluated from bench to bedside, leading to real-time histology of human liver diseases.

Key Words: Multiphoton microscopy; Fluorescence lifetime imaging; Liver; Morphology, Function; Diseases

2.3 Introduction

Liver is one of the most important metabolic organs of vertebrates with multiple functions. It receives oxygenated blood from the heart via the hepatic artery, and nutrient-rich blood from the gastrointestinal tract via the portal vein (**Fig. 2.1A**). The blood flows through liver sinusoids (**Fig. 2.1B**, terminal vessels between hepatocyte cords and lined with Kupffer cells and endothelial cells), empties into the central vein, and exits the liver from hepatic veins. Hepatocytes make up 70-85% of the liver’s cell population. They are the key functional liver cells with important roles in metabolic, secretory and endocrine functions [1, 2]. Kupffer cells, another type of liver cells, are specialized macrophages in the liver located on the walls of the liver sinusoids [3].

Hepatic stellate cells (HSC) are pericytes located in the space of Disse, which is located between the hepatocytes and sinusoidal endothelium. Quiescent HSCs can be activated in response to liver damage, leading to collagen formation, fibrosis or cirrhosis [4]. Bile is secreted by hepatocytes, and drained into biliary ductules, which are lined with epithelial cells, then leaves the liver from the bile duct [3].

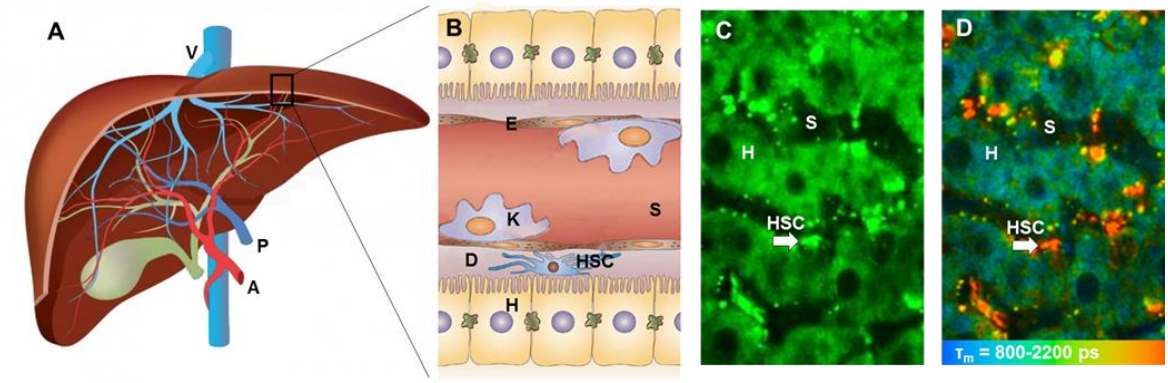

Figure 2.1 Structure of the liver. (A) Macrostructure of the liver. (B) Microscopic structure of liver sinusoid in hepatic lobules. (C) Representative TPEF image of the liver, recorded at $\lambda_{Exc}/\lambda_{Em}$: 740/350 to 650 nm. (D) Representative FLIM of the liver, recorded at $\lambda_{Exc}/\lambda_{Em}$: 740/350 to 450 nm. A: Hepatic artery; P: Portal vein; V: Hepatic veins; H: Hepatocyte; E: Endothelial cell; S: Sinusoid; K: Kupffer cell; D: Space of Disse; HSC: Hepatic stellate cell (arrow). Reproduced with permission [2]. 2015, The Royal Society of Chemistry.

Conventional optical illumination techniques are insufficient to precisely describe the complex internal three-dimensional structure, heterogeneous cell populations and the dynamics of biological processes of the liver. The need for better imaging tools has triggered a renaissance in the development of optical-microscopy instrumentation in the past three decades. In 1990, two-photon microscopy, later also referred to as multiphoton microscopy (MPM), was pioneered by Denk *et al*. at Cornell University [5]. This important invention enabled unprecedented quantitative deep imaging of the liver down to the molecular level. Fluorescence lifetime imaging (FLIM), first developed in 1989, was soon used in MPM in 1990s [6]. This imaging technique can provide detailed information about the liver microenvironment which cannot be revealed by microscopy using fluorescence intensity. The applications of MPM and FLIM in hepatology have been discussed in several review articles. These papers focused on specific areas of MPM such as defining liver functions [7],

imaging liver cancers [8], or just provided a general description of intravital imaging of the liver [9]. Although numerous techniques, fluorescent dyes and proteins that favor MPM have been proposed, there are only scattered reports on the detailed applications and limitations of MPM and FLIM in hepatology. The scope of this comprehensive review is to first summarize the principles and advantages of MPM for imaging the liver systematically. Subsequently, we will evaluate the application of MPM in visualizing anatomy, defining functions and studying pharmacology of the liver, and will highlight the use of FLIM. The information discussed in this review would be useful for the development of in vivo imaging strategies for the liver, as pointed out in the final section.

2.4 Principles and advantages of MPM for imaging the liver

2.4.1 MPM

Fluorescence is the emission of light by a substance after absorbing light or other electromagnetic radiation. Usually the absorbed light has a shorter wavelength and higher energy than the emitted light. This is known as single-photon fluorescence that is applied in traditional fluorescence microscopy. In contrast, MPM uses pulsed longer-wavelength light to excite fluorophores in the specimen being observed [5, 10]. Two photons must meet the fluorophores simultaneously (within 10−18 s) in order to excite a fluorophore to emit a fluorescence photon with shorter wavelength and higher energy. A typical optical principle of MPM is shown in **Fig. 2.2A**. MPM is considered as a revolutionary development in biological imaging because the longer-wavelength and lower-energy excitation light reduces photodamage and increases penetration depth, allowing imaging of living specimens [11]. Unlike confocal microscopes, MPM does not contain pinhole apertures, allowing the detector to be placed closer to the objective to optimize collection of scattered light, and further enhancing the imaging depth.

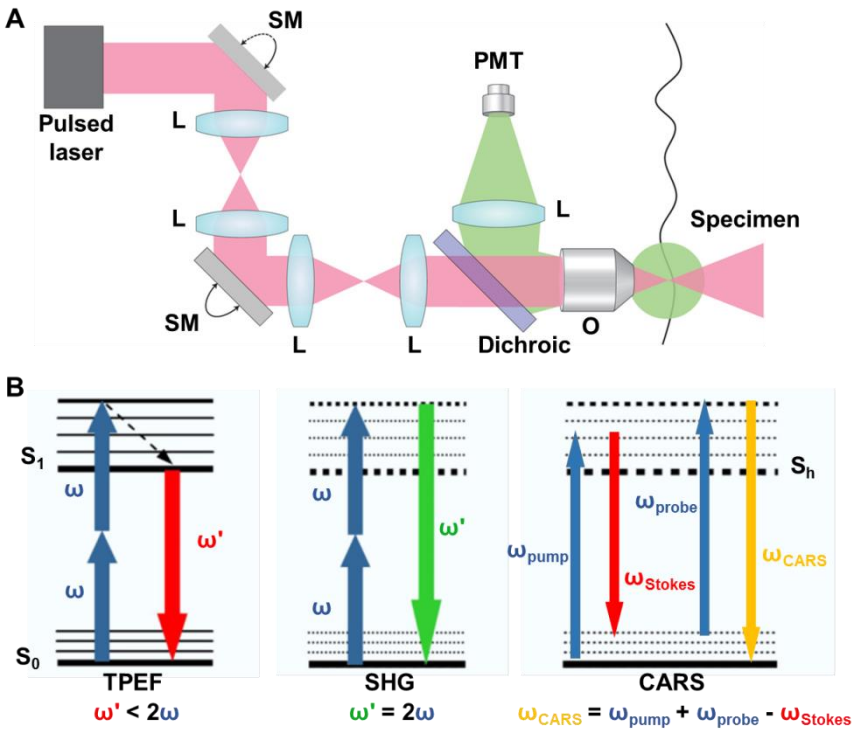

Figure 2.2 Typical optical principle of multiphoton systems and imaging modalities. (A) A typical MPM uses a raster scanning system to control the beam and a dichroic is used to separate TPEF from the excitation light and direct this fluorescence to a single-element detector such as a photomultiplier tube (PMT). (B) Energy level diagrams of TPEF, SHG and CARS imaging modalities. L: lens; SM: scan mirror; O: objective; S_0: the ground energy state; S_1: the excited state; S_h: the higher virtual state. Reproduced with permission [10, 12]. 2013, Nature Publishing Group. 2010, Elsevier.

2.4.2 Imaging modality of MPM

As shown in **Fig. 2.2B**, MPM can excite and detect nonlinear signals including two-photon excited fluorescence (TPEF), second harmonic generation (SHG) and coherent anti-Stokes Raman scattering (CARS) [13]. The concept of TPEF is based on the idea mentioned above that two photons of lower energy can excite an electron into a state with higher energy, from which it can decay and emit a shorter-wavelength light. Each photon carries approximately half the energy necessary to excite the fluorophore [5]. The most commonly used fluorophores in MPM have excitation spectra in the range of 400-500 nm, whereas the laser used to excite the TPEF lies in the 700~1000 nm range. As shown in **Table 2.1**, a number of

endogenous molecules in the liver can generate fluorescence, which is a hindrance of traditional fluorescence microscopy, yet is used as an advantage in TPEF imaging [14]. The metabolic coenzymes nicotinamide adenine dinucleotide hydride (NADH) is a respiratory substrate for complex I of the mitochondrial electron transport chain, which is an endogenous fluorophore in the cytoplasm of hepatocytes. As the fluorescence excitation, emission, and lifetime of NADH and NADPH overlap, these two molecules are usually measured together by MPM coupled with FLIM (MPM-FLIM) and referred to as NAD(P)H [15]. TPEF images of NAD(P)H in the liver can provide basic information of liver structure. Because NAD+, the oxidized form of NAD(P)H, has no fluorescence, changes in the fluorescence intensity of NAD(P)H can provide valuable information regarding cell metabolisms. Flavin adenine dinucleotide (FAD) which is only fluorescent in the oxidative states, can provide further information of the cellular redox state [14, 16]. The most common optical method for metabolic imaging is the “redox ratio,” which is the ratio of the fluorescence intensity of FAD and NAD(P)H. The redox ratio is sensitive to changes in the cellular metabolic rate and vascular oxygen supply [14, 16]. A decrease in the redox ratio or the fluorescence intensity of NAD(P)H is usually observed in cancer cells or injured cells.

In SHG, photons with the same frequency interact with a nonlinear substance and generate new photons with half the wavelength of the initial photons [17]. Since SHG is an even-order nonlinear non-absorption process, fluorophore is not required in the specimen. Only highly ordered structures without inversion symmetry are capable of emitting SHG light. Collagen, a sensitive indicator of liver fibrosis, is one such structure.

CARS is a third-order nonlinear optical process involving multiple types of photons: a pump photon, a Stokes photon and a probe photon. These three photons interact with the sample, and generate a coherent optical signal at the anti-Stokes frequency. This signal will be enhanced when the frequency difference between the pump and the Stokes photons coincides with the frequency of a Raman resonance [18]. CARS imaging is intrinsic and specific to molecular vibration, such as aliphatic C-H bonds of lipids. Thus it is ideal for detecting intracellular fat vacuoles in fatty liver tissues.

2.4.3 FLIM

The fluorescence lifetime is the mean time a fluorophore remains in the excited state before emitting a photon (fluorescence) and returning to the initial ground energy state. FLIM has been used as an important imaging technique in MPM, which constructs a spatial distribution map of fluorescence lifetimes from a fluorescent specimen [19]. The lifetime of the fluorophore signal, rather than its intensity, is used to create the image. **Fig. 2.1D** shows an example of FLIM image of normal mouse liver. This technique has the advantage of differentiating various endogenous and exogenous fluorophores in the liver tissue based on their unique lifetimes. **Table 2.1** shows the lifetimes of major endogenous fluorophores in the normal liver. Lifetime changes of exogenous fluorophores usually reflect drug-interactions or protein-interactions, while those changes of endogenous fluorophores reflect changes in liver microenvironment, which cannot be revealed by microscopy using fluorescence intensity.

A common application of FLIM in the liver is to measure the fluorescence lifetime of NAD(P)H. NAD(P)H can exist as free or protein-bound molecules, which have similar excitation and emission wavelengths, but can be distinguished by their distinct fluorescence lifetimes. Protein-bound NAD(P)H mainly locates in mitochondrial membrane, and produces adenosine triphosphate (ATP) in aerobic conditions, while free NAD(P)H is located in the cytoplasm, involving in ATP synthesis without oxygen in glycolysis. The relative contribution of protein-bound NAD(P)H decrease in hypoxia, mainly because cellular respiration is shifted to glycolysis, producing ATP in anaerobic conditions [20, 21]. The changes of lifetimes of free and protein-bound NAD(P)H also indicate altered metabolic state, as is typically observed in cell differentiation, apoptosis and necrosis [20].

2.5 Imaging liver anatomy and diagnosing liver diseases

MPM has been applied in diagnosis of almost all types of liver diseases in human beings and animals. Liver fibrosis, cancer and steatosis are the most widely studied liver diseases using MPM, which will be discussed in detail below. In addition, the MPM optical diagnostic features for hepatic ischemia-reperfusion (I/R) injury were reported to include reduced fluorescence and cellular vacuolation of hepatocytes, and heterogeneous spread of damage over the liver [22].

Acetaminophen (APAP) induced liver injury [23] and hepatitis C virus infections [24] have also been visualized using fluorescent dyes or sensors for MPM.

2.5.1 Normal liver

The capsule of the liver, known as Glisson's capsule, is a fibrous connective membrane mainly composed of collagen and elastin fibers. It encompasses the hepatic parenchyma, and contributes significantly to the global mechanical behavior of the liver. MPM has been used to characterize the shape, geometry and microstructure arrangement of the capsule using TPEF and SHG [25, 26]. The obtained images revealed that the collagen/elastin ratio increases from the inner to the outer surface of the liver capsule. The microstructure and strain fields of the capsule present heterogeneity among different layers. Reorientation occurs in fiber layers from the inner to the outer surface of the liver capsule.

The cellular structure of liver can be imaged as deep as 250 μm below the liver capsule by MPM. As shown in **Fig. 2.1**, **2.3** and **2.4**, hepatocyte cords with bright autofluorescence of NAD(P)H are separated by the blood-filled dark sinusoids in TPEF imaging. The stellate cells are smaller in size but have strong vitamin A-associated autofluorescence and a longer lifetime than that of NAD(P)H [21]. Fenestrations are transcellular pores in endothelial cells that facilitate transfer of substrates between blood and the extravascular compartment. Liver sinusoidal endothelial cells could be stained by 6-lauroyl-2-dimethylaminonaphthalene (LAURDAN) to visualize the number and size of fenestrations using MPM [27]. Recently, more specific fluorescence-conjugated antibodies (such as anti-PECAM1/CD31 or anti-VCAM-1/CD106) have been developed to stain viable liver sinusoidal endothelium [9, 28].

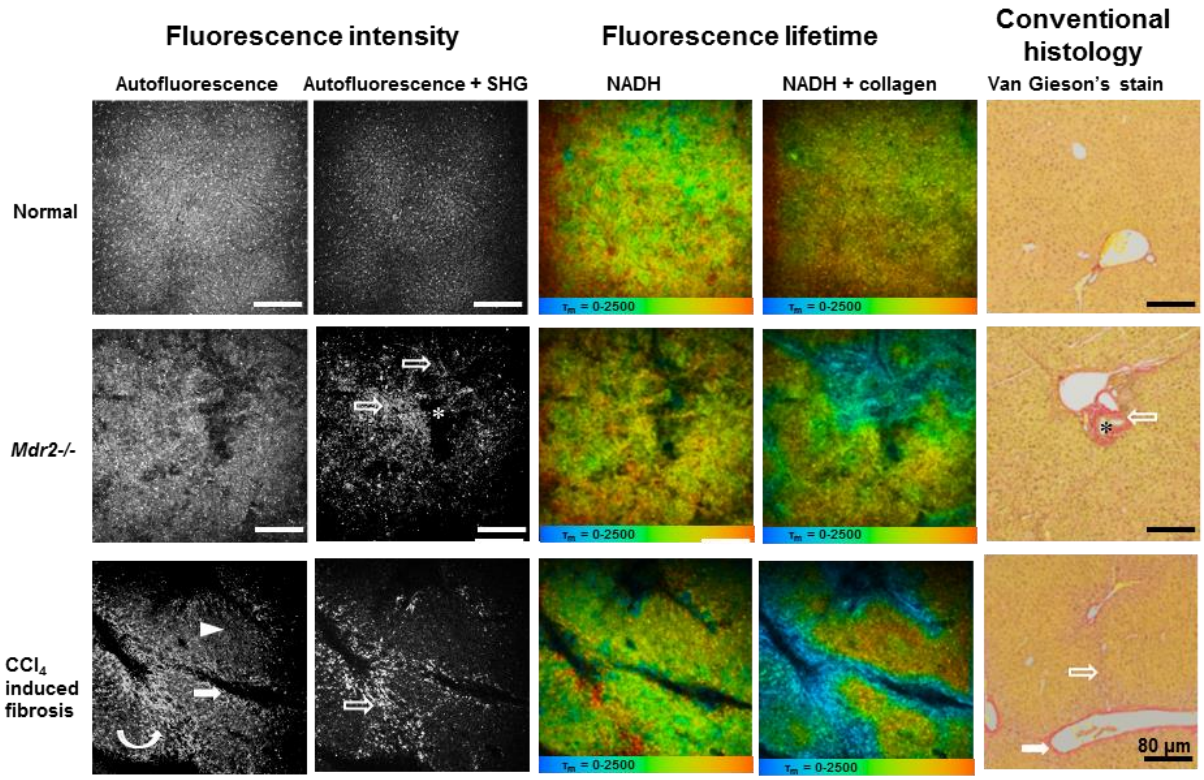

Figure 2.3 MPM-FLIM and conventional histopathological images of liver in healthy mice, *Mdr2−/−* mice and mice with CCl_4 induced liver fibrosis at low magnification (10×) (scale bar: 80 μm). Autofluorescence intensity image was recorded at $\lambda_{Exc}/\lambda_{Em}$: 740/350 to 650 nm. Autofluorescence and SHG intensity image was recorded at $\lambda_{Exc}/\lambda_{Em}$: 800/350 to 650 nm. Pseudocolored fluorescence lifetime image for NADH (τ_m: 0-2500 ps; blue-green-red) was recorded at $\lambda_{Exc}/\lambda_{Em}$: 740/350 to 450 nm. Pseudocolored fluorescence lifetime image for NADH and collagen (τ_m: 0-2500 ps; blue-green-red) was recorded at $\lambda_{Exc}/\lambda_{Em}$: 800/350 to 450 nm. Conventional histological images were collected on Van Gieson's stained section. Opened arrows indicate collagen; asterisks indicate bile duct; curved arrow indicates bridges formed by stellate cells; filled arrows indicate postsinusoidal venules; and arrow head indicates injury of hepatocytes. MPM-FLIM images of unfixed live livers were collected within 30 min after surgical procedures started, and 2 days after the last CCl_4 injection. Reproduced with permission [21]. 2015. OSA Publishing.

2.5.2 Liver fibrosis

In liver fibrosis, injury of hepatocytes can be observed as reduced fluorescence of NAD(P)H in TPEF imaging (**Fig. 2.3** and **2.4**) [21]. Moreover, FLIM shows

changes in cellular metabolic pathways as indicated by the decrease of lifetimes of free and protein-bound NAD(P)H, and contribution of protein-bound NAD(P)H (**Fig. 2.4**). The livers of mice receiving CCl_4 for 5 weeks showed signs of postsinusoidal venules. HSCs can be detected using real-time histology by their distinct vitamin A-associated autofluorescence. Inhomogeneous distribution of stellate cells was found in a mouse model of chronic chemical hepatic injury and advanced liver fibrosis [21]. The stellate cells accumulated in centrilobular region around central veins, and reduced in midzonal regions. The regional redistribution of stellate cells formed bridges between postsinusoidal venules in some liver lobules. The morphology and distribution of stellate cells imaged by MPM provide valuable information about cellular microenvironment during development of liver fibrosis, which cannot be obtained from conventional histology.

SHG imaging has been performed on liver biopsies taken from patients with liver fibrosis or cirrhosis [21, 29], rodents with CCl_4 induced chronic injury and fibrosis [21], and cholangitis and biliary fibrosis (*Mdr2−/−* and bile duct ligation) [21, 29]. MPM can clearly reveal the increase of the collagen amount during fibrosis progression and offer the possibility of an accurate characterization of fibrosis without specific staining. As shown in Figure 3, collagen deposition was obvious in the centrilobular region and pseudolobular formation was evident in in CCl_4 induced fibrotic liver. While the livers with biliary fibrosis of 20-week-old *Mdr2−/−* mice showed intercellular fibrosis, especially around the medium sized to large bile ducts of the periportal region. Two quantification systems, Fibro-C-Index [29] and Fibrosis-SHG index (**Fig. 2.5**) [12] have been developed for the assessment of liver fibrosis using MPM. Both systems have been compared and validated by pathological examination, indicating the high reliability and sensitivity for potential application of MPM in clinical diagnosis of liver fibrosis. Since collagen SHG response is effectively instantaneous [30], the mean lifetimes decreased significantly in fibrotic liver at excitation of 800 nm (containing both NADH and collagen signals), allowing the discrimination from normal liver (**Fig. 2.3**). MPM-FLIM would be a powerful tool providing realtime histology which combines morphology and quantitative evaluation of liver fibrosis simultaneously.

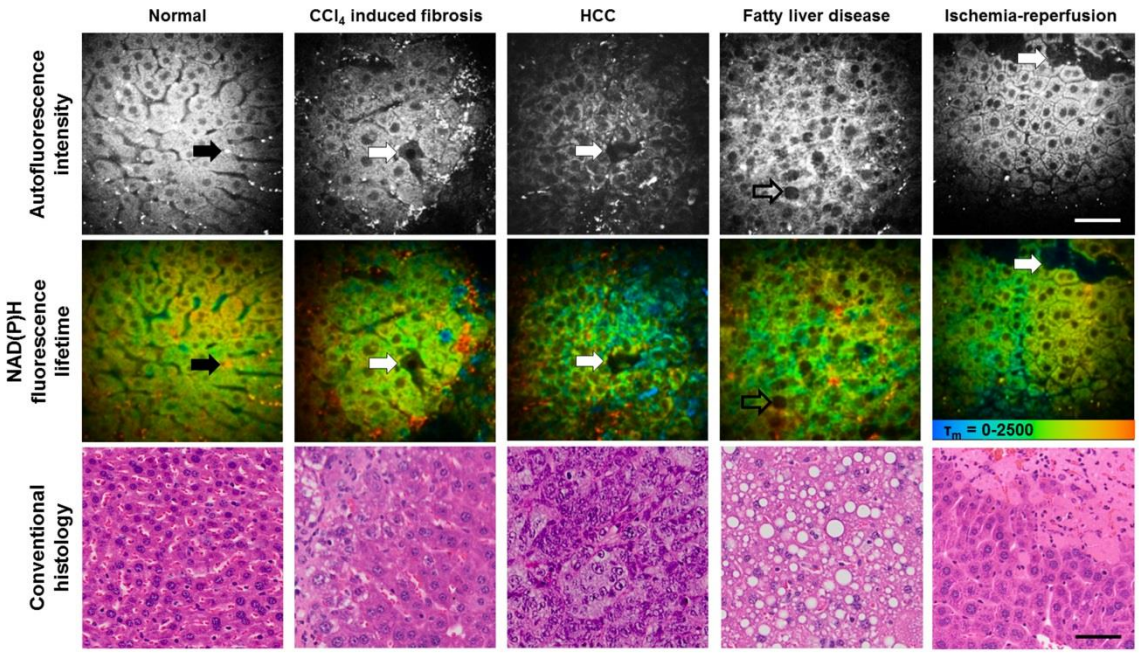

Figure 2.4 MPM-FLIM and conventional histopathological images of the mouse liver in health and disease at high magnification (40×) (Scale bar: 20 μm.). Autofluorescence intensity image was recorded at $\lambda_{Exc}/\lambda_{Em}$: 740/350 to 650 nm. Pseudocolored fluorescence lifetime image (τ_m: 0-2500 ps; blue-green-red) was recorded at $\lambda_{Exc}/\lambda_{Em}$: 740/350 to 450 nm. Black arrow indicates stellate cells associated autofluorescence; white arrows indicate cellular necrosis; and opened arrow indicates intracellular fat vacuole. MPM-FLIM images of unfixed live livers were collected within 30 min after surgical procedures started. Conventional histological images were collected on H&E stained section. Reproduced with permission [21]. 2015. OSA Publishing.

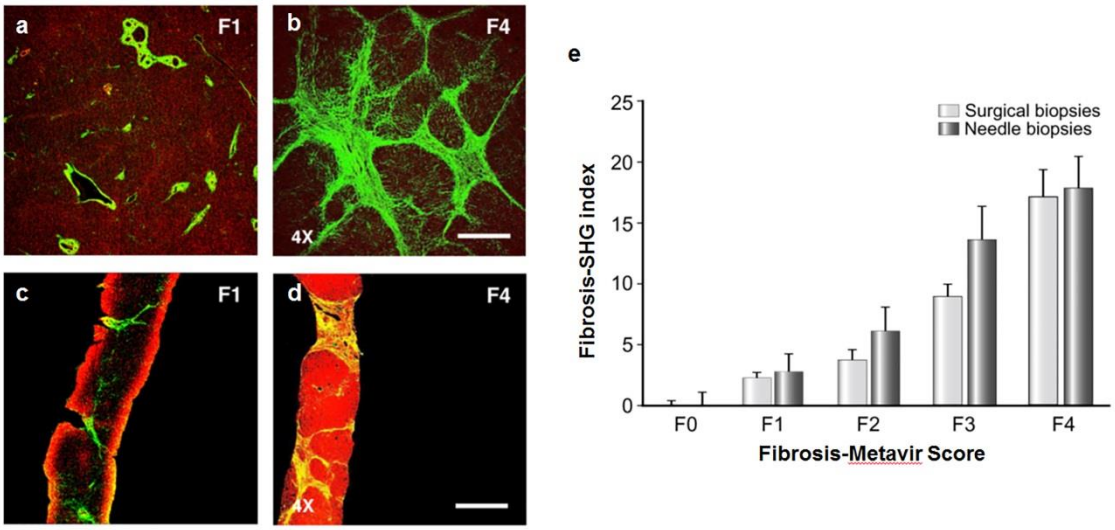

Figure 2.5 Collagen quantification in human liver fibrosis using MPM. (a-d) TPEF/SHG images of the fibrosis (F0-Metavir grade) and cirrhotic (F4-Metavir grade) liver samples from surgical (a) and needle biopsies (b). F-Metavir grades have been determined by a pathologist using the Metavir scoring system from conventional histology. Red color represents the TPEF signal of hepatocytes and green color represents the SHG signal of collagen fibers. Laser intensity was set at 100 mW and wavelength was fixed at 810 nm. Scale bar: 1 mm. (e) Standardized Fibrosis-SHG indexes determined for each F-Metavir stage in 46 surgical and 73 needle biopsies. Histograms indicate the average indexes ±SEM after normalization. Reproduced with permission [12]. 2010, Elsevier.

2.5.3 Liver cancer

The most common type of primary liver cancer is hepatocellular carcinoma (HCC). The MPM optical diagnostic features for HCC have been established and validated in different studies [21, 31]. High-resolution MPM images have clearly demonstrated extensive cell heterogeneity characterized by irregular size and shape, increased nuclear to cytoplasmic ratio, decreased autofluorescence of NAD(P)H, central necrosis and intercellular collagen in HCC (**Fig. 2.4**). Yan *et al.* performed a pilot preclinical study investigating 224 surgical specimens including benign and malignant liver lesions such as hemangioma, focal nodular hyperplasia, HCC, cholangiocarcinoma, and colorectal cancer liver metastases. They found that MPM is able to diagnose liver cancer and differentiate benign and malignant liver lesions with high sensitivity, specificity and accuracy [31].

In FLIM images, the cellular lifetimes of free and protein-bound NAD(P)H, and contribution of protein-bound NAD(P)H significantly decreased in HCC, which is consistent with hypoxia and the increased levels of glycolysis in neoplastic cells (**Fig. 2.4**). In poorly-differentiated HCC sections, an increased cellular lifetime of red fluorescent pigments including porphyrins, biliverdins and bilirubins, and scattered short-lifetime spots can also be detected non-uniformly, which may represent the inflammation-induced infiltrated leukocytes [32]. Thus, MPM-FLIM has the potential to become a powerful clinical tool in the future to perform real-time diagnosis of liver cancer and differentiation of benign and malignant liver lesions.

2.5.4 Liver steatosis

In liver with steatosis, black intracellular fat vacuole can be detected as spots with significantly reduced fluorescence of NAD(P)H (darker than the nuclei) in TPEF images (**Fig. 2.4**) [21]. The cytoplasm of hepatocytes has a sponge-like appearance because of numerous small black intracellular fat inclusions in mice after feeding a high fat diet for 14 days (**Fig. 2.4**). Compared to TPEF imaging, CARS imaging can specifically visualize fat droplets in fresh liver samples and extract the fat content through image analysis [33]. Similarly to the way using SHG to quantify the collagen amount in the fibrotic liver, CARS imaging has been used to quantitatively assess the fat in rat livers with steatosis [33]. The content of hepatic fat measured by MPM has been correlated well with that determined by biochemical analysis. This staining free technique has the potential for early diagnosis and rapid detection of liver steatosis.

2.6 Imaging liver physiology and defining liver function

In the past two decades, the development of MPM has resulted in an explosion of mechanistic investigation of liver physiology down to the molecular level. Compared to conventional microscopy, MPM has an important advantage of intravital imaging, which can enhance our understanding of liver physiology and function, and provide new insights into pathogenesis and disease control mechanisms. **Table 2** shows the characteristics and functions of fluorescent probes commonly used in MPM imaging of the liver physiology.

2.6.1 Mitochondrial physiology

The mitochondrion is a double membrane-bound organelle found in most eukaryotic cells. The mitochondrial permeability transition (MPT) is defined as an increase in the permeability of the mitochondrial membranes to molecules less than 1500 Dalton [34]. MPT results from the opening of MPT pores located in the inner membrane of the mitochondria under certain pathological conditions such as hepatic I/R injury, leading to mitochondrial depolarization and swelling, and cell death through apoptosis or necrosis. MPM has been applied to visualize the mitochondrial physiology using different fluorescent probes. Propidium iodide (PI) labels the nuclei of nonviable cells, and can be used to visualize the overall cell viability [35]. The opening of MPT pores could be assessed using calcein acetoxymethyl ester in TPEF imaging. Calcein is a fluorescent molecule that cannot be taken up by mitochondria after intravenous injection, resulting in the mitochondria appearing as dark voids in the hepatocytes in the normal liver [36]. In mice with hepatic I/R injury or bile duct ligation, the opening of MPT pores in hepatocytes can be revealed by the appearance of calcein fluorescence in the mitochondria matrix space, which are dark voids in normal hepatocytes [37, 38]. Rhodamine 123 (Rh123) is another commonly used fluorescent dye in TPEF imaging to visualize polarized mitochondria [35]. After intravenous injection, Rh123 selectively accumulates in polarized mitochondria of the healthy liver, resulting in bright punctate fluorescence of Rh123 in hepatocytes. While the liver with hepatic I/R injury [38, 39] or obstructive cholestasis [37] shows dim diffuse of Rh123 fluorescence, denoting that many mitochondria did not take up Rh123 because of depolarization. Thus, MPM can be employed to investigate the drug efficacy. As shown in **Fig. 2.6**, the effect of NIM811, an MPT inhibitor, was evaluated using fluorescent probes of PI and Rh123 to visualize the attenuation of mitochondrial depolarization and MPT onset in APAP induced liver injury [40].

Table 2.1 Characteristics of major endogenous fluorophores and collagen SHG in normal liver

Fluorophore	Sample	Excitation wavelength* (nm)	Emission wavelength (nm)	Fluorescence lifetime (ns)	Reference
NAD(P)H	Mouse and rat *in vivo*, human *ex vivo*	740-800	350 - 490	0.3 - 0.7 (bound), 2.5–3.0 (free)	[21, 22, 31, 47]
FAD	Rat *in vivo*, human *ex vivo*	800	500 - 620	0.04 - 0.4 (bound), 2.3 - 2.8 (free)	[31, 47, 75]
Elastin	Human *ex vivo*	850	500 - 550	1.96	[25, 43]
Vitamin A	Mouse and rat *in vivo*	700-830	~ 500	1.7 – 2.2	[21]
Porphyrin / biliverdin / bilirubin	Human *ex vivo*	1230	670	0.4 - 1	[32]
Collagen SHG	Human and rat *ex vivo*	800 - 1230	1/2 laser wavelength	No lifetime	[25, 31, 32, 76]

*: two-photon excitation

Table 2.2 Characteristics and functions of fluorescent probes commonly used in TPEF imaging of the liver

Probe	Molecular weight (g/mol)	Excitation wavelength (nm)	Emission wavelength (nm)	Function	References
RH 123	380.82	820	500-550	Indicates mitochondrial polarization Indicates P-gp function	[23, 35, 37, 38, 47] [42, 44, 67]
Calcein	622.53	720	500-550	Indicates MPT	[38]
Sodium fluorescein	332.31	920	515-620	Indicates hepatic microcirculation and Oatp function	[42, 62]
RITC-dextran	70,000	920	573	Labels sinusoids Labels abnormal hepatocytes	[23, 50, 77] [51, 67]

Table 2.2 - Continued.

Probe	Molecular weight (g/mol)	Excitation wavelength (nm)	Emission wavelength (nm)	Function	References
CFDA	460.39	780	520	Indicates hepatobiliary excretion function	[48, 50, 51, 77]
TRITC-labeled albumin	443.52	488*	561	Labels sinusoids	[57]
Rhodamine 6G	479,02	530*	556	Labels mitochondria	[50]
TMRM	500.93	548*	574	Indicates mitochondrial polarization	[50]
FITC-dextran	70,000	920	518	Labels sinusoids	[50, 54, 67]
DAPI	277.32	720	461	Labels cell nuclei	[78]
AlexaFluor488	570.48	496*	519	Labels antibody	[54, 78]
PI	668	920	608	Indicates cell viability	[35]
LAURDAN	353.54	800	423-483	Labels liver sinusoidal endothelial cells	[27]
PE-coupled anti-PECAM-1	-	565 or 498*	573	Labels liver sinusoidal endothelial cells	[28]
Texas red-dextran	70,000	596*	615	Labels macrophages	[54]
PD nanobeads	-	545*	575	Labels macrophages	[55]
Carboxylated latex particles	-	580*	605	Labels macrophages	[53]

*: single-photon excitation, RH 123: Rhodamine 123, RITC-dextran: Rhodamine B isothiocyanate-dextran, CFDA: Carboxyfluorescein diacetate, TRITC: tetramethylrhodamine isothiocyanate, TMRM: tetramethylrhodamine methylester, FITC-dextran: Fluorescein isothiocyanate-dextran, DAPI: 4',6-diamidino-2-phenylindole, PI: Propidium iodide, LAURDAN: 6-lauroyl-2-dimethylaminonaphthalene, PE: phycoerythrin, PECAM-1: platelet-endothelial cell adhesion molecule-1, MPT: Mitochondrial permeability transition.

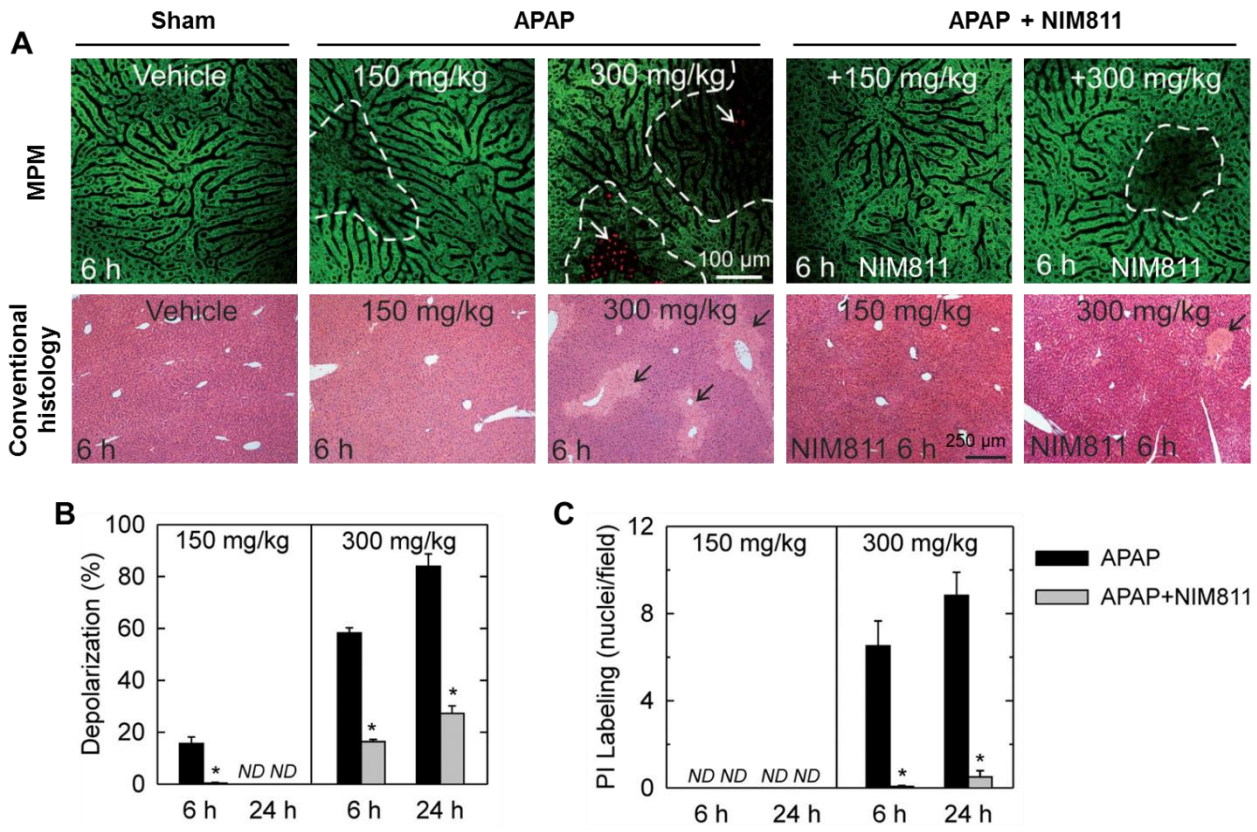

Figure 2.6 *In vivo* visualization of mitochondrial depolarization and cell death in mouse liver using MPM. (A) NIM811 decreases hepatocellular cell death and/or mitochondrial depolarization after both low and high dose APAP. NIM811 (10 mg/kg) was administered by gavage 1 h before APAP. Top and bottom rows show intravital MPM and conventional histopathological images, respectively. Punctate labeling with Rh123 signifies mitochondrial polarization, whereas dim diffuse Rh123 staining denotes mitochondrial depolarization (dashed line). Nuclear PI labeling signifies cell death (white arrows). Conventional histological images were collected on H&E stained section. Black arrows identify necrotic areas. (B and C): Protection by NIM811 against depolarization and cell death induced by APAP. Percent area of mitochondrial depolarization is plotted for various treatment groups (B). PI-labeled nuclei were also counted (C). N.D., not detectable; *$P < 0.05$. Reproduced with permission [40]. 2016, Oxford University Press.

2.6.2 Functions of hepatic enzymes and transporters

Hepatic enzymes and transporters play a significant role in drug metabolism and biliary excretion. In most studies, functions of hepatic transporters are evaluated in

cultured cell system or isolated perfused liver [41]. However, both methods have obvious disadvantages such as limited biological significance in cell lines and indirect analysis of transport processes in perfused liver models [42]. Using specific fluorescent probes, MPM allows direct measurement of enzyme and transporter functions. Recently, a two-photon excited ratiometric fluorescent probe has been developed for sensitive and selective detection of CYP1A, one of the most important phase I drug-metabolizing enzymes [34]. TPEF imaging can directly assess the functions of hepatic transporters by observing the in vivo distribution kinetics of specific fluorescent substrates in the liver [42-44]. For example, the functions of biliary canalicular transporter MDR1 (P-glycoprotein, P-gp) and basolateral transporter organic anion transporting polypeptide (Oatp) have been evaluated using their specific substrates Rh123 [45] and sodium fluorescein [46]. In hepatic I/R injury, the uptake and clearance of fluorescein are found to be delayed, probably due to the impaired hepatic microcirculation and the dysfunction of efflux transporters [47]. And the impaired P-gp function can be revealed by the increased fluorescence intensity of Rh123 in the hepatocytes with I/R injury compared to sham [7, 44].

2.6.3 Hepatobiliary excretory function

Bile excretion is part of hepatobiliary function. The liver is responsible for the uptake, processing, and excretion of many exogenous or endogenous substances into bile by hepatocytes [48]. Carboxyfluorescein diacetate (CFDA) has been used to define the hepatobiliary excretory function of healthy mice, mice with APAP-induced liver injury and with obstructive cholestasis [48-50]. CFDA is a nonfluorogenic substance and can be hydrolyzed by esterase into fluorogenic carboxyfluorescein (CF) after taken up by hepatocytes. The kinetics of CF can be determined in hepatocytes and sinusoids separately based on its fluorescence intensity. The delayed clearance of CF from hepatocytes into bile canaliculi was observed in mice with bile duct ligation. An active machinery operating backflow of bile containing CF from hepatocytes into sinusoids was found in mice with obstructive cholestasis and APAP-induced liver injury [48, 50, 51].

In addition, fluorescein has also been used to reflect the hepatobiliary excretory function. The uptake and clearance of fluorescein has also been found to be delayed in mice with liver steatosis and hepatic I/R injury using TPEF imaging, and confirmed by FLIM [47, 52]. Conventional methods for studying the hepatobiliary excretory function usually involve biochemical analyses of contents in the bile, liver, blood or urine, while MPM enables intravital imaging of fluorescent probes in the liver at the subcellular level. This imaging technique can provide further quantitative measures of metabolic and

hepatobiliary excretory function, and hence extend the qualitative liver function tests now available.

2.6.4 Cell physiology and migration

MPM has been applied to study the cell migration and function in the liver in a variety of disease states including HCC, colorectal cancer liver metastases, hepatic I/R injury, parasitic infection and liver regeneration. Kupffer cells can be labeled in vivo by intravenous injection of red fluorescent carboxylated latex particles [53], 70-kDa Texas red-dextran [54] and PD nanobeads (545 marked) [55] due to their macrophage phagocytic ability. After labelling, TPEF imaging of the liver reveals that Kupffer cells are the main cellular scavenger for circulating particle-associated antigens in homeostasis [53]. These cells are the only detectable population of mononuclear phagocytes within granulomas induced by Leishmania donovani infection [55]. Kupffer cells do not migrate to interact with vessels while infiltrating monocytes interact directly with sinusoids after partial hepatectomy [54].

Leukocytes are the cells of the immune system that are involved in protecting the body against both disease and foreign invaders. These cells can be further divided into five main types: neutrophils, eosinophils, basophils, lymphocytes, and monocytes [56]. Green fluorescent protein (GFP)-expressing leukocytes were used for MPM imaging in almost all the studies, because most leukocytes lack the phagocytic ability and are difficult to be labelled using fluorescent dyes [53, 57-59]. The GFP-expressing tumor-infiltrating leukocyte adhesion and migration in HCC have been visualized *in vivo* at the single-cell level [57]. Their migration was found in a random manner with frequently changed infiltrating directions. In hepatic I/R injury, MPM successfully detected the numbers, velocity, and morphology of recruited neutrophils in vivo, and has potential for a wide range of applications to investigate the mechanism of I/R injury [58].

Recently, MPM has been used to detect the colorectal cancer liver metastases in living mice taking its advantages of imaging target organs for a long period at a high magnification and in the deep depths from the surface [8, 60]. An animal model of colorectal cancer liver metastases was developed by inoculating red fluorescent protein (RFP) expressing colorectal cancer cells into the spleens of GFP transgenic mice. As shown in **Fig. 2.7**, the multi-stage tumor metastatic processes have been visualised in this mouse model, including tumor cell arrest, tumor cell-platelet interaction, tumor cell-leukocyte interaction, and metastatic colonization in the liver [8, 61]. These studies are good examples of the applications of MPM as a tool for basic investigation.

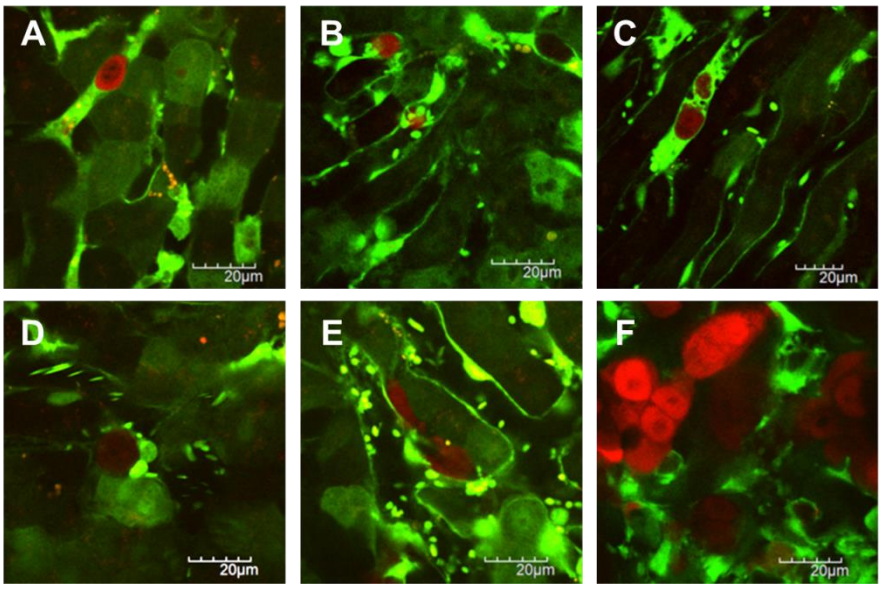

Figure 2.7 Visualisation of the liver metastatic process of colon cancer cells. (A) Colon cancer cells arrest in the sinusoid. (B) Tumor cell-platelet interaction. (C) Platelets aggregation to the tumor cell. (D) Tumor cell-leukocyte interaction. (E) Tumor cell extravasation. (F) Liver metastatic colonization of colon cancer cells. Red color represents the colon cancer cells and green color represents the structure of the liver and blood vessels. Reproduced with permission [8, 61]. 2014. e-Century Publishing Corporation. 2012. Koji Tanaka et al.

2.7 Pharmacokinetic imaging in the liver

A precise method of understanding and analyzing pharmacokinetic events is to directly observe the distribution, metabolism and excretion of diagnostic or therapeutic agents in space and over time. MPM provides a powerful tool to spatiotemporally monitor the transport of molecules, nanoparticles and biological agents in the liver at the cellular level for pharmacokinetic analysis.

2.7.1 Molecule imaging

The pharmacokinetics of fluorescein and RH123 has been investigated by MPM in rat liver [43, 44, 62]. Since MPM allows simultaneous visualization of the organ autofluorescence and molecule fluorescence, it is able to determine the levels of fluorescent molecules in the sinusoids, hepatocytes and the bile respectively (**Fig. 2.8A**), which enables dividing the liver into subcompartments for pharmacokinetic modelling, as seen in **Fig. 2.8B**. A physiologically based pharmacokinetic (PBPK) model has been developed to characterize the kinetics of fluorescein at the single-cell resolution in health and diseased liver *in vivo* [52]. Using the same intravital imaging technique, half-life of

Rh123 is calculated by fitting the decay of fluorescence intensity in hepatocytes vs. time profile into the exponential equation [44].

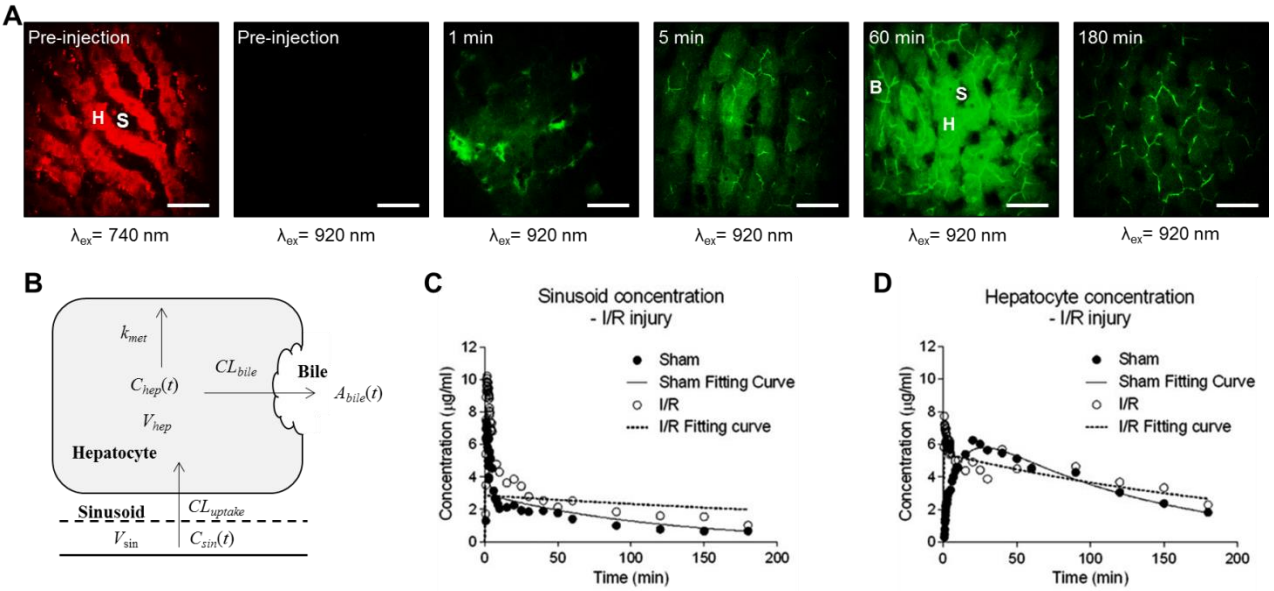

Figure 2.8 Pharmacokinetic imaging of fluorescein in the liver at the cellular level. (A) TPEF images of fluorescein in normal rat livers at various time points after bolus injection via jugular vein with high magnification (40 ×) (scale bar: 20 μm). The symbol S indicates sinusoid, H indicates hepatocyte and B indicates bile duct. Red color represents autofluorescence of liver and green color represents fluorescein. (B) Schematic overview of compartmental model describing hepatic uptake and elimination kinetics of fluorescein. (C and D) Fluorescein concentration-time profiles in the sinusoid and hepatocyte compartments. Reproduced with permission [52, 63]. 2015. American Society for Pharmacology and Experimental Therapeutics. 2014. John Wiley and Sons.

Furthermore, FLIM imaging adds the capability of differentiating fluorescent molecules from biological tissues based on their fluorescent lifetimes. For example, fluorescein and its metabolite fluorescein mono-glucuronide (FG) have an overlapping excitation and emission spectra [62], which make them to be hardly distinguished using TPEF imaging. However, the fluorescence lifetime of fluorescein and metabolite FG is reported to be 3.8 to 4.1 ns and 2.3 ns, respectively [62], which can be differentiated by FLIM. The in vivo distribution and metabolism of fluorescein has been studied based on the lifetime change in different zonation of rat liver using MPM-FLIM, showing the mean lifetimes of fluorescein and FG decease over time after injection [62]. Therefore, the combination of MPM and FLIM provides a novel technique for studying real-time distribution and metabolism of fluorescent molecules in the liver at a high resolution.

MPM has also been used to real-time evaluate the chemotherapy response on the colorectal cancer liver metastases [64]. After administration of 5-fluorouracil or irinotecan, tumor cell fragmentation, condensation, swelling and intracellular vacuoles are observed under time-series intravital TPEF imaging. A pharmacokinetic/pharmacodynamic model could be developed based on these observations.

2.7.2 Nanoparticle imaging

Nanoparticles (NPs) are defined as spherical (or quasispherical) particles with a diameter less than 100 nm, but often refer to the range up to 300–500 nm [65]. Since NPs have unique physiochemical properties, and have been intensively applied to drug and gene delivery, imaging and diagnosis [66], it is important to investigate their pharmacokinetics for clinical applications. Although many studies have reported the organ-level distribution of NPs, very few have addressed their disposition in organs at the cellular level [63]. The uptake, distribution and excretion of fluorescent or fluorescent labelled NPs can be investigated using TPEF imaging at the single cell resolution [67-70]. Polymeric NPs with high bond repetition rate are highly suitable for CARS imaging because the CARS signal scales quadratically with the bond concentration [70].

The *in vivo* spatiotemporal disposition of quantum dots (QDs), a typical example of long-circulating NPs, has been intensively explored in the liver at a single cell level using MPM [63, 71]. The concentration profile of QDs determined from the QD fluorescence intensity in sinusoids correlates well with that in the plasma measured by inductively coupled plasma mass spectrometry (ICP-MS) [63]. This suggests that MPM may be used as a semi-quantitative method to investigate the distribution of fluorescent NPs in living organisms, particularly in the initial distribution phase (0.5 to 5 min), when collecting blood samples is difficult. Furthermore, the enriched quantified data obtained from MPM imaging, especially at early time, allows more sophisticated pharmacokinetic modelling to reveal more detail information of NP disposition, while blood sampling and ICP-MS analysis can only provide limited data for modelling [63]. As shown in **Fig. 2.9**, the QD sub-organ distribution visualized by TPEF imaging was further confirmed by FLIM imaging based on the change of average fluorescence lifetime. Since the fluorescence lifetime of QDs is much longer than that of liver cells, the increased fluorescence lifetime in the sinusoid but not in hepatocytes after QDs injection confirmed that these negatively charged QDs predominantly distributed in the sinusoids [63]. Thus, even if the excitation and emission spectrum of a fluorophore overlap with those of the background, it can still be distinguished based on different fluorescence lifetimes.

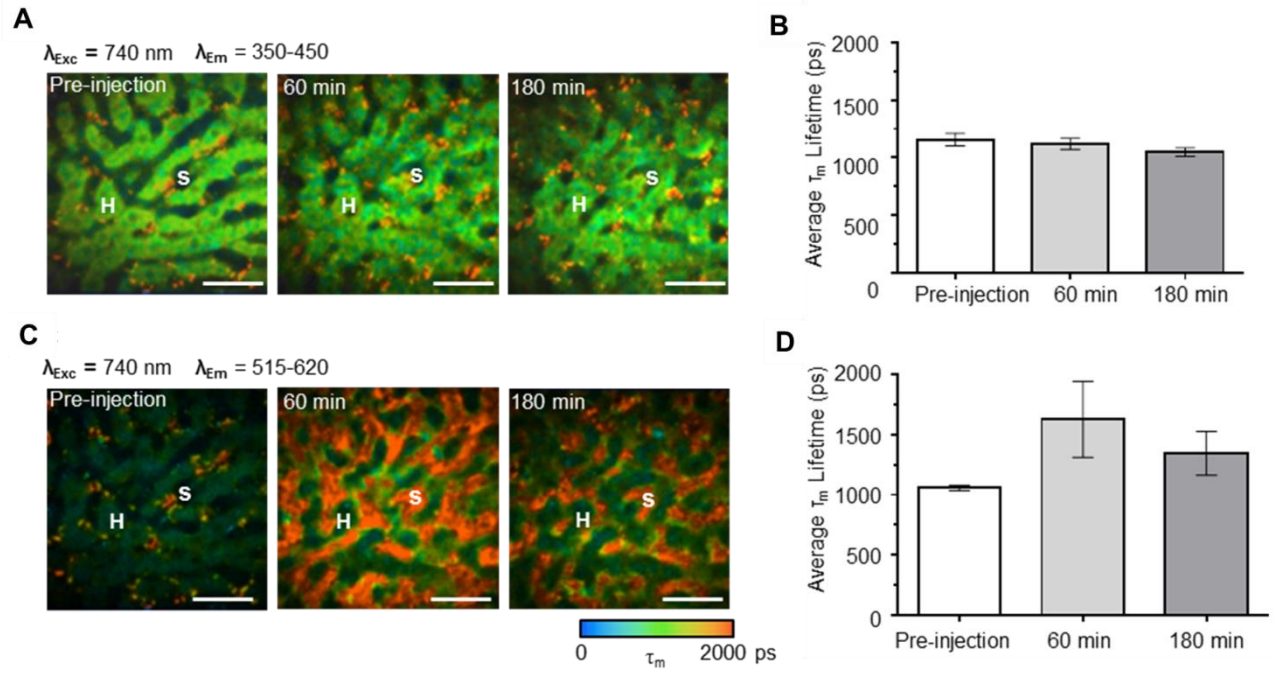

Figure 2.9 FLIM images of representative rat liver before, 60 min and 180 min after QD bolus injection in emission channel of 350–450 nm (a) and 515–620 nm (c). The pseudocolor is based on the average fluorescence lifetime τ_m (0–2000 ps; blue-green-red). (The symbol S indicates sinusoid, H indicates hepatocyte, scale bar: 20 μm). The average τ m values at different time points before and after QDs injection are displayed in (b) (in channel of 350–450 nm) and (d) (in channel of 515–620 nm). The error bar indicates standard deviation (n = 3). Reproduced with permission [63]. 2014. John Wiley and Sons.

2.7.3 Therapeutic cell imaging

Cell therapy has emerged as an evolutionary therapeutic force especially for diseases not curable by traditional therapeutics. Mesenchymal stem cell (MSC) is one of the most promising and widely used therapeutic cells for many debilitating diseases including liver cirrhosis, diabetes, spinal cord injury and myocardial infarction. Recently, a whole body PBPK model has been developed based on the organ disposition and cell-tissue interactions of GFP-expressing MSCs visualised by MPM [72]. This imaging technique opens up a new window for more in-depth investigation about the disposition of molecules, nanoparticles and biological agents in the liver and other organs to understand their in vivo pharmacokinetics and pharmacodynamics.

2.8 Summary, limitation and future direction

A better understanding of the liver anatomy, physiology and pharmacology is necessary for developing new diagnostic and therapeutic strategies for liver diseases. This

fundamental knowledge can be obtained using various techniques, among which the dynamic imaging tools provided by MPM has emerged as a very powerful option to researchers. FLIM adds the abilities of MPM to detect environmental changes and differentiate fluorophores from biological background according to their lifetimes. As summarised in this review, MPM-FLIM has been employed for both *ex vivo* or *in vivo* imaging of the liver. Intravital MPM preserves physiological conditions more faithfully, but it is a demanding technique that requires dedicated personnel. Although most of the aforementioned researches are based on animal studies, MPM has already been applied to clinical settings to diagnose and assess liver diseases.

Limited infiltration depth is one of the most significant limitations of MPM. Normally, the imaging depth is hundreds of micrometers in MPM. Thus early diseases arising deep in the liver tissue are difficult to be diagnosed with this technique. We anticipate that in the near future the penetration depths of MPM will be further increased, and new infrared dyes will be developed with longer excitation wavelengths that penetrate more deeply due to less absorption and scattering. Another limitation is that *in vivo* MPM imaging of the liver can only be achieved after surgical exposure, which grossly impedes its application in humans. Miniaturised laser scanning microscope has been developed, which allows minimal invasive imaging of the liver through keyhole incisions [73]. Endoscope coupled with MPM has also been developed [74], which can image the liver through small surgical incision or intrahepatic bile duct as endoscopic retrograde cholangiopancreatography. These minimal invasive imaging techniques have provided the possibility of *in vivo* imaging the human liver. Therefore, we anticipate that in the near future MPM will be evaluated from bench to bedside, and especially be applied to endoscopic or laparoscopic systems, leading to a deep understanding of the anatomy, physiology and pharmacology of the human liver.

References

[1] Hamel F, Grondin M, Denizeau F, Averill-Bates DA, Sarhan F. Wheat extracts as an efficient cryoprotective agent for primary cultures of rat hepatocytes. Biotechnol Bioeng. 2006;95:661-70.

[2] Wang HL, Thorling CA, Liang XW, Bridle KR, Grice JE, Zhu YA, et al. Diagnostic imaging and therapeutic application of nanoparticles targeting the liver. J Mater Chem B. 2015;3:939-58.

[3] Wisse E, Braet F, Luo D, De Zanger R, Jans D, Crabbe E, et al. Structure and function of sinusoidal lining cells in the liver. Toxicol Pathol. 1996;24:100-11.
[4] Wu J, Zern MA. Hepatic stellate cells: a target for the treatment of liver fibrosis. J Gastroenterol. 2000;35:665-72.
[5] Denk W, Strickler JH, Webb WW. Two-photon laser scanning fluorescence microscopy. Science. 1990;248:73-6.
[6] Straub M, Hell SW. Fluorescence lifetime three-dimensional microscopy with picosecond precision using a multifocal multiphoton microscope. Appl Phys Lett. 1998;73:1769-71.
[7] Thorling CA, Crawford D, Burczynski FJ, Liu X, Liau I, Roberts MS. Multiphoton microscopy in defining liver function. J Biomed Opt. 2014;19.
[8] Tanaka K, Toiyama Y, Okugawa Y, Okigami M, Inoue Y, Uchida K, et al. In vivo optical imaging of cancer metastasis using multiphoton microscopy: a short review. Am J Transl Res. 2014;6:179-87.
[9] Marques PE, Oliveira AG, Chang L, Paula-Neto HA, Menezes GB. Understanding liver immunology using intravital microscopy. J Hepatol. 2015;63:733-42.
[10] Hoover EE, Squier JA. Advances in multiphoton microscopy technology. Nature photonics. 2013;7:93-101.
[11] So PTC, Dong CY, Masters BR, Berland KM. Two-photon excitation fluorescence microscopy. Annu Rev Biomed Eng. 2000;2:399-429.
[12] Gailhouste L, Le Grand Y, Odin C, Guyader D, Turlin B, Ezan F, et al. Fibrillar collagen scoring by second harmonic microscopy: A new tool in the assessment of liver fibrosis. J Hepatol. 2010;52:398-406.
[13] Tang S, Zhou Y, Ju MJ. Multimodal optical imaging with multiphoton microscopy and optical coherence tomography. Journal of biophotonics. 2012;5:396-403.
[14] Small DM, Sanchez WY, Roy S, Hickey MJ, Gobe GC. Multiphoton fluorescence microscopy of the live kidney in health and disease. J Biomed Opt. 2014;19:020901.
[15] Huang S, Heikal AA, Webb WW. Two-photon fluorescence spectroscopy and microscopy of NAD(P)H and flavoprotein. Biophysical journal. 2002;82:2811-25.
[16] Skala MC, Riching KM, Gendron-Fitzpatrick A, Eickhoff J, Eliceiri KW, White JG, et al. In vivo multiphoton microscopy of NADH and FAD redox states, fluorescence lifetimes, and cellular morphology in precancerous epithelia. Proc Natl Acad Sci U S A. 2007;104:19494-9.
[17] Bloembergen N, Pershan PS. Light Waves at Boundary of Nonlinear Media. Phys Rev. 1962;128:606-&.

[18] Tolles WM, Nibler JW, Mcdonald JR, Harvey AB. Review of Theory and Application of Coherent Anti-Stokes Raman-Spectroscopy (Cars). Appl Spectrosc. 1977;31:253-71.
[19] Becker W. Fluorescence lifetime imaging--techniques and applications. J Microsc. 2012;247:119-36.
[20] Blacker TS, Mann ZF, Gale JE, Ziegler M, Bain AJ, Szabadkai G, et al. Separating NADH and NADPH fluorescence in live cells and tissues using FLIM. Nature communications. 2014;5:3936.
[21] Wang HL, Liang XW, Mohammed YH, Thomas JA, Bridle KR, Thorling CA, et al. Real-time histology in liver disease using multiphoton microscopy with fluorescence lifetime imaging. Biomed Opt Express. 2015;6:780-92.
[22] Thorling CA, Liu X, Burczynski FJ, Fletcher LM, Gobe GC, Roberts MS. Multiphoton microscopy can visualize zonal damage and decreased cellular metabolic activity in hepatic ischemia-reperfusion injury in rats. J Biomed Opt. 2011;16.
[23] Li FC, Liang JH, Yang SM, Lee HS, Dong CY. Investigating the effects of Panadol on mouse liver by in rivo multiphoton microscopy. Proc Spie. 2008;6860.
[24] Liang YQ, Shilagard T, Xiao SY, Snyder N, Lau D, Cicalese L, et al. Visualizing Hepatitis C Virus Infections in Human Liver by Two-Photon Microscopy. Gastroenterology. 2009;137:1448-58.
[25] Jayyosi C, Fargier G, Coret M, Bruyere-Garnier K. Photobleaching as a tool to measure the local strain field in fibrous membranes of connective tissues. Acta Biomater. 2014;10:2591-601.
[26] Jayyosi C, Coret M, Bruyere-Garnier K. Characterizing liver capsule microstructure via in situ bulge test coupled with multiphoton imaging. J Mech Behav Biomed Mater. 2016;54:229-43.
[27] Svistounov D, Warren A, McNerney GP, Owen DM, Zencak D, Zykova SN, et al. The Relationship between Fenestrations, Sieve Plates and Rafts in Liver Sinusoidal Endothelial Cells. Plos One. 2012;7.
[28] Marques PE, Amaral SS, Pires DA, Nogueira LL, Soriani FM, Lima BH, et al. Chemokines and mitochondrial products activate neutrophils to amplify organ injury during mouse acute liver failure. Hepatology. 2012;56:1971-82.
[29] Tai DCS, Tan N, Xu S, Kang CH, Chia SM, Cheng CL, et al. Fibro-C-Index: comprehensive, morphology-based quantification of liver fibrosis using second harmonic generation and two-photon microscopy. J Biomed Opt. 2009;14.
[30] Roberts MS, Dancik Y, Prow TW, Thorling CA, Lin LL, Grice JE, et al. Non-invasive imaging of skin physiology and percutaneous penetration using fluorescence spectral and

lifetime imaging with multiphoton and confocal microscopy. Eur J Pharm Biopharm. 2011;77:469-88.
[31] Yan J, Zhuo SM, Chen G, Wu XF, Zhou D, Xie SS, et al. Preclinical study of using multiphoton microscopy to diagnose liver cancer and differentiate benign and malignant liver lesions. J Biomed Opt. 2012;17.
[32] Liu TM, Hsieh CT, Chen YS, Huang FL, Huang HY, Lee WJ, et al. Diagnosing hepatocellular carcinoma with the intensity and the lifetime of two-photon red autofluorescences. Proc Spie. 2011;7903.
[33] Wu YM, Chen HC, Chang WT, Jhan JW, Lin HL, Liau I. Quantitative Assessment of Hepatic Fat of Intact Liver Tissues with Coherent Anti-Stokes Raman Scattering Microscopy. Anal Chem. 2009;81:1496-504.
[34] Dai ZR, Ge GB, Feng L, Ning J, Hu LH, Jin Q, et al. A Highly Selective Ratiometric Two-Photon Fluorescent Probe for Human Cytochrome P450 1A. J Am Chem Soc. 2015;137:14488-95.
[35] Liu Q, Rehman H, Krishnasamy Y, Ramshesh VK, Theruvath TP, Chavin KD, et al. Role of inducible nitric oxide synthase in mitochondrial depolarization and graft injury after transplantation of fatty livers. Free Radic Biol Med. 2012;53:250-9.
[36] Chauvin C, De Oliveira F, Ronot X, Mousseau M, Leverve X, Fontaine E. Rotenone inhibits the mitochondrial permeability transition-induced cell death in U937 and KB cells. J Biol Chem. 2001;276:41394-8.
[37] Rehman H, Ramshesh VK, Theruvath TP, Kim I, Currin RT, Giri S, et al. NIM811 (N-Methyl-4-isoleucine Cyclosporine), a Mitochondrial Permeability Transition Inhibitor, Attenuates Cholestatic Liver Injury but Not Fibrosis in Mice. J Pharmacol Exp Ther. 2008;327:699-706.
[38] Theruvath TP, Snoddy MC, Zhong Z, Lemasters JJ. Mitochondrial permeability transition in liver ischemia and reperfusion: role of c-Jun N-terminal kinase 2. Transplantation. 2008;85:1500-4.
[39] Wang JH, Ahn S, Fischer TD, Byeon JI, Dunn WA, Behrns KE, et al. Autophagy Suppresses Age-Dependent Ischemia and Reperfusion Injury in Livers of Mice. Gastroenterology. 2011;141:2188-U360.
[40] Hu J, Ramshesh VK, McGill MR, Jaeschke H, Lemasters JJ. Low Dose Acetaminophen Induces Reversible Mitochondrial Dysfunction Associated with Transient c-Jun N-Terminal Kinase Activation in Mouse Liver. Toxicol Sci. 2016;150:204-15.

[41] Weiss M, Li P, Roberts MS. An Improved Nonlinear Model Describing the Hepatic Pharmacokinetics of Digoxin: Evidence for Two Functionally Different Uptake Systems and Saturable Binding. Pharm Res-Dordr. 2010;27:1999-2007.
[42] Weiss M, Liu X, Thorling CA, Roberts MS. Functional characterization of hepatic transporters using intravital microscopy. Eur J Pharm Sci. 2013;49:845-9.
[43] Roberts MS, Roberts MJ, Robertson TA, Sanchez W, Thorling C, Zou Y, et al. In vitro and in vivo imaging of xenobiotic transport in human skin and in the rat liver. Journal of biophotonics. 2008;1:478-93.
[44] Liu X , Thorling CA , Jin L, MS R. Intravital multiphoton imaging of rhodamine 123 in the rat liver after intravenous dosing. Intravital. 2012;1:54.
[45] Forster S, Thumser AE, Hood SR, Plant N. Characterization of Rhodamine-123 as a Tracer Dye for Use In In vitro Drug Transport Assays. Plos One. 2012;7.
[46] De Bruyn T, Fattah S, Stieger B, Augustijns P, Annaert P. Sodium Fluorescein is a Probe Substrate for Hepatic Drug Transport Mediated by OATP1B1 and OATP1B3. J Pharm Sci-Us. 2011;100:5018-30.
[47] Thorling CA, Liu X, Burczynski FJ, Fletcher LM, Roberts MS, Sanchez WY. Intravital multiphoton microscopy can model uptake and excretion of fluorescein in hepatic ischemia-reperfusion injury. J Biomed Opt. 2013;18.
[48] Liu Y, Chen HC, Yang SM, Sun TL, Lo W, Chiou LL, et al. Visualization of hepatobiliary excretory function by intravital multiphoton microscopy. J Biomed Opt. 2007;12.
[49] Li FC, Liu Y, Huang GT, Chiou LL, Liang JH, Sun TL, et al. In vivo dynamic metabolic imaging of obstructive cholestasis in mice. Am J Physiol-Gastr L. 2009;296:G1091-G7.
[50] Li FC, Huang GT, Lin CJ, Wang SS, Sun TL, Lo SY, et al. Apical membrane rupture and backward bile flooding in acetaminophen-induced hepatocyte necrosis. Cell Death Dis. 2011;2.
[51] Liu Y, Li FC, Chen HC, Chang PS, Yang SM, Lee HS, et al. In vivo multiphoton imaging of bile duct ligation. Proc Spie. 2008;6860.
[52] Thorling CA, Jin L, Weiss M, Crawford D, Liu X, Burczynski FJ, et al. Assessing Steatotic Liver Function after Ischemia-Reperfusion Injury by In Vivo Multiphoton Imaging of Fluorescein Disposition. Drug Metab Dispos. 2015;43:154-62.
[53] Heymann F, Peusquens J, Ludwig-Portugall I, Kohlhepp M, Ergen C, Niemietz P, et al. Liver inflammation abrogates immunological tolerance induced by Kupffer cells. Hepatology. 2015;62:279-91.

[54] Melgar-Lesmes P, Edelman ER. Monocyte-endothelial cell interactions in the regulation of vascular sprouting and liver regeneration in mouse. J Hepatol. 2015;63:917-25.
[55] Beattie L, Peltan A, Maroof A, Kirby A, Brown N, Coles M, et al. Dynamic Imaging of Experimental Leishmania donovani-Induced Hepatic Granulomas Detects Kupffer Cell-Restricted Antigen Presentation to Antigen-Specific CD8(+) T Cells. Plos Pathog. 2010;6.
[56] Boyum A. Isolation of lymphocytes, granulocytes and macrophages. Scandinavian journal of immunology. 1976;Suppl 5:9-15.
[57] Takeichi T, Engelmann G, Mocevicius P, Schmidt J, Ryschich E. 4-Dimensional Intravital Microscopy: A New Model for Studies of Leukocyte Recruitment and Migration in Hepatocellular Cancer in Mice. J Gastrointest Surg. 2010;14:867-72.
[58] Honda M, Takeichi T, Asonuma K, Tanaka K, Kusunoki M, Inomata Y. Intravital Imaging of Neutrophil Recruitment in Hepatic Ischemia-Reperfusion Injury in Mice. Transplantation. 2013;95:551-8.
[59] Wehr A, Baeck C, Heymann F, Niemietz PM, Hammerich L, Martin C, et al. Chemokine Receptor CXCR6-Dependent Hepatic NK T Cell Accumulation Promotes Inflammation and Liver Fibrosis. J Immunol. 2013;190:5226-36.
[60] Tanaka K, Morimoto Y, Toiyama Y, Okugawa Y, Inoue Y, Uchida K, et al. Intravital dual-colored visualization of colorectal liver metastasis in living mice using two photon laser scanning microscopy. Microsc Res Techniq. 2012;75:307-15.
[61] Tanaka K, Morimoto Y, Toiyama Y, Matsushita K, Kawamura M, Koike Y, et al. In vivo time-course imaging of tumor angiogenesis in colorectal liver metastases in the same living mice using two-photon laser scanning microscopy. J Oncol. 2012;2012:265487.
[62] Thorling CA, Dancik Y, Hupple CW, Medley G, Liu X, Zvyagin AV, et al. Multiphoton microscopy and fluorescence lifetime imaging provide a novel method in studying drug distribution and metabolism in the rat liver in vivo. J Biomed Opt. 2011;16.
[63] Liang XW, Grice JE, Zhu Y, Liu D, Sanchez WY, Li Z, et al. Intravital Multiphoton Imaging of the Selective Uptake of Water-Dispersible Quantum Dots into Sinusoidal Liver Cells. Small. 2015;11:1711-20.
[64] Tanaka K, Okigami M, Toiyama Y, Morimoto Y, Matsushita K, Kawamura M, et al. In vivo real-time imaging of chemotherapy response on the liver metastatic tumor microenvironment using multiphoton microscopy. Oncol Rep. 2012;28:1822-30.
[65] Wang HL, Thorling CA, Liang XW, Bridle KR, Grice JE, Zhu YA, et al. Diagnostic imaging and therapeutic application of nanoparticles targeting the liver. J Mater Chem B. 2015;3:939-58.

[66] Semete B, Booysen L, Lemmer Y, Kalombo L, Katata L, Verschoor J, et al. In vivo evaluation of the biodistribution and safety of PLGA nanoparticles as drug delivery systems. Nanomed-Nanotechnol. 2010;6:662-71.
[67] Cheng SH, Li FC, Souris JS, Yang CS, Tseng FG, Lee HS, et al. Visualizing Dynamics of Sub-Hepatic Distribution of Nanoparticles Using Intravital Multiphoton Fluorescence Microscopy. Acs Nano. 2012;6:4122-31.
[68] Chen AT, Dogdas B, Mehta S, Haskell K, Ng B, Keough E, et al. Quantification of Cy-5 siRNA Signal in the Intra-vital Multi-photon Microscopy Images. Ieee Eng Med Bio. 2012:3712-5.
[69] Stefanello TF, Szarpak-Jankowska A, Appaix F, Louage B, Hamard L, De Geest BG, et al. Thermoresponsive hyaluronic acid nanogels as hydrophobic drug carrier to macrophages. Acta Biomater. 2014;10:4750-8.
[70] Garrett NL, Lalatsa A, Uchegbu I, Schatzlein A, Moger J. Exploring uptake mechanisms of oral nanomedicines using multimodal nonlinear optical microscopy. Journal of biophotonics. 2012;5:458-68.
[71] Liang XW, Wang HL, Grice JE, Li L, Liu X, Xu ZP, et al. Physiologically Based Pharmacokinetic Model for Long-Circulating Inorganic Nanoparticles. Nano Lett. 2016;16:939-45.
[72] Wang HL, Liang XW, Xu ZP, Crawford DHG, Liu X, Roberts MS. A physiologically based kinetic model for elucidating the in vivo distribution of administered mesenchymal stem cells. Sci Rep-Uk. 2016;6.
[73] Alencar H, Mahmood U, Kawano Y, Hirata T, Weissleder R. Novel multiwavelength microscopic scanner for mouse imaging. Neoplasia. 2005;7:977-83.
[74] Kim P, Puoris'haag M, Cote D, Lin CP, Yun SH. In vivo confocal and multiphoton microendoscopy. J Biomed Opt. 2008;13.
[75] Lin J, Lu FK, Zheng W, Xu SY, Tai DA, Yu H, et al. Assessment of liver steatosis and fibrosis in rats using integrated coherent anti-Stokes Raman scattering and multiphoton imaging technique. J Biomed Opt. 2011;16.
[76] Stanciu SG, Xu SY, Peng QW, Yan J, Stanciu GA, Welsch RE, et al. Experimenting Liver Fibrosis Diagnostic by Two Photon Excitation Microscopy and Bag-of-Features Image Classification. Sci Rep-Uk. 2014;4.
[77] Lo W, Liu Y, Chen HC, Yang SM, Sun TL, Chiou LL, et al. Intravital multiphoton microscopy for imaging hepatobiliary function - art. no. 64421R. P Soc Photo-Opt Ins. 2007;6442:R4421-R.

[78] Kleine M, Worbs T, Schrem H, Vondran FWR, Kaltenborn A, Klempnauer J, et al. Helicobacter hepaticus Induces an Inflammatory Response in Primary Human Hepatocytes. Plos One. 2014;9.

Chapter 3

Real-time histology in liver disease using multiphoton microscopy with fluorescence lifetime imaging

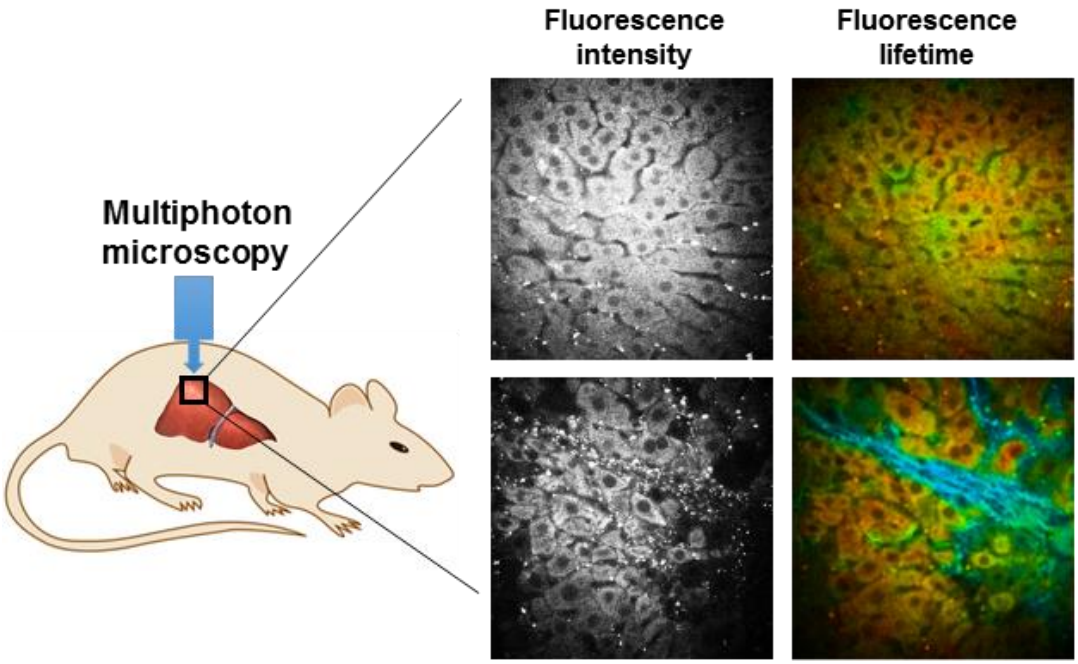

3.1 Synopsis

In this chapter, multiphoton microscopy with fluorescence lifetime imaging was used to image live mice livers (normal, with fibrosis, steatosis, hepatocellular carcinoma and ischemia-reperfusion injury) for stain-free real-time histology. It is able to simultaneously image and quantify the cellular morphology and microenvironment of live livers without conventional biopsy or fluorescent dyes.

The article entitled, “Real-time histology in liver disease using multiphoton microscopy with fluorescence lifetime imaging” has been published by *Biomedical Optics Express*, 2015; 6(3):780-92. The manuscript, figures and tables have been adjusted to fit the overall style of the Thesis and incorporated as this chapter.

3.2 Abstract

Conventional histology with light microscopy is essential in the diagnosis of most liver diseases. Recently, a concept of real-time histology with optical biopsy has been advocated. In this chapter, live mice livers (normal, with fibrosis, steatosis, hepatocellular carcinoma and ischemia-reperfusion injury) were imaged by MPM-FLIM for stain-free real-time histology. The acquired MPM-FLIM images were compared with conventional histological images. MPM-FLIM imaged subsurface cellular and subcellular histopathological hallmarks of live liver in mice models at high resolution. Additional information such as distribution of stellate cell associated autofluorescence and fluorescence lifetime changes was also gathered by MPM-FLIM simultaneously, which cannot be obtained from conventional histology. MPM-FLIM could simultaneously image and quantify the cellular morphology and microenvironment of live livers without conventional biopsy or fluorescent dyes.

Key Words: Real-time histology, Liver disease, Multiphoton microscopy, Fluorescence lifetime imaging

3.3 Introduction

Liver diseases are frequently encountered in clinical practice with high morbidity and mortality [1]. Fatty liver disease is a worldwide health problem and potentially progresses to steatohepatitis, fibrosis and finally cirrhosis [2]. Primary sclerosing cholangitis is a chronic cholestatic liver disease and often develops to liver cirrhosis or even cholangiocarcinoma [3]. Hepatocellular carcinoma is the third leading cause of cancer-related mortality worldwide [4]. Histological examination is essential in the diagnosis of most liver diseases. Conventional histology relies on microscopic examination of a specimen obtained from biopsy or surgery, which is usually time consuming due to the complicated sample preparation procedures including fixation, sectioning and staining. The frozen sections of surgical margin are assessed during hepatocellular carcinoma or cholangiocarcinoma surgery to achieve a R0 resection (complete resection with

microscopic examination of margins showing no tumor cells) [5]. Re-resection and/or re-anastomosis must be performed if the surgical margin is tumor positive, leading to the prolonged operation time. In addition, liver biopsy is often associated with complications such as bleeding or bile leak, and can yield false negative results [6]. There is a desperate need for a rapid, accurate and safe histological diagnosis method for the successful diagnosis and management of liver disease.

Goetz *et al.* has recently reported the application of confocal laser endomicroscopy for the real-time histological examination of liver disease in both animal models and human [7, 8]. This technology allows immediate in vivo subsurface microscopic imaging and has potential to dynamically monitor pathologic events of liver with high resolution. Compared to confocal microscopy, multiphoton microscopy (MPM) has the advantages of less photobleaching and photodamage, and has considerably enhanced imaging penetration depth due to less scattered multiphoton excitation in samples [9]. Fresh, unprocessed and unstained live liver can be imaged *in vivo* or *ex vivo* by MPM with excitation in 700 to 800 nm using intrinsic tissue emissions including two-photon excitation fluorescence (TPEF) and second harmonic generation (SHG) [10].

Fluorescence lifetime imaging (FLIM) coupled with MPM could map the spatial distribution of fluorescence lifetime, the average time of an electron stays in the excited state before returning to the ground state [11]. It can be used to differentiate endogenous fluorophores (*e.g.* nicotinamide adenine dinucleotide (NADH), collagen, and vitamin A) in the liver tissue based on their unique lifetimes. Lifetime changes of these fluorophores reflect changes in liver microenvironment, such as pH, protein binding and injury induced fibrosis, which are usually associated with disease but cannot be revealed by microscopy using fluorescence intensity [9].

Liver tissue obtained from biopsy or surgery of various liver diseases, such as liver fibrosis [12], hepatitis C virus infection [13], hepatocellular carcinoma and cholangiocarcinoma [14] has been examined by MPM. The miniaturized MPM and multiphoton probe have been developed recently [15-17], which allows real-time histological examination of liver without conventional biopsy for liver disease diagnosis. However, there are no systematic studies on MPM features of live normal and diseased livers and comparison of those features with conventional histological examination, and there is no application of MPM-FLIM in the liver disease diagnosis. Therefore, this study aims to establish MPM-FLIM diagnostic features for common liver diseases. Mouse models developed to mimic human liver diseases were examined in this study to explore the feasibility of real-time histology using this new method.

3.4 Materials and Methods

3.4.1 Chemicals and cells

Rodent high fat diet (25% fat, 1% cholesterol and 0.5% cholate) was provided by Specialty Feeds Pty Ltd (SF12-014, Glen Forrest, Western Australia). Carbon tetrachloride (CCl_4) was purchased from Sigma Aldrich (St Louis, MO, US). Ilium xylazile and ketamine hydrochloride were purchased from Bayer Australia (Pymble NSW, Australia). Hepa 1-6 cells were obtained from ATCC (Manassas, VA, USA) and maintained in vitro under cell culture conditions recommended by ATCC.

3.4.2 Animal models

Male 8-week and 20-week-old FVB/N and 8-week-old BALB/c nude mice were purchased from the Animal Resource Centre (Perth, Western Australia). Male 20-week-old *Mdr2-/-* (FVB/N background) mice were purchased from the Jackson Laboratory (Bar Harbor, USA). All animal procedures were approved by the Animal Ethics Committee of the University of Queensland.

Healthy mice (six FVB/N and six BALB/c nude, 20g) served as controls and there were six mice in each liver disease group. FVB/N mice were induced by feeding mice a high fat diet for 14 days before imaging procedure [18]. To study the primary sclerosing cholangitis and biliary fibrosis, 20-week-old *Mdr2-/-* mice were examined. Since the homozygous disruption of the Mdr2 gene in mice causes an insufficient excretion of phospholipids into the bile, the histological features found in *Mdr2-/-* mice are similar to primary sclerosing cholangitis and biliary fibrosis[19]. Chronic chemical hepatic injury and advanced liver fibrosis in BALB/c nude mice was induced by CCl_4 intraperitoneally injection at a dose of 1 mL/kg, dissolved in olive oil (1:4), twice a week for 5 weeks [20]. Hepatocellular carcinoma was induced by intrahepatic implantation of 5×10^6 Hepa1-6 cells into BALB/c nude mice via open surgical technique and imaging procedures were performed after 14 days [21]. Liver ischemia-reperfusion injury was induced by clamping the portal vein and hepatic artery supplying the median and left lobes using a microvascular clamp. After 45 min of partial ischemia, the clamp was removed to allow reperfusion in the liver for 6 h and 12 h.

3.4.3 MPM-FLIM

MPM was performed using the DermaInspect system (Jen-Lab GmbH, Jena, Germany) equipped with an ultrashort (85 fs pulse width) pulsed mode-locked 80-MHz titanium sapphire laser (MaiTai, Spectra Physics, Mount View, California). The excitation wavelength was set to 740 nm for liver autofluorescence and 800 nm for both SHG and autofluorescence signals, with an emission signal range of 350 to 650 nm established through the use of a BG39 bandpass filter (BG39, Schott glass color filter, Schott MG, Mainz, Germany). Images were recorded with water-immersion 10× or oil-immersion 40× objectives (Carl Zeiss, Germany). The laser power was set to 20 or 15 mW for 10× and 40×magnification imaging, respectively, and the acquisition time for obtaining the images was 7.4 s per frame.

For FLIM, a time-correlated single-photon counting (TCSPC) SPC-830 detector (Becker & Hickl, Berlin, Germany) was incorporated into the MPM system. The TCSPC module constructs a photon distribution across the x and y coordinates of the scan area. Fluorescence emission was spectrally resolved between linearly arranged photon counters through the use of dichroic filters in the beam path. The emission light was collected spectrally in a channel from 350 to 450 nm at 740-nm excitation for NADH and 800-nm excitation for NADH and collagen SHG.

Mice were anaesthetized initially by an intraperitoneally injection of ketamine hydrochloride (80 mg/kg) and xylazine (10 mg/kg). Body temperature was controlled by placing mice on a heating pad set to 37°C. A midline laparotomy was performed to expose the liver as previously described [22, 23]. MPM-FLIM images of unfixed live livers were collected within 30 min after surgical procedures started. Normal saline was used to keep the liver moist and attached to the cover glass of ring interfaced to MPM throughout the experiment. Twenty-four images from twelve non-overlapping fields were collected per mouse (twelve acquired with 740 nm excitation and twelve acquired with 800 nm excitation).

3.4.4 Histopathology

Liver specimens from sites of MPM-FLIM imaging were fixed in 4% buffered formalin and embedded in paraffin. Serial sections were obtained for Hematoxylin & Eosin (H&E) stain to evaluate histopathologic changes and Van Gieson’s stain to evaluate fibrosis. The OlyVIA software 2.6 (Olympus, Münster, Germany) was used to visualize and scan the slides.

3.4.5 Data Analysis

Quantitative analysis of the fluorescence intensity images was done using ImageJ 1.44p (National Institutes of Health, USA). Spatial distribution of stellate cells (positive vitamin A-associated autofluorescence) was assessed by densitometric recording of positive sites of fluorescence per frame (10× magnification images) within the periportal, midzonal and centrilobular regions of liver lobules [24]. The area of stellate cells was calculated as percent of the whole liver area of the frame from twelve representative image fields. The fluorescent intensity of injured hepatocytes was calculated from dark area in twelve representative image of diseased liver, and compared to the same extent in those of healthy liver [9]. The nuclear to cytoplasmic ratio was defined as the diameter of the nucleus divided by the diameter of the entire cell (along the same line, arbitrary orientation) [25]. It was measured along three different arbitrary lines within a cell, and tested on eighteen different cells from six representative image fields.

FLIM images were analyzed using SPCImage software 4.9.7 (Becker & Hickl, Berlin, Germany). A bin of two was used in all images when smoothing the decay data prior to fitting. The decay curve is a sum of multiple components as each pixel represents an overlay of emissions from various fluorophores. In this study, a bi-exponential decay model function ($F(t) = \alpha_1 e^{-t/\tau 1} + \alpha_2 e^{-t/\tau 2}$ with $\alpha_1 + \alpha_2 = 1$) was used. Since NADH is the only fluorophore contributing significantly to the data in a given pixel at 740 nm excitation and emission channel from 350 to 450 nm, two lifetimes, τ1 and τ2 could represent the fast and slow decay lifetimes of free and protein-bound NADH, respectively. The amplitudes α1 and α2 represent the relative concentration fraction of NADH [26]. τm is the weighted average lifetime calculated from τ1 and τ2 and their relative amplitudes ($\tau m = \alpha 1 \tau 1 + \alpha 2 \tau 2$). For statistical analysis, one-way ANOVA with Dunnett's test for correction was used to compare the data from normal liver against that from each diseased condition. All the statistical analysis was done using GraphPad Prism v 6.04 (GraphPad Software Inc., La Jolla, California). Results were considered statistically significant with a p-value < 0.05.

3.5 Results

3.5.1 Normal liver

Liver of healthy mice was examined as control. Laser power of 15 to 20 mW was found adequate for imaging. The cellular structure of liver could be imaged deep to 250 μm below the fibrous capsule of Glisson by MPM. We found that imaging depth of 50 μm was the clearest for observing cellular and subcellular morphology (**Fig. 3.1A** and **B**). The stellate cells were smaller in size but had strong vitamin A-associated autofluorescence

(bright dots in **Fig. 3.1A** and **3.2A**), and distributed across the acinus of normal liver uniformly. Bright hepatocyte cords were separated from each other by the blood-filled dark sinusoids (**Fig. 3.2A** and **B**).

3.5.2 Primary sclerosing cholangitis and biliary fibrosis

The livers of 20-week-old *Mdr2-/-* mice showed intercellular fibrosis (**Fig. 3.2F** and **G**), especially around the medium sized to large bile ducts of the periportal region (**Fig. 3.1F** and **G**). Injury of hepatocytes was observed as significantly reduced fluorescence ($p < 0.05$, **Fig. 3.2F**). These morphological changes correlated well with histological results (**Fig. 3.1J** and **3.2J**), and were similar to the primary sclerosing cholangitis and biliary fibrosis. Stellate cells had a normal distribution in 20-week-old *Mdr2-/-* mice.

The mean lifetime excited at 740 nm (1555.7 ± 35.5 ps, **Fig. 3.1H** and **3.2H**) did not show a statistically significant change compared to those of the control group ($p > 0.05$, **Fig. 3.3A**), while that excited at 800 nm (980.0 ± 59.3 ps, **Fig. 3.1I** and **3.2I**) significantly decreased ($p < 0.05$, **Fig. 3.3B**).

3.5.3 Liver with chronic injury and fibrosis

The livers of mice receiving CCl_4 showed signs of hepatocyte damage, which were observed as significantly reduced fluorescence ($p < 0.05$, **Fig. 3.2K**). Collagen deposition was obvious in the centrilobular region and pseudolobular formation was evident in liver (**Fig. 3.1K** and **L**). Inhomogeneous distribution of stellate cells was found only in CCl_4 induced fibrotic liver (**Fig. 3.1K**). The stellate cells reduced in midzonal regions, and accumulated in centrilobular region around central veins ($p < 0.05$). The regional redistribution of stellate cells formed bridges between postsinusoidal venules in some liver lobules (**Fig. 3.1K**). The localisation of stellate cells strongly coincided with that of fibrillar collagen. Hallmarks of hepatocyte damage, including cellular hyaline inclusions, ballooning degeneration and mononuclear cell infiltration, were observed in liver tissue on H&E staining. Liver fibrosis was confirmed by Van Gieson's staining (**Fig. 3.1O** and **3.2O**).

The mean lifetime excited at 740 nm (1443.1 ± 42.7 ps, **Fig. 3.1M** and **3.2M**) was slightly shorter after receiving CCl_4 ($p > 0.05$, **Fig. 3.3A**), while that excited at 800 nm (869.3 ± 132.3 ps, **Fig. 3.1N** and **3.2N**) significantly decreased ($p < 0.05$, **Fig. 3.3B**).

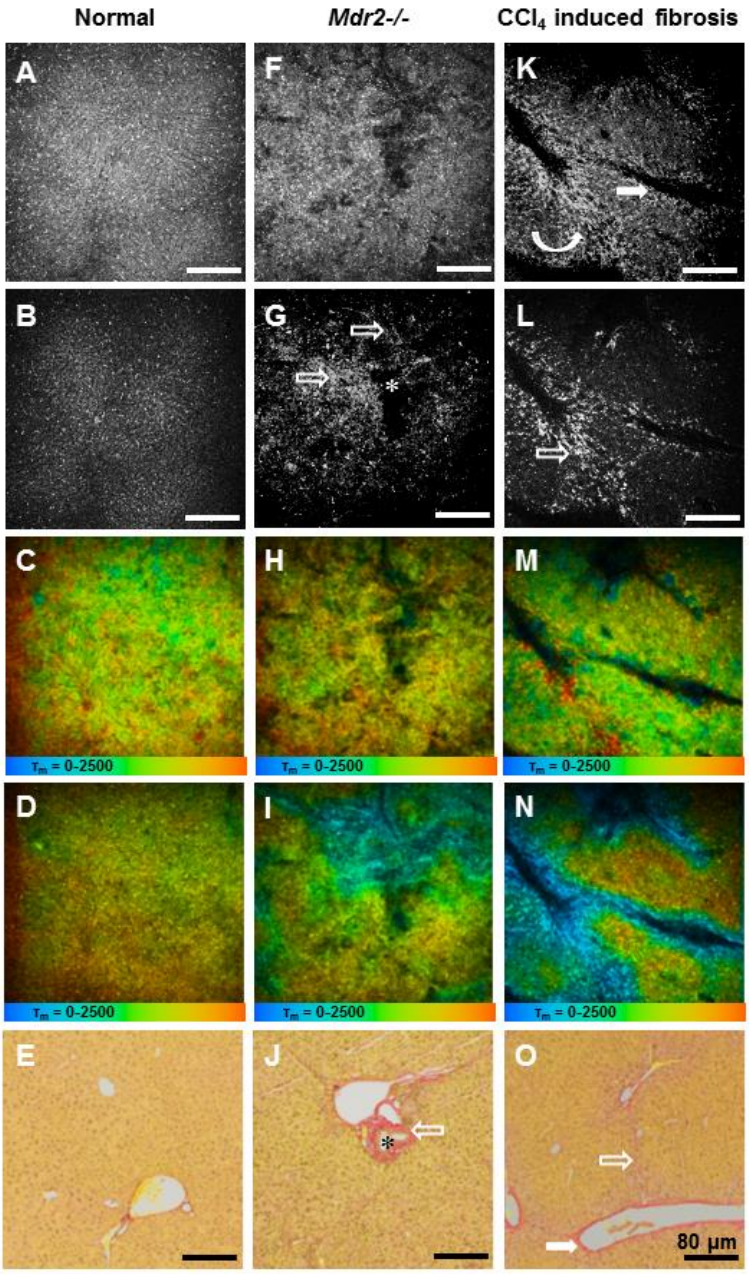

Figure 3.1 MPM-FLIM and conventional histopathological images of liver in healthy mice, *Mdr2-/-* mice and mice with CCl_4 induced liver fibrosis at low magnification (10×) (scale bar: 80 µm). A, F and K. Fluorescence intensity image recorded at $\lambda_{Exc}/\lambda_{Em}$: 740/350 to 650 nm. B, G and L. Fluorescence intensity image recorded at $\lambda_{Exc}/\lambda_{Em}$: 800/350 to 650 nm. C, H and M. Pseudocolored τ_m fluorescence lifetime image (0-2500 ps; blue-green-red) recorded at $\lambda_{Exc}/\lambda_{Em}$: 740/350 to 450 nm. D, I and N. Pseudocolored τ_m fluorescence lifetime image (0-2500 ps; blue-green-red) recorded at $\lambda_{Exc}/\lambda_{Em}$: 800/350 to 450 nm. E, J and O. Conventional histological images were collected on Van Gieson's stained section. Opened arrows indicate collagen, asterisks indicate bile duct, curved arrow indicates bridges formed by stellate cells, and filled arrows indicate postsinusoidal venules.

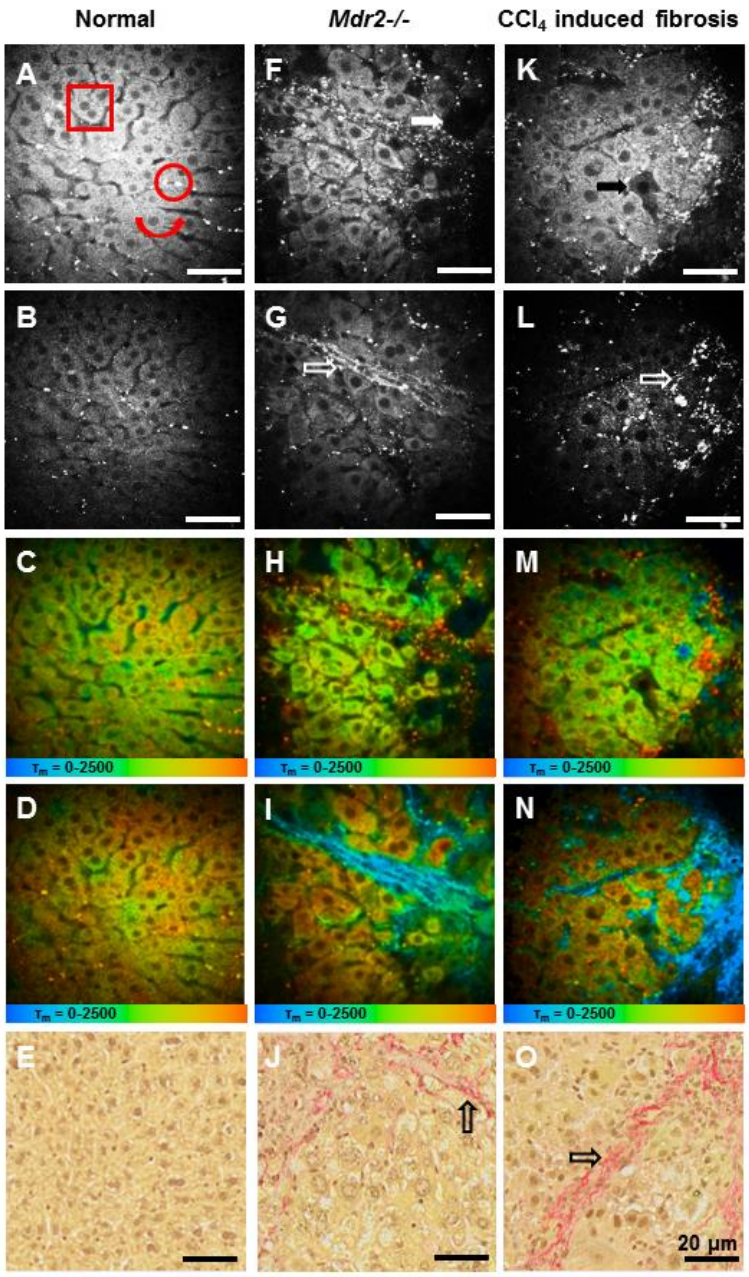

Figure 3.2 MPM-FLIM and conventional histopathological images of liver in healthy mice, *Mdr2-/-* mice and mice with CCl_4 induced liver fibrosis at high magnification (40×) (scale bar: 20 µm). A, F and K. Fluorescence intensity image recorded at $\lambda_{Exc}/\lambda_{Em}$: 740/350 to 650 nm. B, G and L. Fluorescence intensity image recorded at $\lambda_{Exc}/\lambda_{Em}$: 800/350 to 650 nm. C, H and M. Pseudocolored τ_m fluorescence lifetime image (0-2500 ps; blue-green-red) recorded at $\lambda_{Exc}/\lambda_{Em}$: 740/350 to 450 nm. D, I and N. Pseudocolored τ_m fluorescence lifetime image (0-2500 ps; blue-green-red) recorded at $\lambda_{Exc}/\lambda_{Em}$: 800/350 to 450 nm. E, J and O. Conventional histological images were collected on Van Gieson's stained section. Curved arrow indicates hepatic sinusoids, red square indicates hepatocytes, red circle indicates stellate cells associated autofluorescence, opened arrows indicate collagen, and filled arrows indicate cellular necrosis.

3.5.4 Liver with steatosis

In the liver of mice fed with high fat diet, intracellular micro- and macrovesicular steatosis was visualized by MPM. The black intracellular fat vacuole (darker than the nuclei) pushed nuclei of hepatocytes aside towards the cell membrane (**Fig. 3.4A**). The cytoplasm of hepatocytes had a sponge-like appearance because of numerous small black intracellular fat inclusions. These observations correlated well with conventional histology. Intracellular lipid droplets appeared as uncolored circles in liver tissue on H&E staining (**Fig. 3.4E**). No significant fibrosis or inflammatory infiltration was noted.

The mean lifetimes excited at 740 nm (1460.0 ± 65.7 ps, **Fig. 3.4C**) and 800 nm (1028.7 ± 83.1 ps, **Fig. 3.4D**) were slightly shorter than those of the control group, but were not statistically significant ($p > 0.05$, **Fig. 3.3A** and **B**).

3.5.5 Liver with hepatocellular carcinoma

Liver tumor developed in all animals challenged with intrahepatic Hepa1-6 implantation by day 14. Extensive cell heterogeneity characterized by irregular size and shape, increased nuclear to cytoplasmic ratio ($p < 0.05$, **Fig. 3.4F**) and intercellular collagen (**Fig. 3.4G**) resembled the histopathological features of poorly differentiated hepatocellular carcinoma in human. Few stellate cells were observed. Central necrosis of tumor was indicated as areas of significantly reduced fluorescence ($p < 0.05$, **Fig. 3.4F**). Peri-tumoral hepatocytes showed cellular and nuclear pleomorphisms. The conventional histopathological image of fixed H&E (**Fig. 3.4J**) and Van Gieson's stained samples displayed the similar characteristic.

The mean lifetimes excited at 740 nm (1221.4 ± 97.1 ps, **Fig. 3.4H**) and 800 nm (471.7 ± 166.5 ps, **Fig. 3.4I**) decreased significantly in hepatocellular carcinoma compared with those in normal liver ($p < 0.05$, **Fig. 3.3A** and **B**). The lifetimes of free and protein-bound NADH (647.7 ± 20.2 and 2541.7 ± 341.8 ps, respectively), and contribution of protein-bound NADH (32.3 ± 4.0%) also significantly decreased ($p < 0.05$, **Fig. 3.3C**).

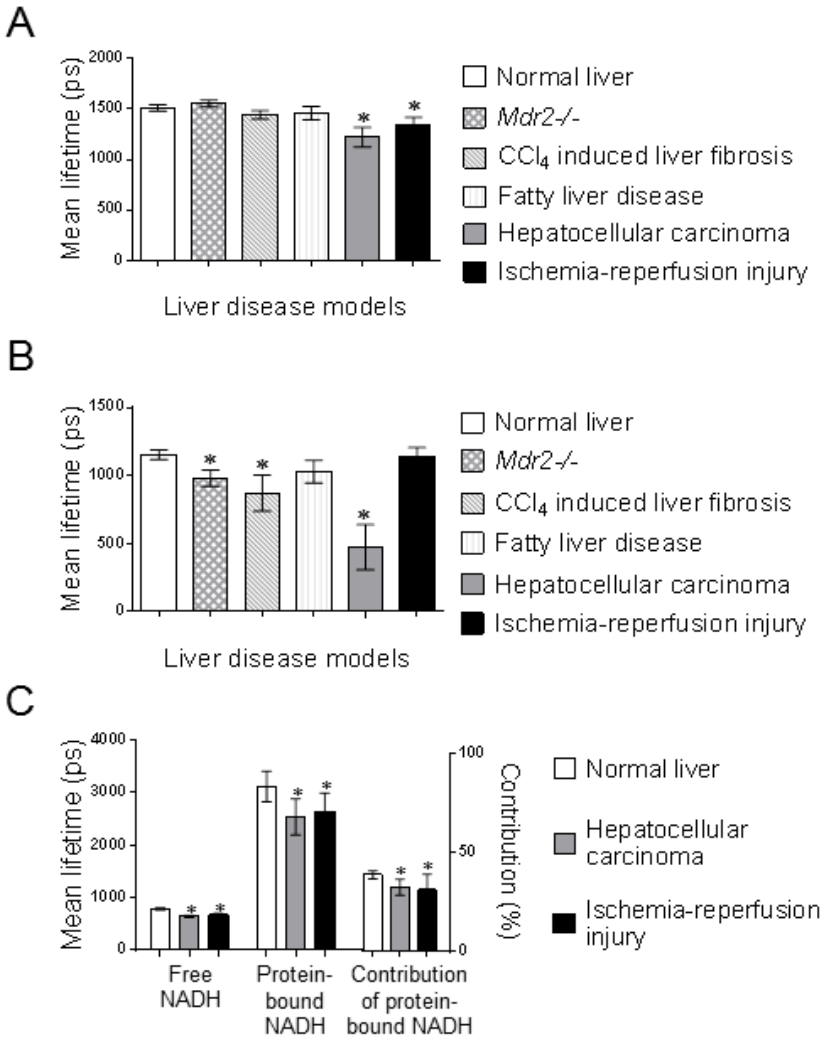

Figure 3.3 Mean and 95% confidence interval of lifetime variables excited at 740 and 800 nm (*n* = 6 for each group). A. Mean lifetime recorded at $\lambda_{Exc}/\lambda_{Em}$: 740/350 to 450 nm. B. Mean lifetime recorded at $\lambda_{Exc}/\lambda_{Em}$: 800/350 to 450 nm. C. The lifetimes of free and protein-bound NADH, and contribution of protein-bound NADH of normal liver, hepatocellular carcinoma and liver with ischemia-reperfusion injury (6 h of reperfusion). Columns, mean of twelve representative images; bars, standard deviation of twelve representative images; *, statistical significance compared with normal liver.

3.5.6 Liver with ischemia-reperfusion injury

Progressive hepatocyte necrosis after ischemia, as indicated by reduced fluorescence and cellular vacuolation, was observed during reperfusion from 6 h ($p < 0.05$, **Fig. 3.4K**) to 12 h. The area of necrosis was about 10% at 6 h and progressed to 25% at 12 h of reperfusion. Liver injury after ischemia, as indicated by hallmarks of oncotic necrosis

including vacuolation and cellular hyaline inclusions, was observed during reperfusion from 6 h to 12h on H&E staining (**Fig. 3.4O**).

The mean lifetimes excited at 740 nm (1344.4 ± 74.9 ps, **Fig. 3.4M**) and 800 nm (1136.3 ± 68.9 ps, **Fig. 3.4N**) decreased significantly in ischemia-reperfusion injury group (6 h of reperfusion) compared with those in normal liver ($p < 0.05$, **Fig. 3.3A** and **B**). The lifetimes of free and protein-bound NADH (671.3 ± 29.0 and 2641.3 ± 355.2 ps, respectively), and contribution of protein-bound NADH (31 ± 7.9%) also significantly decreased ($p < 0.05$, **Fig. 3.3C**).

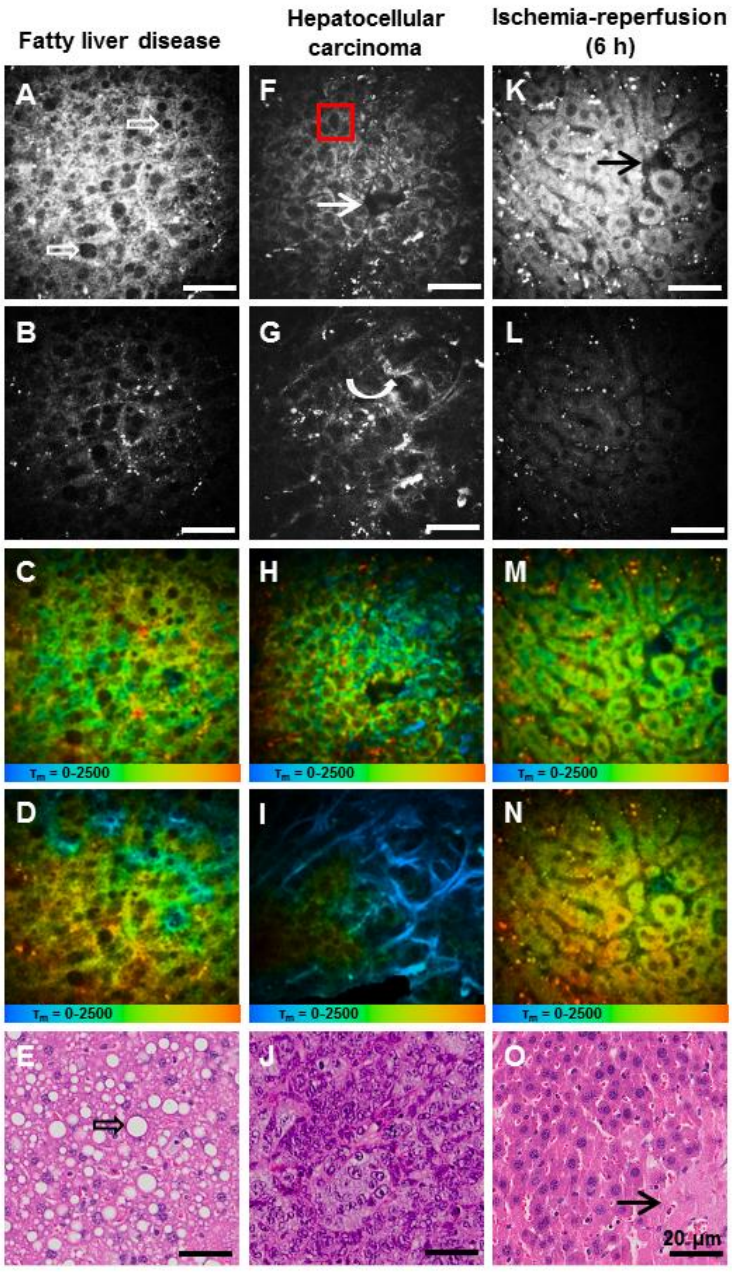

Figure 3.4 MPM-FLIM and conventional histopathological images of liver in mice with fatty liver disease, hepatocellular carcinoma and ischemia-reperfusion injury (6 h of reperfusion) at high magnification (40×) (scale bar: 20 μm). A, F and K. Fluorescence intensity image

recorded at $\lambda_{Exc}/\lambda_{Em}$: 740/350 to 650 nm. B, G and L. Fluorescence intensity image recorded at $\lambda_{Exc}/\lambda_{Em}$: 800/350 to 650 nm. C, H and M. Pseudocolored τm fluorescence lifetime image (0-2500 ps; blue-green-red) recorded at $\lambda_{Exc}/\lambda_{Em}$: 740/350 to 450 nm. D, I and N. Pseudocolored τ_m fluorescence lifetime image (0-2500 ps; blue-green-red) recorded at $\lambda_{Exc}/\lambda_{Em}$: 800/350 to 450 nm. E, J and O. Conventional histological images were collected on H&E stained section. Opened arrows indicate intracellular fat vacuole, red square indicates hepatocellular carcinoma cells with increased nuclear to cytoplasmic ratio, curved arrows indicate collagen, and narrow arrows indicate cellular necrosis.

3.6 Discussion

In this study, we performed the first systematic and comprehensive MPM-FLIM live imaging of livers (normal, with steatosis, fibrosis, hepatocellular carcinoma, and ischemia-reperfusion injury) to assess the potential of MPM-FLIM for real-time histology and diagnosis of liver diseases. Histopathological hallmarks of liver diseases including steatosis, fibrillar collagen deposition, increased nuclear to cytoplasmic ratio and hepatocyte necrosis could be easily characterized from MPM live imaging. Morphological changes observed in MPM images were consistent with conventional histological results. Additional information of cellular microenvironment such as distribution of stellate cell associated autofluorescence and fluorescence lifetime changes could be gathered by MPM-FLIM simultaneously, which could not be obtained from conventional histopathology.

Using channels contained both SHG and autofluorescence signals (800 nm excitation and emission signal from 350 to 450 nm), we have differentiated liver fibrosis caused by primary sclerosing cholangitis or by chronic hepatic injury. Fibrillar collagen deposited in periportal region of liver in *Mdr2-/-* mice while accumulated in centrilobular region of CCl_4 induced fibrotic liver. These MPM findings are consistent with conventional histopathological results in this and previous studies [19, 27]. The SHG makes the specific detection of liver fibrosis possible because there is a strong correlation between SHG signals and fibrillar collagen (type I and III) in liver, while non-fibrillar collagen (type IV) and SHG signals did not correlate [10, 12, 28]. In this study, we found that fluorescence lifetime imaging can be used as a fast and accurate real-time quantification of liver fibrosis. Since collagen SHG response is effectively instantaneous [26, 29], the mean lifetimes decreased in fibrotic liver at excitation of 800 nm (containing both NADH and collagen signals), allowing the discrimination from normal liver. Although the decreases of mean lifetime excited at 800 nm in fibrotic livers were not as obvious as that of hepatocellular carcinoma group, the overall differences were statistically significant. Thus MPM-FLIM would be a

powerful tool providing real-time histology which combines morphology and quantitative evaluation of liver fibrosis simultaneously. Our future work will be focused on analyzing the correlation between the MPM-FLIM results and the Fibrosis-Metavir score, which is currently considered as the gold standard in the assessment of liver fibrosis.

MPM also enables the identification of hepatic stellate cells since these cells store 80% of vitamin A in the whole body [30], and vitamin A absorbs light with wavelength of 765 ± 65 nm and could emit strong fluorescence at below 500 nm under MPM [26]. Current accepted mechanism for the generation of collagen in liver fibrosis is that collagen-producing cells (hepatic stellate cells, portal fibroblasts, and myofibroblasts) are activated by fibrogenic cytokines such as TGF-beta1, angiotensin II, and leptin in the injured liver [31]. However, little information has been revealed about the activity of these cells (such as distribution or proliferation) at the early injury stage. In this study, we observed the stellate cell spatial distribution changed in CCl_4 induced fibrotic liver directly from MPM images, which is consistent with the observation of Vollmar *et al*. using fluorescence microscopy [24]. It is reported that stellate cell accumulation in fibrous septa only occurred early after CCl_4 exposure (1 to 4 weeks) while significant loss of vitamin A storage in liver was found after prolonged periods of CCl_4 administration (8 to 12 weeks) [24]. We suggest that in pathological conditions such as liver fibrosis caused by chronic hepatic injury, the quiescent stellate cells first accumulate in centrilobular region around central veins and between postsinusoidal venules at the early injury stage. Then these cells change into an activated state, synthesize and secrete fibrillar collagen, and finally leading to fibrosis or cirrhosis. While in patients with primary biliary cirrhosis, Cameron *et al.* reported that there was an increase in the total number of lipid vesicles which contain mostly vitamin A in stellate cells, but without spatial redistribution or number increase [3]. These observations best explain why *Mdr2-/-* mice had a normal distribution of vitamin A-associated autofluorescence in this study. Until now, stellate cell numbers and distribution have not been used clinically in diagnosis of liver disease. Although other myofibroblast populations do make a contribution to liver injury, for example portal myofibroblasts are important in cholestasis, only stellate cells could be detected using real-time histology by their distinct vitamin A-associated autofluoresce. In this study, we found that the morphology and distribution of stellate cells imaged by MPM provide valuable information of cellular microenvironment during development of liver fibrosis. This technique might serve as an early and differential diagnostic tool for liver disease in clinic in the foreseeable future.

The nicotinamide moiety of NADH usually absorbs light with wavelength of 340 ± 30 nm (single-photon excition) and could emit fluorescence at 460 ± 50 nm [32]. For MPM-FLIM, images obtained in emission channel 350-450 nm under 740 nm excitation mainly reflect the fluorescence lifetime of NADH, which is sensitive to the changes in the cellular energy metabolism and microvascular oxygen supply [25]. Free NADH is mainly located in the cytoplasm, and involved in adenosine triphosphate (ATP) synthesis without oxygen in glycolysis, while protein-bound NADH is located in mitochondrial membrane, producing ATP in aerobic conditions [9, 33]. The free and protein-bound forms of NADH have similar excitation and emission wavelengths, but can be separated by their distinct fluorescence lifetimes [34]. In our study, lifetime of free and protein-bound NADH, and contribution of protein-bound NADH significantly decreased in hepatocellular carcinoma and liver with ischemia-reperfusion injury. Previous studies have found that the lifetime of free and protein-bound NADH, and the relative contribution of protein-bound NADH decreased with hypoxia [25, 34]. Changes in cellular metabolic pathways and the distribution of NADH enzyme binding sites may be responsible for decrease of protein-bound NADH lifetime in hypoxia [35]. In carcinoma and ischemia, cellular respiration is shifted to glycolysis, producing ATP in anaerobic conditions rather than oxidative phosphorylation for ATP production [36, 37]. So the measured decreases in NADH lifetimes and the contribution of protein-bound NADH in hepatocellular carcinoma and the liver with ischemia-reperfusion injury are consistent with the increased levels of glycolysis in neoplastic and ischemia injured cells. We also found the mean lifetimes of NADH in fatty liver disease and CCl4 induced fibrotic liver were slight shorter than those of the control group, but without statistical significance. One possible reason might be the hypoxia in fatty liver or fibrotic liver was not as severe as that in hepatocellular carcinoma and liver ischemia-reperfusion injury.

Current limitations of MPM-FLIM include limited infiltration depth. First, cellular and subcellular details were clearest at 50 μm below the capsule of Glisson and the maximum depth was 250 μm in our study. Thus early diseases arising deep in the liver tissue are difficult to be diagnosed with this technique. We anticipate that in the near future MPM-FLIM will be applicable to endoscopic retrograde cholangiopancreatography (ERCP) to image liver lesions from intrahepatic bile duct. The second limitation is that FLIM scan was performed using a long-time exposure of 7.4 s. Moving artefacts, such as respiration, would decrease the image quality. However, our group found most MPM-FLIM images were of excellent quality in rats in vivo [9]. This technique thus bears a great potential to permit laparoscopic real-time histology of liver diseases in human. Third, infiltration of

inflammatory cells is a vital component of most liver diseases and is scored in all current histopathology scoring systems. Fluorescent dyes have to be administrated to provide real-time differentiation of inflammatory cells using MPM-FLIM. So until now, this technique may not totally replace biopsy.

In summary, this study demonstrates for the first time that MPM-FLIM is able to simultaneously image and quantify the cellular morphology and microenvironment of live livers without conventional biopsy or fluorescent dyes. We established a reliable and standardized method of real-time histology for liver diseases with optical biopsy and compared conventional histopathology, which is considered as the gold standard in the clinical assessment of liver disease currently. Although MPM-FLIM may not totally replace biopsy now, we anticipate that in the near future this technique will be evaluated from bench to bedside, and especially be applied to endoscopic or laparoscopic systems, leading to a less invasive real-time histology of liver diseases.

References

[1] Uhl P, Fricker G, Haberkorn U, Mier W. Current status in the therapy of liver diseases. Int J Mol Sci. 2014;15:7500-12.

[2] Sass DA, Chang P, Chopra KB. Nonalcoholic fatty liver disease: a clinical review. Digestive diseases and sciences. 2005;50:171-80.

[3] Cameron RG, Neuman MG, Shear N, Blendis LM. Multivesicular stellate cells in primary biliary cirrhosis. Hepatology (Baltimore, Md). 1997;26:819-22.

[4] Jemal A, Siegel R, Ward E, Hao Y, Xu J, Murray T, et al. Cancer statistics, 2008. CA: a cancer journal for clinicians. 2008;58:71-96.

[5] Wang H, Wang H, Chen T, Liang X, Song Y, Wang J. Evaluation of the POSSUM, P-POSSUM and E-PASS scores in the surgical treatment of hilar cholangiocarcinoma. World J Surg Oncol. 2014;12:191.

[6] Schneider AR, Benz C, Adamek HE, Jakobs R, Riemann JF, Arnold JC. Minilaparoscopy versus conventional laparoscopy in the diagnosis of hepatic diseases. Gastrointestinal endoscopy. 2001;53:771-5.

[7] Goetz M, Vieth M, Kanzler S, Galle PR, Delaney P, Neurath MF, et al. In vivo confocal laser laparoscopy allows real time subsurface microscopy in animal models of liver disease. Journal of hepatology. 2008;48:91-7.

[8] Goetz M, Kiesslich R, Dienes HP, Drebber U, Murr E, Hoffman A, et al. In vivo confocal laser endomicroscopy of the human liver: a novel method for assessing liver microarchitecture in real time. Endoscopy. 2008;40:554-62.
[9] Thorling CA, Liu X, Burczynski FJ, Fletcher LM, Gobe GC, Roberts MS. Multiphoton microscopy can visualize zonal damage and decreased cellular metabolic activity in hepatic ischemia-reperfusion injury in rats. Journal of biomedical optics. 2011;16:116011.
[10] Zipfel WR, Williams RM, Webb WW. Nonlinear magic: multiphoton microscopy in the biosciences. Nature biotechnology. 2003;21:1369-77.
[11] Lakowicz JR, Szmacinski H, Nowaczyk K, Berndt KW, Johnson M. Fluorescence lifetime imaging. Analytical biochemistry. 1992;202:316-30.
[12] Gailhouste L, Le Grand Y, Odin C, Guyader D, Turlin B, Ezan F, et al. Fibrillar collagen scoring by second harmonic microscopy: a new tool in the assessment of liver fibrosis. Journal of hepatology. 2010;52:398-406.
[13] Liang Y, Shilagard T, Xiao SY, Snyder N, Lau D, Cicalese L, et al. Visualizing hepatitis C virus infections in human liver by two-photon microscopy. Gastroenterology. 2009;137:1448-58.
[14] Yan J, Zhuo S, Chen G, Wu X, Zhou D, Xie S, et al. Preclinical study of using multiphoton microscopy to diagnose liver cancer and differentiate benign and malignant liver lesions. Journal of biomedical optics. 2012;17:026004.
[15] Bird D, Gu M. Two-photon fluorescence endoscopy with a micro-optic scanning head. Optics letters. 2003;28:1552-4.
[16] Tang S, Jung W, McCormick D, Xie T, Su J, Ahn YC, et al. Design and implementation of fiber-based multiphoton endoscopy with microelectromechanical systems scanning. Journal of biomedical optics. 2009;14:034005.
[17] Rivera DR, Brown CM, Ouzounov DG, Webb WW, Xu C. Multifocal multiphoton endoscope. Optics letters. 2012;37:1349-51.
[18] Anstee QM, Goldin RD. Mouse models in non-alcoholic fatty liver disease and steatohepatitis research. International journal of experimental pathology. 2006;87:1-16.
[19] Mauad TH, van Nieuwkerk CM, Dingemans KP, Smit JJ, Schinkel AH, Notenboom RG, et al. Mice with homozygous disruption of the mdr2 P-glycoprotein gene. A novel animal model for studies of nonsuppurative inflammatory cholangitis and hepatocarcinogenesis. The American journal of pathology. 1994;145:1237-45.
[20] Vidal I, Richert L. The nude mouse as model for liver deficiency study and treatment and xenotransplantation. International journal of hepatology. 2012;2012:140147.

[21] Wang Q, Luan W, Goz V, Burakoff SJ, Hiotis SP. Non-invasive in vivo imaging for liver tumour progression using an orthotopic hepatocellular carcinoma model in immunocompetent mice. Liver international : official journal of the International Association for the Study of the Liver. 2011;31:1200-8.
[22] Thorling CA, Jin L, Weiss M, Crawford D, Liu X, Burczynski FJ, et al. Assessing steatotic liver function after ischemia-reperfusion injury by in vivo multiphoton imaging of fluorescein disposition. Drug metabolism and disposition: the biological fate of chemicals. 2015;43:154-62.
[23] Liang X, Grice JE, Zhu Y, Liu D, Sanchez WY, Li Z, et al. Intravital Multiphoton Imaging of the Selective Uptake of Water-Dispersible Quantum Dots into Sinusoidal Liver Cells. Small (Weinheim an der Bergstrasse, Germany). 2014.
[24] Vollmar B, Siegmund S, Menger MD. An intravital fluorescence microscopic study of hepatic microvascular and cellular derangements in developing cirrhosis in rats. Hepatology (Baltimore, Md). 1998;27:1544-53.
[25] Skala MC, Riching KM, Gendron-Fitzpatrick A, Eickhoff J, Eliceiri KW, White JG, et al. In vivo multiphoton microscopy of NADH and FAD redox states, fluorescence lifetimes, and cellular morphology in precancerous epithelia. Proceedings of the National Academy of Sciences of the United States of America. 2007;104:19494-9.
[26] Roberts MS, Dancik Y, Prow TW, Thorling CA, Lin LL, Grice JE, et al. Non-invasive imaging of skin physiology and percutaneous penetration using fluorescence spectral and lifetime imaging with multiphoton and confocal microscopy. European journal of pharmaceutics and biopharmaceutics : official journal of Arbeitsgemeinschaft fur Pharmazeutische Verfahrenstechnik eV. 2011;77:469-88.
[27] Thomas JA, Pope C, Wojtacha D, Robson AJ, Gordon-Walker TT, Hartland S, et al. Macrophage therapy for murine liver fibrosis recruits host effector cells improving fibrosis, regeneration, and function. Hepatology (Baltimore, Md). 2011;53:2003-15.
[28] Boulesteix T, Pena AM, Pages N, Godeau G, Sauviat MP, Beaurepaire E, et al. Micrometer scale ex vivo multiphoton imaging of unstained arterial wall structure. Cytometry Part A : the journal of the International Society for Analytical Cytology. 2006;69:20-6.
[29] Becker W. Fluorescence lifetime imaging--techniques and applications. Journal of microscopy. 2012;247:119-36.
[30] Senoo H. Structure and function of hepatic stellate cells. Medical electron microscopy : official journal of the Clinical Electron Microscopy Society of Japan. 2004;37:3-15.

[31] Bataller R, Brenner DA. Liver fibrosis. The Journal of clinical investigation. 2005;115:209-18.
[32] Blacker TS, Mann ZF, Gale JE, Ziegler M, Bain AJ, Szabadkai G, et al. Separating NADH and NADPH fluorescence in live cells and tissues using FLIM. Nature communications. 2014;5:3936.
[33] Wang HW, Gukassyan V, Chen CT, Wei YH, Guo HW, Yu JS, et al. Differentiation of apoptosis from necrosis by dynamic changes of reduced nicotinamide adenine dinucleotide fluorescence lifetime in live cells. Journal of biomedical optics. 2008;13:054011.
[34] Bird DK, Yan L, Vrotsos KM, Eliceiri KW, Vaughan EM, Keely PJ, et al. Metabolic mapping of MCF10A human breast cells via multiphoton fluorescence lifetime imaging of the coenzyme NADH. Cancer research. 2005;65:8766-73.
[35] Banerjee S, Bhatt DK. Histochemical studies on the distribution of certain dehydrogenases in squamous cell carcinoma of cheek. Indian journal of cancer. 1989;26:21-30.
[36] Schroeder T, Yuan H, Viglianti BL, Peltz C, Asopa S, Vujaskovic Z, et al. Spatial heterogeneity and oxygen dependence of glucose consumption in R3230Ac and fibrosarcomas of the Fischer 344 rat. Cancer research. 2005;65:5163-71.
[37] Kannerup AS, Gronbaek H, Funch-Jensen P, Jorgensen RL, Mortensen FV. The influence of preconditioning on metabolic changes in the pig liver before, during, and after warm liver ischemia measured by microdialysis. Hepatol Int. 2009;3:310-5.

Chapter 4

Dual-mode quantitative imaging of cellular oxidative stress for predicting drug response in liver injury

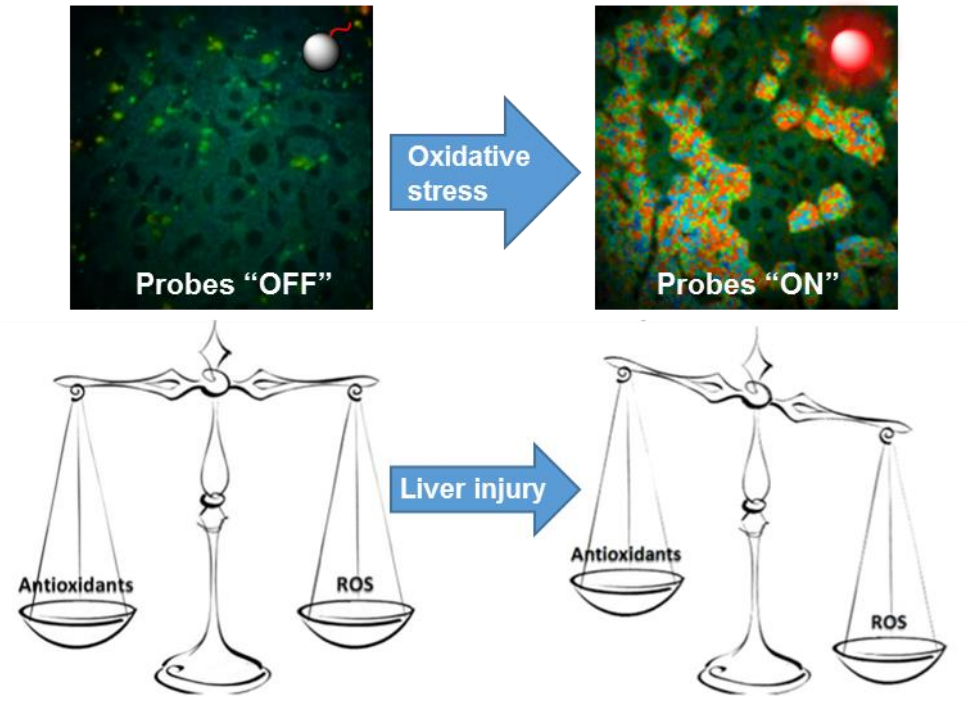

4.1 Synopsis

In this chapter, the fluctuations of cellular oxidative stress during liver injury were investigated at the single cell-level resolution. By combining fluorescence intensity imaging and fluorescence lifetime imaging, we totally removed any possibility of crosstalk from in vivo environmental or instrumental factors, and accurately localised and measured the changes in oxidative stress within the liver.

The article entitled, “Two-photon dual imaging platform for in vivo monitoring cellular oxidative stress in liver injury” has been published by *Scientific Reports*, 2017; 7: 45374. The manuscript, figures and tables have been adjusted to fit the overall style of the Thesis and incorporated as this chapter.

4.2 Abstract

Oxidative stress reflects an imbalance between reactive oxygen species (ROS) and antioxidants, which has been reported as an early unifying event in the development and progression of various diseases and as a direct and mechanistic indicator of treatment response. However, highly reactive and short-lived nature of ROS and antioxidant limited conventional detection agents, which are influenced by many interfering factors. This chapter investigated the fluctuations of cellular oxidative stress during liver injury at the single cell-level resolution. By combining fluorescence intensity imaging and fluorescence lifetime imaging, we totally remove any possibility of crosstalk from *in vivo* environmental or instrumental factors, and accurately localised and measured the changes in ROS and glutathione (GSH) within the liver. This precedes changes in conventional biochemical and histological assessments in two distinct experimental murine models of liver injury. The ability to monitor real-time cellular oxidative stress with dual-modality imaging has significant implications for high-accurate, spatially configured and quantitative assessment of metabolic status and drug response.

Key Words: Oxidative stress, Liver injury, Multiphoton microscopy, Fluorescence lifetime imaging

4.3 Introduction

Oxidative stress has been reported as an early unifying event in the development and progression of various diseases including injury [1, 2], cancer [3], and many inflammatory diseases [4]. It reflects an imbalance between the production of reactive oxygen species (ROS) and antioxidant defenses, such as glutathione (GSH) [5]. Excessive production of ROS damages all components of the cell, including lipids, proteins, and DNA. Some ROS, including hydrogen peroxide (H_2O_2) and hypochlorous acid (HOCl), also act as cellular messengers, and can cause disruptions in normal mechanisms of cellular signaling [5]. While GSH, the major ROS-scavenging system in cells to reduce ROS stress, can detoxify the reactive intermediates and repair the resulting damage. Because ROS and

antioxidants have distinct sources of production and are particularly sensitive to upstream molecular interventions [6], their detection at the single cell-level resolution could be useful for identifying subpopulations of cells with different susceptibility to ROS-induced injury in different stages of diseases. Moreover, the oxidative stress endpoints can report early and molecular changes due to treatment [7], and have potential to serve as powerful biomarkers of drug response. For example, in liver diseases, the primary endpoint of drug efficacy is functional recovery of hepatocytes. The current treatment evaluations include imaging liver morphology, monitoring blood levels of liver enzymes, bilirubin and markers of inflammation, and assessing the signs and symptoms [8]. Yet each of these current techniques fails to capture dynamic changes in metabolic state and poorly reflects sensitivity to drug efficacy. Cellular and molecular changes of hepatocytes precede changes in liver morphology or markers in peripheral blood during treatment. If these molecular endpoints can be identified and measured, they would provide powerful biomarkers for early-drug response.

Methods to detect oxidative stress *in vivo* have encountered technical challenges, which prevented implementation of this method for preclinical drug efficacy screening [2, 9]. A number of GSH and ROS-detection probes have been developed [9-13]. Most of them are single-mode intensity-based probes, which can provide quantitative results, but may often be influenced by fluid optical properties, endogenous fluorophores, probe concentration, and other *in vivo* environmental or instrumental factors. The fluorescence lifetime of probes are independent of these interfering factors, offering accurate and ultrasensitive detecting the presence of many components of cell signaling pathways [14]. Thus, the combination of fluorescence intensity imaging and fluorescence lifetime imaging (FLIM) is an ideal procedure for intracellular oxidative stress investigations with high reliability and accuracy. Up to now, however, no such dual-mode probe has been developed for *in vivo* real-time molecular imaging. We have previously synthesized a transition-metal complex-based sensing platform for detecting cellular GSH and ROS levels *in vitro* [15-18]. This sensing platform consists of three probes, which exhibit favorable photophysical properties including high photostability, selective and quantitative response. To further investigate the fluorescence lifetime and two-photon absorption behavior of this platform, and advance to monitoring multiple analytes at the single cell-level resolution in living systems, here we combined fluorescence intensity imaging and FLIM to detect oxidative stress in the liver of living mice using this sensing platform. We investigated this approach as a tool for monitoring cellular oxidative stress to predict drug response in two of the most common types of liver injury: acetaminophen (APAP)-induced

liver injury, which accounts for approximately one-half of all acute liver failures in the western world today [19], and hepatic ischemia-reperfusion (I/R) injury, which often occurs during liver resection and liver transplantation [20]. The drug response predicted by cellular oxidative stress was further compared with alanine aminotransferase (ALT) levels in blood and histological examination of the liver. This work represents a significant advancement in the tools available to study cellular metabolism and predict drug response in living systems.

4.4 Materials and Methods

4.4.1 Chemicals and cells

All chemicals were obtained from Sigma-Aldrich (St Louis, MO, USA) unless otherwise stated. Bromobimane was purchased from Santa Cruz (Santa Cruz, California, USA). PBS was purchased from Invitrogen (Carlsbad, CA, USA). The GSH-detection probe (P-GSH), H_2O_2-detection probe (P-HP) and HOCl-detection probe (P-HA) were synthesised according to the literature [15-18]. AML12 cells were obtained from ATCC (Manassas, VA, USA) and maintained *in vitro* under cell culture conditions recommended by ATCC.

4.4.2 *In vitro* characterisation

Two-photon absorption spectrum was recorded using DermaInspect system (Jen-Lab GmbH, Jena, Germany). The power (15 mW) and laser pulses (80-MHz and 85 fs pulse width) were adjusted under the chosen measurement conditions that were kept constant throughout this study. Emission spectra were measured on a Perkin-Elmer LS 50B fluorescence spectrometer with excitation and emission slits of 10 nm. To determine optical responses of probes toward different GSH, H_2O_2 and HOCl in solution, the fluorescence intensities (λ_{ex} = 850 nm, λ_{em} = 515 to 620 nm) of the P-GSH, P-HP and P-HA (10 μM) in PBS (30 mM, pH = 7.4) were measured 5 min after the addition of GSH, H_2O_2 and HOCl to determine the intensity enhancement. Emission lifetimes were measured on an ISS-Chronos multifrequency cross-correlation phase and modulation lifetime spectrometer (ISS Inc., Champaign, IL, USA). For examining the applicability of probes for detecting cellular GSH and ROS levels using FLIM imaging, 1×10^5 AML12 cells per well were plated in 12 well plates and incubated for 24 h at 37 °C and 5% CO_2. To remove the intracellular GSH, cells were incubated in serum free medium containing N-ethylmaleimide (100 μM) for 1 h at 37 °C in the incubator. Cells were then exposed to 30

mM of P-GSH in serum free medium and incubated for 2 h in the same conditions. To investigate the photostability of P-GSH, P-HP and P-HA, these probes were incubated in PBS or GSH, H_2O_2 and HOCl under irradiation with a 30 W deuterium lamp (one-photon spectrum: 85 to 400 nm) at room temperature. FLIM imaging was performed using DermaInspect system (Jen-Lab GmbH, Jena, Germany) equipped with an ultrashort (85 fs pulse width) pulsed mode-locked 80-MHz titanium sapphire laser (MaiTai, Spectra Physics, Mount View, CA, USA) and a time-correlated single-photon counting (TCSPC) SPC-830 detector (Becker & Hickl, Berlin, Germany). The excitation wavelength was set to 740 nm for autofluorescence and 850 nm for probe signals, with emission signal ranges of 350 to 450 nm and 515 to 620 nm established respectively through the use of BG39 bandpass filters (BG39, Schott glass color filter, Schott MG, Mainz, Germany). Images were recorded with oil-immersion × 40 objectives (Carl Zeiss, Oberkochen, Germany). The laser power was set to 15 mW for× 40 magnification imaging, and the acquisition time for obtaining the images was 7.4 seconds per frame. Fluorescence emission was spectrally resolved between linearly arranged photon counters through the use of dichroic filters in the beam path.

4.4.3 Animal models

Male 8-week-old BALB/c mice were purchased from the Animal Resource Centre (Perth, Western Australia). All animal procedures were approved by the Animal Ethics Committee of the University of Queensland and were carried out in accordance with Australian Code for the Care and Use of Animals for Scientific Purposes 8th edition. For APAP-induced liver injury, mice received gavage of 500 mg/kg APAP in 0.9% saline. Liver ischemia-reperfusion injury was induced by clamping the portal vein and hepatic artery supplying the median and left lobes using a microvascular clamp. After 45 min of partial ischemia, the clamp was removed to allow reperfusion in the liver. For drug efficacy studies, animals were treated with 150 mg/kg of NAC intravenously 45 min after APAP administration [2], and 200 mg/kg of GSH or 150 mg/kg of NAC intravenously 45 min before liver ischemia [21].

4.4.4 *In vivo* imaging of GSH and ROS

Mice were anaesthetized initially by the intraperitoneal injection of ketamine hydrochloride (80 mg/kg) and xylazine (10 mg/kg). Body temperature was controlled by placing mice on a heating pad set to 37°C. Intravital imaging of the mouse liver was

performed as previously described [22, 23]. Briefly, a midline laparotomy is performed and the liver is exposed for imaging. The left lobe of the liver is placed on the metal plate, which was slightly raised above the intraperitoneal cavity to minimize pressure on the organs underneath. Normal saline was used to keep the liver moist and attached to the cover glass throughout the experiment. 50 μM of probe suspended in 0.2 mL PBS was injected with a 27 gauge needle into the portal vein. Multiphoton imaging was performed using the Lavision Biotec Nikon multiphoton microscopy (LaVision BioTec, Bielefeld, Germany) and DermaInspect system (Jen-Lab GmbH, Jena, Germany) equipped with an ultrashort (85 fs pulse width) pulsed mode-locked 80-MHz titanium sapphire laser (MaiTai, Spectra Physics, Mount View, CA, USA). The excitation wavelength was set to 740 nm for organ autofluorescence and 850 nm for probe signals, with emission signal ranges of 350 to 450 nm and 515 to 620 nm established respectively through the use of BG39 bandpass filters (BG39, Schott glass color filter, Schott MG, Mainz, Germany). Images were recorded with water-immersion × 10 or oil-immersion × 40 objectives (Carl Zeiss, Oberkochen, Germany). The laser power was set to 20 or 15 mW for × 10 or × 40 magnification imaging, and the acquisition time for obtaining the images was 7.4 seconds per frame. For FLIM, a time-correlated single-photon counting (TCSPC) SPC-830 detector (Becker & Hickl, Berlin, Germany) was incorporated into the DermaInspect system. The TCSPC module constructs a photon distribution across the x and y coordinates of the scan area. Fluorescence emission was spectrally resolved between linearly arranged photon counters through the use of dichroic filters in the beam path. The emission light was collected spectrally in a channel from 515 to 620 nm at 850-nm excitation. Imaging depth of 50 to 100 μm below the fibrous capsule of Glisson were chosen and kept constant throughout this study. Twenty-four images from twelve non-overlapping fields were collected per mouse (n = 5) without the use of randomization and blinding.

FLIM images were analysed using SPCImage software 4.9.7 (Becker & Hickl, Berlin, Germany). The fluorescence intensity decay curve of each pixel was fitted to a bi-exponential decay model: $F(t) = \alpha_1 e^{-t/\tau 1} + \alpha_2 e^{-t/\tau 2} + C$. Two lifetimes, τ_1 and τ_2 represent the fast and slow decay lifetimes; α_1 and α_2 are the corresponding relative amplitude coefficients, where $\alpha_1 + \alpha_2 = 1$. C is a constant related to the level of background light present and the contribution from all preceding excitation pulses (the '*offset*'-signals). When excited by laser pulses with an 80 MHz repetition rate, the slow decay fluorescence of the long-lifetime fluorescent probes for hundreds of excitation pulses accumulates and forms a quasi-continuous background. This background is significantly larger than the background caused by possible incomplete decay of endogenous fluorescence. The

‘*offset*’-signals of reacted probes and the cellular autofluorescence (‘*offset*’ parameter within BH SPCImage determines the baseline of the fluorescence decay curve) were adjusted under the chosen measurement conditions that were kept constant throughout this study. Since the fluorescence decay of reacted probes is slow compared to the measurement time window which is defined by the repetition rate of the laser system, the “Incomplete Model” in SPCImage software was used for calculation according to the software handbook.

4.4.5 Single-cell analysis of images

The cellular-level image analysis was done using ImageJ 1.44p (National Institutes of Health, USA) and Cell Profiler 2.1.0 in Matlab R2015a (The MathWorks Inc.). Grayscale FLIM images were imported and cell pixels were smoothed. The resulting round objects between 30 and 70 pixels in diameter were segmented and saved as the cell within the image. An Otsu Global threshold was used to improve propagation and prevent propagation into background pixels. Then corresponding fluorescence intensity images were imported. Subpopulation analysis was performed by generating histograms of all cell values from fluorescence intensity images of positive cells identified by FLIM images. Each histogram was fitted to 1 and 2 component Gaussian curves. The lowest Akaike information criterion (AIC) signified the best fitting probability density function for the histogram. Probability density functions were normalized to have an area under the curve equal to 1. The OSI was calculated as the ratio of the mean intensity of cellular ROS to the mean intensity of cellular GSH.

4.4.6 Tissue collection and plasma biochemical measurements

Mouse blood (0.2 mL) was collected in lithium heparin tubes from the inferior vena cava using a 30 gauge needle. At the end of the experiment, the liver, kidney and spleen were excised, and portions were immersed into 10% buffered formalin for histological assessment. Plasma concentration of alanine aminotransferase (ALT) was measured using a Hitachi 747 analyzer (Hitachi Ltd., Tokyo, Japan).

4.4.7 Histology

Organ specimens were fixed in 4% buffered formalin and embedded in paraffin. Sections were obtained for Hematoxylin & Eosin (H&E) stain to evaluate histopathologic features. The OlyVIA software 2.6 (Olympus, Münster, Germany) was used to visualise

and scan the slides. Bromobimane was used for labelling GSH in liver sections on slides according to the manufacturer instructions.

4.4.8 Statistical tests

Student's t test with a Bonferroni correction was used to compare the data between groups. All the statistical analysis was done using GraphPad Prism v 6.04 (GraphPad Software Inc., La Jolla, California). Results were considered statistically significant with a *p*-value < 0.05.

4.5 Results

4.5.1 Sensing mechanism of the two-photon dual imaging probes

This two-photon sensing platform consists of three probes (**Fig. 4.1A**), which combine a tris(2,2'-bipyridine)Ru(II) complex as the turn-on fluorescent unit, with the specific responsive group for GSH, H_2O_2 or HOCl, which also serves as an electron acceptor. Excitation of the tris(2,2'-bipyridine)Ru(II) complex leads to the triplet state of metal-to-ligand charge transfer (3MLCT), and by this process, the metal electrons are transferred to the bipyridine ligands in an emissive state. As shown in **Fig. 4.1B**, when this ligand is conjugated to a strong electron acceptor, such as phenyl-2,4dinitrobenzenesulfonate in the P-GSH, the electron transfer destination will be diverted from 2,2'-bipyridine to phenyl-DNBSO. Thus, the 3MLCT is corrupted and the fluorescence and lifetime of the Ru(II) complex are quenched by an intramolecular photo-induced electron transfer process (PET). While the reaction with GSH, H_2O_2 or HOCl can specifically trigger the quantitative cleavage of the electron acceptor group, and the PET process is eliminated, then the fluorescence of the ruthenium complex can be turned on.

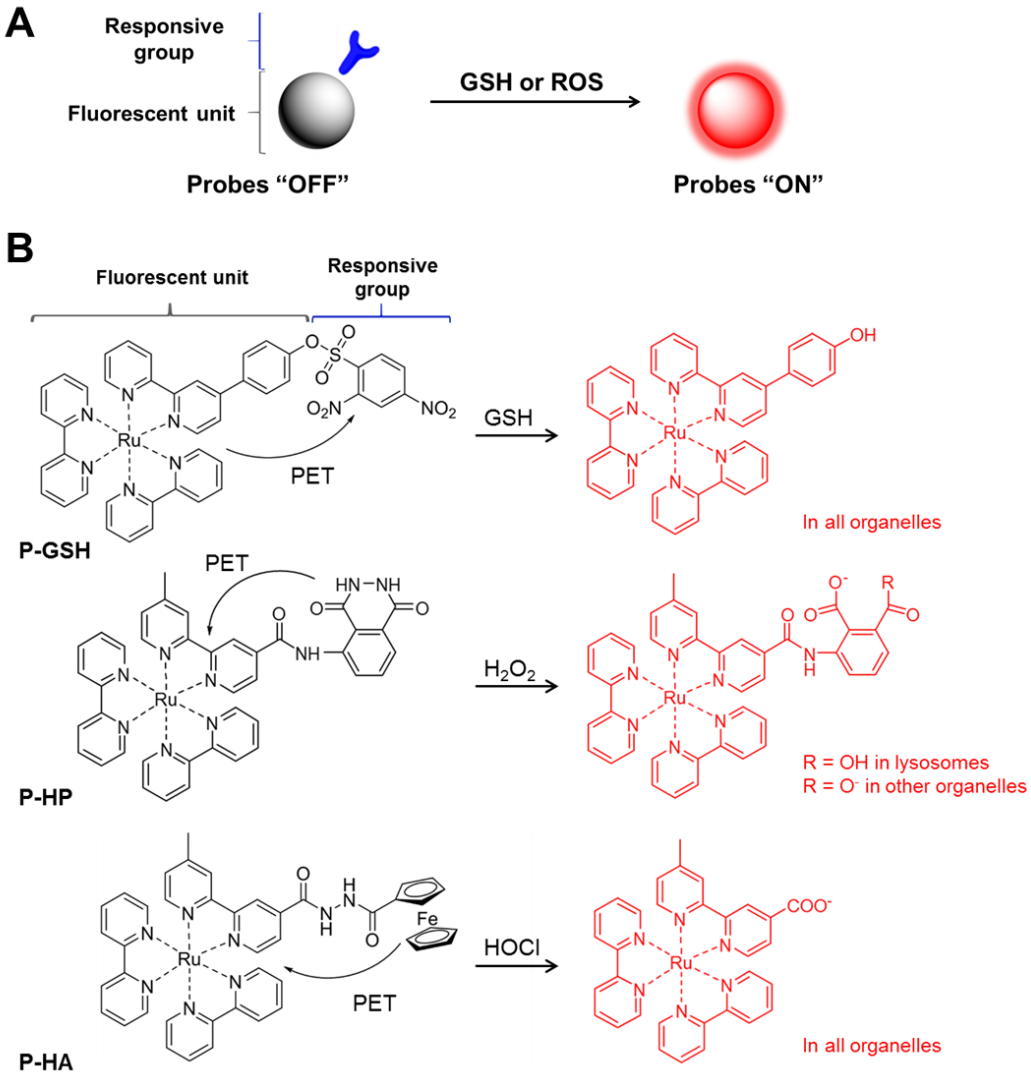

Figure 4.1 Design of two-photon sensing platform for imaging of oxidative stress. (A) Illustration of the sensing mechanism. This sensing platform consists of two parts: a ruthenium complex as the turn-on fluorescent unit, and a responsive group as the GSH, H_2O_2 or HOCl reaction moiety. (B) Response reaction of P-GSH, P-HP and P-HA toward GSH, H_2O_2 or HOCl, respectively. The probes are non-fluorescent due to the effective photo-induced electron transfer process (PET). In the presence of GSH, H_2O_2 or HOCl, the responsive group can be quantitatively cleaved, and the reaction ruthenium complex will become highly fluorescent. The protonation state of P-HP depends on the organelle pH values. The counter-ions are sodium and potassium in biological conditions.

4.5.2 *In vitro* characterization of the two-photon dual imaging probes

We have previously reported that the ruthenium complex has a broad single-photon absorption spectrum from 350 to 550 nm [15-18]. For *in vivo* application of deep-tissue imaging, we first evaluated the two-photon absorption spectrum of these two-photon dual

imaging probes. **Fig. 4.2A** shows the two-photon absorption spectrum of P-GSH with a peak at 850 nm, and its emission spectrum with a peak at 612 nm. To determine the fluorescence intensity of P-GSH in response to GSH, we added GSH in a stepwise manner and measured the fluorescence signal in an emission channel of 515-620 nm at a two-photon excitation wavelength of 850 nm. The dose-dependent intensity enhancement of P-GSH showed good linear relationships in the concentration range from 0 to 10 μM of GSH, and the maximum intensity was at the concentration of 20 μM (**Fig. 4.2B**). The P-HP and P-HA have similar excitation and emission spectra to that of P-GSH (**Supplementary Fig. 4.1A** and **B**). Good linear correlations can be obtained in the concentration range from 0 to 50 μM of H_2O_2 and 0 to 40 μM of HOCl (**Supplementary Fig. 4.1C** and **D**). Because of the differences in specific responsive groups and PET process, the P-GSH, P-HP and P-HA have different sensitivity for detection of GSH, H_2O_2 and HOCl. Metal complex-based probes have been reported to be particularly suitable for FLIM imaging because their fluorescence lifetime (typically more than 50 ns) is much longer than those of tissue (2-3 ns) and most organic dyes (1-5 ns) [24]. So we further measured the fluorescence lifetime of P-GSH in PBS. The P-GSH has a characteristic 38-fold increase of emission lifetime from 6 to 225 ns in the presence of GSH (Fig. 2C and D). P-HP and P-HA also have over 20-fold increase of emission lifetime from 5.5 and 4.3 ns to 146 and 90.5 ns, respectively. The optical characteristics of P-GSH, P-HP and P-HA are summarised in **Supplementary Table 4.1**.

We have previously reported the specificity and *in vitro* cellular uptake properties of these probes [15-18]. To further examine their applicability for detecting cellular GSH and ROS levels using FLIM, probes (30 μM) were incubated with a mouse hepatocyte cell line (AML12) in culture media for 2 h. **Fig. 4.2E** displays the spatial distribution of the fluorescence lifetime signal of P-GSH in the AML12 cells in two emission channels. According to our previous work, long-lifetime fluorescent probes can be differentiated *in vivo* using the slow decay lifetime τ_2, rather than the fast decay lifetime τ_1. Thus, in this study, the pseudo-color was based on the slow decay lifetime (τ_2) of individual pixel. In the 350-450 nm spectral channel (left), the fluorescence signal mainly comes from nicotinamide adenine dinucleotide phosphate (NAD(P)H), which is a major endogenous fluorophore in cells. The spectral channel of 515-620 nm (right) captured the fluorescence signal of P-GSH, as well as aufluorescence signal from flavin adenine dinucleotide (FAD) in cells. Characteristic longer slow decay lifetimes (> 100 ns) could be detected within the cells after P-GSH administration in the 515-620 nm spectral channel. While no such long lifetime was observed after cells incubated with a thiol scavenger, N-ethylmaleimide

(NEM), to remove the endogenous GSH. Because reacted probe has much longer lifetime compared to unreacted probe and FAD, we believe the significant increase of τ_2 with the cells after probe administration is due to the reaction of probe and their specific substrate. These results confirm that the cellular lifetime change is attributed to the reaction of P-GSH with endogenous intracellular GSH.

To investigate the photostability of P-GSH, P-HP and P-HA for *in vivo* imaging, we next incubated probes in PBS under irradiation with a deuterium lamp at room temperature, whilst fluorescence intensity and fluorescence lifetime was assessed over time (**Supplementary Fig. 4.2**). There was no significant change in the fluorescence intensity (Supplementary Fig. 2) or fluorescence lifetime during the 2 hour irradiation. Thus, our dual imaging probes exhibit characteristic long emission lifetime with two-photon excitation and high photostability required for detecting GSH or ROS levels in pathophysiological conditions *in vivo*.

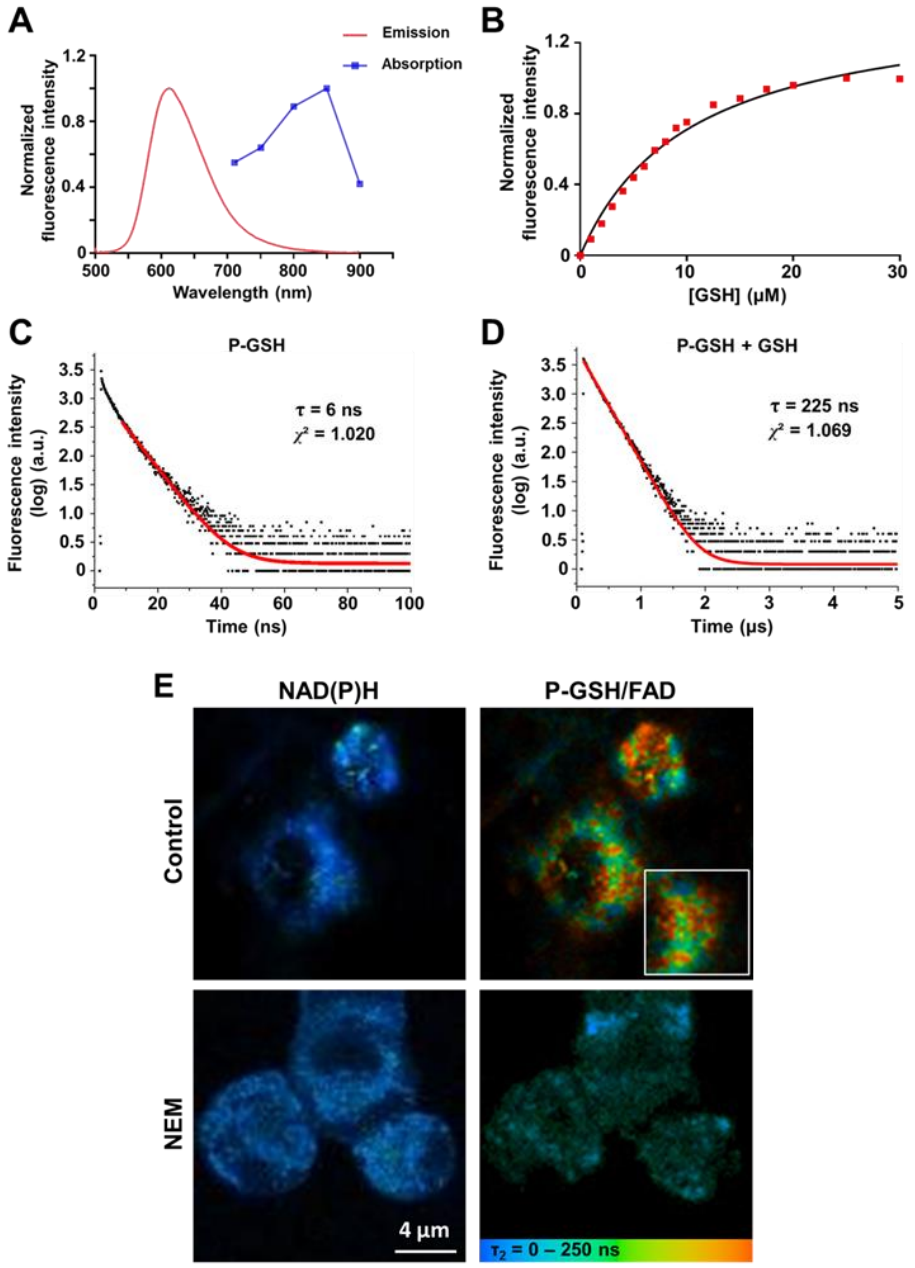

Figure 4.2 Spectral characterization of P-GSH *in vitro*. (A) Two-photon absorption and emission spectra of P-GSH reacted with 10 μM of GSH in PBS buffer. (B) Fluorescence response of P-GSH (10 μM) to varying concentrations of GSH. (C) Emission decay of P-GSH in PBS buffer. (D) Emission decay of P-GSH in PBS buffer with GSH (20 μM). (E) FLIM images of representative P-GSH loaded AML12 cells with (lower row) or without (upper row) NEM treatment. The autofluorescence of NAD(P)H was collected at $\lambda_{Exc}/\lambda_{Em}$: 740/350 to 450 nm. The fluorescence signal for probes and FAD was collected at $\lambda_{Exc}/\lambda_{Em}$: 850/515 to 620 nm. Values are the mean for n = 5 replicates.

4.5.3 Imaging of cellular oxidative stress in APAP-induced liver injury

The mechanism of APAP-induced liver injury is well established. An overdose of APAP can lead to oxidative stress through the overproduction of ROS (mainly H_2O_2). This results in the consumption of key cellular antioxidants, such as GSH, initiating a signaling cascade that results in necrotic cell death. GSH and the GSH precursor N-acetylcysteine (NAC) can scavenge the reactive metabolites, and have been used to treat patients with APAP overdose [25, 26]. Thus APAP-induced liver injury serves as an ideal model of investigating the potential of cellular oxidative stress for early prediction of treatment response in a clinically relevant model.

We anesthetized the mice and exposed the liver at 60 min after APAP administration. Fluorescence intensity imaging and FLIM were acquired at 15 min after injection of 50 μM of P-GSH or P-HP into the portal vein (**Supplementary Fig. 4.3**). As shown in **Fig. 3A**, signals induced by the probes response to GSH in cells were clearly observed using both fluorescence intensity imaging and FLIM methods. A significant increase in P-GSH fluorescence was observed in some hepatocytes (circled in white). Further analysis of FLIM data reveals a significant increase (> 100 ns) in the slow decay lifetime of this area after injection of P-GSH, which reacting with GSH is responsible for the change of lifetime (**Fig. 3B** and **C**). Some false-positive hepatocytes determined by fluorescence intensity imaging (circled in yellow in **Fig. 4.3A**) were found with shorter fluorescence lifetime using FLIM, which removes all the possibilities of crosstalk from in vivo environmental or instrumental factors. There was no significant decrease of probe signals up to 2 hours after injection. We compared P-GSH to bromobimane, a fluorescent heterocyclic compound commonly used for GSH sensing [27, 28]. The fluorescence signal produced by bromobimane cannot be differentiated from the liver autofluorescence *in vivo* after intraportal injection. Comparable fluorescence intensity imaging of GSH can only be obtained from liver sections treated with bromobimane (**Supplementary Fig. 4.4**). The percentage of GSH-positive hepatocytes has no significant difference between this detection method and FLIM ($p > 0.05$). Thus these *ex vivo* imaging results using bromobimane confirmed the *in vivo* results using P-GSH. While the photochemical characteristics of bromobimane based imaging restrict its utility to *ex vivo* tissue in contrast to in vivo P-GSH imaging of the GSH generation in the liver injury.

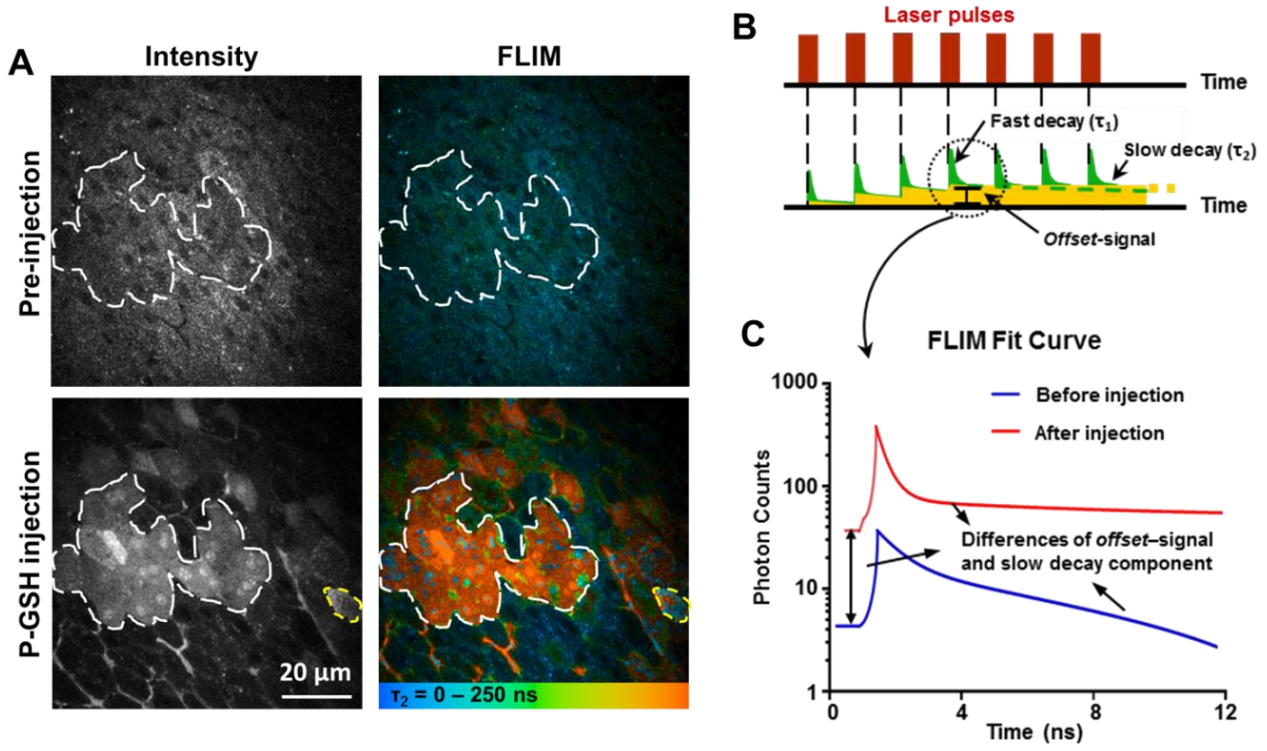

Figure 4.3 Dual-mode *in vivo* imaging of GSH in hepatocytes of mice after APAP administration. (A) Representative fluorescence intensity and FLIM images of mouse liver before and 15 min after probes injection. All images were recorded at $\lambda_{Exc}/\lambda_{Em}$: 850/515 to 620 nm. Scale bar: 20 µm. **(B)** Sketch to illustrate the parameters of the fit procedure of the fluorescence decay curve. Two lifetimes, τ_1 and τ_2 represent the fast and slow decay lifetimes. The slow decaying fluorescence accumulates on repeated laser pulsing to create enhanced background signal, defined as '*offset*'. **(C)** Fluorescence decay fit curves of representative area (circled in white) before (Blue) and after (Red) P-GSH injection.

Having quantified the cellular oxidative stress response following APAP-induced liver injury, we next evaluated the therapeutic context. As shown in **Supplementary Fig. 4.5**, zonal GSH changes in the liver during NAC treatment were identified in fluorescence intensity images and FLIM at low magnification. Representative dual-mode images of GSH and H_2O_2 at high magnification (**Fig. 4.4A** and **B**) demonstrate the high-resolution capability of this technique, which allows single-cell analysis (**Supplementary Fig. 4.6**) and population modeling for quantification of cellular subpopulations with varying oxidative stress. Calculated from FLIM images, we found that NAC treatment significantly increased the percentage of GSH-positive hepatocytes, and decreased that of H_2O_2-positive hepatocytes, compared with the untreated ($p < 0.05$, **Fig. 4.4C** and **E**). Population density modeling of cellular distributions of the GSH intensity calculated from fluorescence intensity images revealed two populations of GSH-positive hepatocytes at 75 min after

APAP administration, both lower than the mean intensity of the controls (**Fig. 4.4D**). The NAC treated group has a single population with higher fluorescence intensity maxima at 30 min after NAC administration. This heterogeneity of cellular GSH level was not seen after NAC treatment, suggesting that the APAP sensitive cell subpopulation responses to NAC treatment. The comparison of H_2O_2 intensity determined on a per cell basis showed similar distributions between groups as to GSH intensity (**Fig. 4.4F**).

A composite endpoint, the optical oxidative stress index (OSI), was computed as the ratio of the mean intensity of cellular ROS to the mean intensity of cellular GSH [29]. After 30 min of NAC treatment, the optical OSI was significantly reduced compared with the untreated ($p < 0.05$, **Fig. 4.5A**). By 2 hours, the optical OSI further decreased in the treatment group ($p < 0.05$). The imaging results were compared with conventional biochemical and histological assessment. As shown in **Fig. 4.5B**, a significant reduction in plasma alanine aminotransferase (ALT) levels associated with NAC treatment was first detected 3 hours after therapy. Furthermore, an increase beyond control levels was not detected until 2 hour after delivery of APAP. Histological changes were not apparent 30 min after NAC treatment (**Fig. 4.5C**). Remediation of APAP-induced hepatocellular necrosis was observed in hematoxylin and eosin (H&E) stained sections of liver tissue 3 hours after NAC treatment. The optical OSI changes therefore precede the conventional measures such as plasma liver enzyme levels or histological features of liver injury. In addition, no obvious necrosis and abnormity were observed in the sections of liver, kidney and spleen tissue from the control group (**Supplementary Fig. 4.7**), suggesting that the two-photon dual imaging probes have no distinct toxicity. Altogether, these results confirm the utility of this sensing platform for monitoring cellular oxidative stress to predict drug response to APAP-induced liver injury *in vivo*.

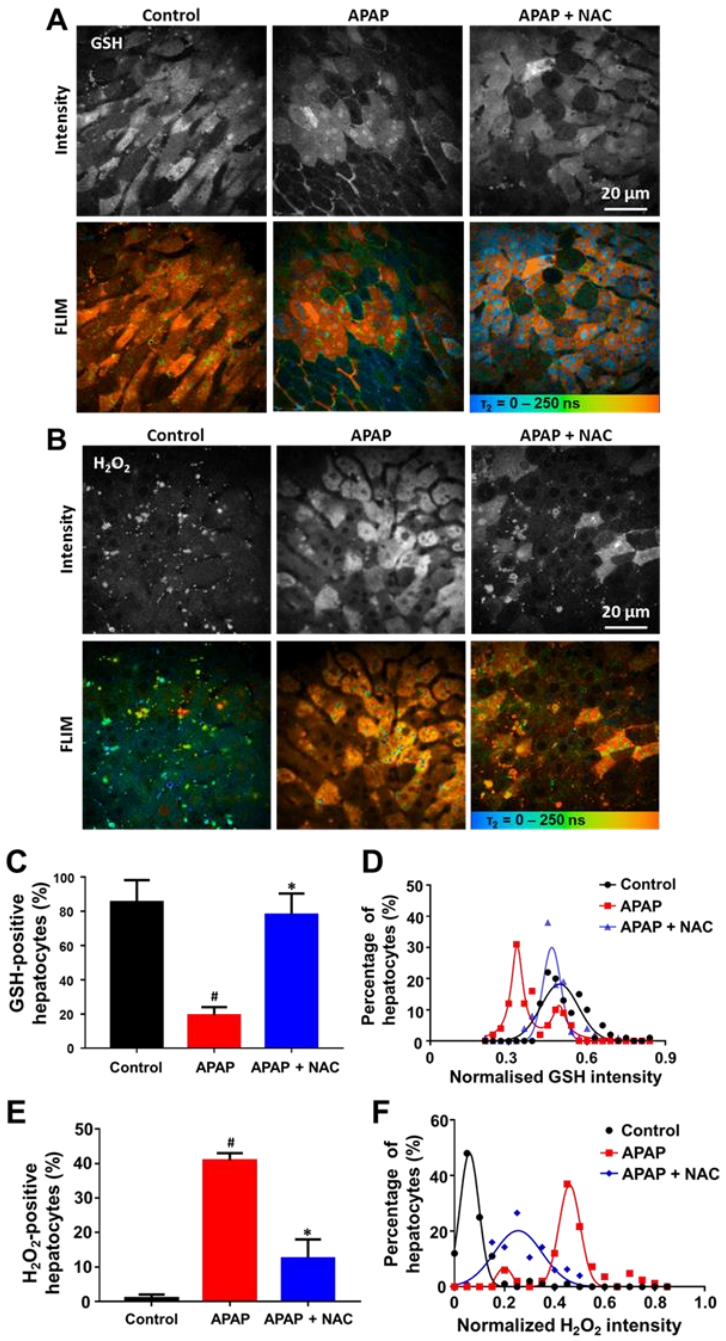

Figure 4.4 Dual-mode quantitative imaging of the change of oxidative stress in hepatocytes responses to NAC treatment against APAP induced liver injury. (A and B) Representative fluorescence intensity and FLIM images of cellular GSH or H_2O_2 of the control, APAP, APAP + NAC groups at 30 min after NAC treatment (75 min after APAP administration). All images were recorded at $\lambda_{Exc}/\lambda_{Em}$: 850/515 to 620 nm. Scale bar: 20 μm. (C and E) The percentages of GSH or H_2O_2-positive hepatocytes of the control, APAP, APAP + NAC groups. (D and F) Population density modeling of the mean GSH or H_2O_2 intensity per cell in control APAP, APAP + NAC groups. Values are the mean ± s.d. for n = 5 mice; * $p < 0.05$, compared with APAP groups; # $p < 0.05$, compared with control group.

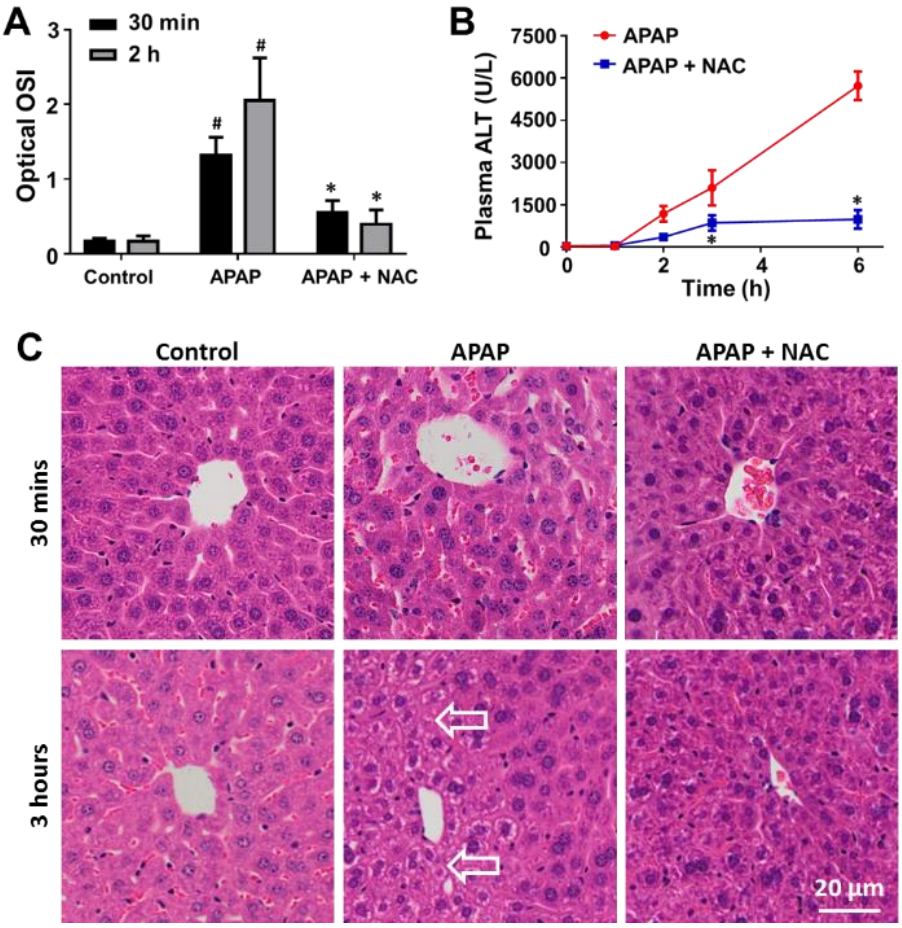

Figure 4.5 Optical oxidative stress index (OSI) of the liver detects response to NAC treatment against APAP induced liver injury. (A) Optical OSI of the liver at 30 min and 2 hours after NAC treatment (75 and 165 min after APAP administration). (B) Concentration-time profile of ALT levels in peripheral blood of the APAP and APAP + NAC groups. (C) Representative histology (H&E staining) of the liver of the control, APAP, APAP + NAC groups at 30 min and 3 hours after NAC treatment (75 and 225 min after APAP administration). Arrows indicate cellular necrosis. Values are the mean ± s.d. for n = 5 mice; * $p < 0.05$, compared with untreated groups; # $p < 0.05$, compared with control group.

4.5.4 Imaging of cellular oxidative stress in hepatic ischemia-reperfusion injury

It is well documented that during hepatic I/R injury, ROS (mainly HOCl) are generated by neutrophils and diffuse into hepatocytes, causing oxidant stress-mediated injury [30]. This pathway can be inhibited by administration of GSH or NAC [31]. Therefore, we used a mouse hepatic I/R injury as an independent model to test the potential of evaluating cellular oxidative stress for early prediction of treatment response. At 30 min after

reperfusion, we observed reductions in the percentage of HOCl-positive hepatocytes and mean HOCl intensity in both GSH and NAC treated groups using P-HA (**Fig. 4.6A**, **B** and **C**), indicating successful remediation of cellular ROS. There were differences in treatment response between GSH and NAC. Consistent with reports that GSH is inferior to NAC as an antidote to hepatic I/R injury [31], GSH treatment resulted in production of higher HOCl level compared to the NAC treated group though still lower than the untreated group ($p < 0.05$, **Fig. 4.6B** and **C**). Additionally, GSH and NAC increased cellular GSH to the same extent (**Supplementary Fig. 4.8**).

The optical OSI significantly decreased in both GSH and NAC treated groups compared with the untreated group from 30 min after reperfusion ($p < 0.05$, **Fig. 4.6D**). The difference in optical OSI between GSH and NAC treated groups was observed at 2 hours after reperfusion ($p < 0.05$). However, no difference in ALT levels in peripheral blood was detected between the treatment groups within 4 hours after reperfusion (**Fig. 4.6E**). As shown in **Fig. 4.6F**, the drug response predicted by dual-mode quantitative imaging was consistent with reduced hepatocyte necrosis observed in H&E stained sections of liver tissue. The optical OSI changes therefore precede the conventional measures such as plasma liver enzyme levels or histological features of hepatic I/R injury. These results fully characterize optical OSI and show its potential for monitoring early-drug response *in vivo* at the single-cell level.

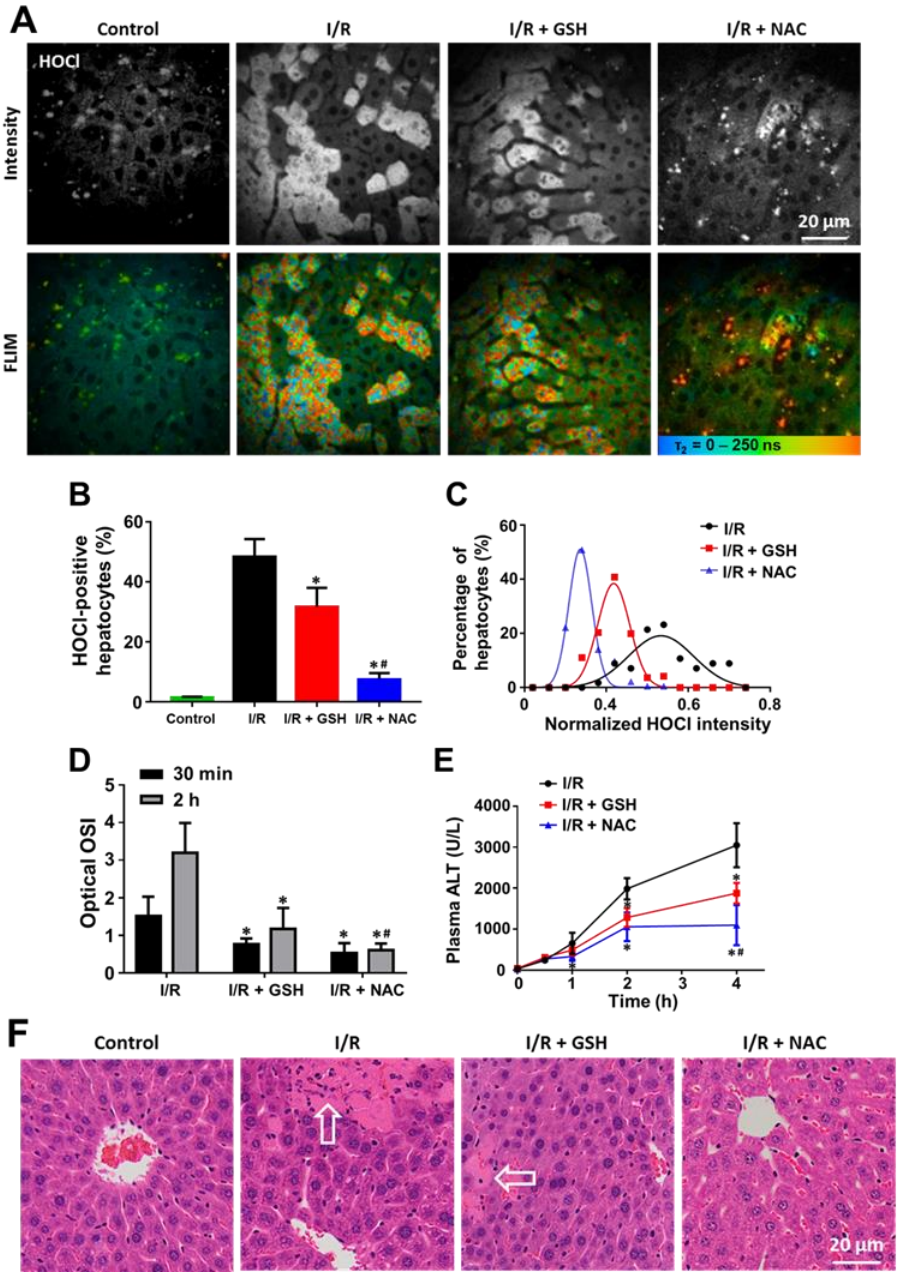

Figure 4.6 Quantitative *in vivo* detection of different responses to GSH and NAC treatment against hepatic I/R injury. (A) Representative fluorescence intensity and FLIM images of cellular HOCl of the control, I/R, I/R + GSH, and I/R + NAC groups at 30 min after reperfusion. All images were recorded at $\lambda_{Exc}/\lambda_{Em}$: 850/515 to 620 nm. Scale bar: 20 μm. (B) The percentages of HOCl-positive hepatocytes in all groups. (C) Population density modeling of the mean HOCl intensity per cell in the I/R, I/R + GSH, and I/R + NAC groups. (D) Optical OSI of the liver at 30 min and 2 hours after reperfusion. (E) Concentration-time profile of ALT levels in peripheral blood of the I/R, I/R + GSH, and I/R + NAC groups. (F) Representative histology (H&E staining) of the liver of all groups at 4 hours after reperfusion. Arrows indicate cellular necrosis. Values are the mean ± s.d. for n = 5 mice; * $p < 0.05$, compared with untreated groups; # $p < 0.05$, compared with I/R + GSH group.

4.6 Discussion

Oxidative stress contributes to a diverse array of physiological and pathological events in living organisms, but there is an insufficient understanding of how its cellular fluxes initiate signaling cascades in living animals in stages of health, aging, and disease [32]. Whereas a growing number of chemical tools have been developed to probe redox biology, technologies that can monitor fluctuations in cellular redox environment in living animals remain limited. We showed that our transition-metal complex-based sensing platform is capable of simultaneous two-photon fluorescence intensity imaging and FLIM, enabling accurate *in vivo* detection of ROS and GSH at the single cell-level resolution. Moreover, the imaging results correlate well with conventional markers of liver injury such as liver enzyme levels and histology, which validate the optical OSI as a prodromal imaging biomarker for prediction and evaluation of drug efficacy.

Although molecular probes have been widely used in biomedical imaging, most of these studies exclusively involve steady-state emission where changes in intensity or emission energy of the probes are used as the imaging signal [24]. Metal complex-based probes are particularly suitable for lifetime-based imaging, as they emit from long-lived, triplet-based excited states that are usually efficiently populated through the heavy-atom effect. For example, many metal complex-based probes can cross the membrane and accumulate in the mitochondria to detect metabolic status in mitochondria of cells. Ruthenium-based probes have been developed for lifetime-based imaging of the cellular DNA, RNA and oxygen levels [24, 33]. Furthermore, metal complexes often possess high two-photon absorption cross-sections, making them particularly compatible with two-photon based lifetime microscopy techniques [34]. In particular, the π-conjugated ligands of our metal complex-based probes endow them with two-photon absorption property for *in vivo* deep-tissue imaging. Moreover, the rapid sensing kinetics and large dynamic range of sensitivity allow our metal complex-based probes to detect nanomolar to micromolar levels of ROS and GSH in near–real time. This permits sensitive monitoring of cellular oxidative stress levels as a mediator of liver injury. This sensing platform has advantages over small-molecule fluorescent-based probes for *in vivo* ROS or GSH imaging reported to date. Conventional emission-based detection methods are influenced by probe concentration and the biomolecular microenvironment [10, 35, 36], or have only been employed under one-photon model [9, 37]. We found metal complex-based probes can uniquely overcome current limitations to improve detection accuracy in quantitative visualization of oxidative stress by FLIM. In addition, since these probes do not have significant systemic toxicity in animals, they may also be applied to study the etiology and

pathophysiology of diseases involving oxidative stress. It is also worth mentioning that the chief limitation of these probes is their irreversibility. They cannot report on decreases of GSH, H_2O_2 and HOCl concentrations. Once all reacted, they will not report any more changes of the actual GSH, H_2O_2 and HOCl concentrations. Therefore, reversible probes such as conjugated polymer based phosphorescent nanoparticles will be highly needed in the future for *in vivo* quantitative measurement. Another limitation of this study is the short observation time window of FLIM (12.5 ns) in our multiphoton microscopy (LaVision and DermaInspect). Although we do have detected significant increases in the slow decay lifetime within the cells after probe administration, phosphorescence lifetime detection is a much better suitable technique to accurately determine the long fluorescence lifetime of the probes.

Current methods of evaluation of drug response are generally based on organ morphology, histological characteristics, and biomarkers in peripheral blood. Molecular changes induced by treatment precede changes in morphology or these biomarkers, and may provide proximal endpoints of drug response [38]. The optical OSI from dual-mode images using metal complex-based probes captures these drug-induced changes in GSH and ROS, which have been hypothesized to correlate closely with treatment outcomes [6, 39]. Our study introduce the concept of molecular imaging as a tool to study drug response *in vivo*, and is the first to correlate optical OSI with a standard assay of drug response in liver injury. The data presented here support the use of optical OSI as an effective imaging biomarker for evaluation of drug response, as cellular H_2O_2, HOCl and GSH levels change at an early stage after liver injury, and precede even histological signs of liver tissue and changes of liver enzymes in peripheral blood. Beyond the study of liver injury, optical OSI may also have utility predicting drug response in other systems. For example, in neurodegenerative diseases, ROS have been implicated as the initiators of protein misfolding and the downstream inducers of cell death [40]. ROS also have an important role in inflammatory diseases, acting as effectors and signaling molecules in both the innate and adaptive immune response [7]. ROS levels change rapidly during anti-cancer therapy. High levels of ROS generated by chemotherapeutic agents for liver cancer, such as doxorubicin, platinum drugs and 5-fluorouracil, can induce cancer cell death [41, 42]. Thus, detection of oxidative stress in real time and with high spatial and temporal resolution using metal complex-based probes may help uncover mechanisms of ROS production and action in a broad range of diseases and contribute to the development of new therapeutics.

High-resolution image analysis revealed initial heterogeneous GSH and ROS levels among hepatocytes after APAP-induced injury (**Fig. 4D** and **F**). The cellular details of the liver can be imaged deep to 250 μm below the fibrous capsule of Glisson using multiphoton microscopy. According to our previous study, imaging depth of 50 to 100 μm was the clearest for observing cellular and subcellular morphology in the liver. Hepatocytes around the central vein (Zone 3) are more sensitive to APAP-induced injury than those around the portal vein (Zone 1) [43]. Consistent with this, our data suggest that there exist two intrinsic subpopulations of hepatocytes with differential tolerance to APAP toxicity. This heterogeneity of cellular GSH and ROS levels was not seen after NAC treatment, suggesting that NAC is protective to this APAP sensitive subpopulation. The ability to detect disease severity at a cellular level before treatment may provide leads for identification of drugs that target such susceptible subpopulations before they are selected by the primary therapy.

In conclusion, in this proof-of-concept study using a two-photon sensing platform, we present the first dual-mode quantitative imaging of cellular oxidative stress *in vivo*. The high resolution and high accuracy of imaging allows subpopulation analysis for identification of heterogeneous disease severity among cell populations and assessment of drug response. We demonstrate that optical OSI can be used as an early and sensitive indicator of metabolic response to treatment in two distinct models of liver injury. Altogether, these results suggest that two-photon dual imaging probes are a powerful tool to monitor the production and action of cellular oxidative stress in a broad range of diseases and inform the rational modification of treatment decisions accordingly.

References

[1] Czaja MJ. Cell signaling in oxidative stress-induced liver injury. Seminars in liver disease. 2007;27:378-89.

[2] Shuhendler AJ, Pu K, Cui L, Uetrecht JP, Rao J. Real-time imaging of oxidative and nitrosative stress in the liver of live animals for drug-toxicity testing. Nature biotechnology. 2014;32:373-80.

[3] Hecht F, Pessoa CF, Gentile LB, Rosenthal D, Carvalho DP, Fortunato RS. The role of oxidative stress on breast cancer development and therapy. Tumour biology : the journal of the International Society for Oncodevelopmental Biology and Medicine. 2016;37:4281-91.

[4] Naito Y, Takano H, Yoshikawa T. Oxidative stress-related molecules as a therapeutic target for inflammatory and allergic diseases. Current drug targets Inflammation and allergy. 2005;4:511-5.
[5] Valko M, Leibfritz D, Moncol J, Cronin MT, Mazur M, Telser J. Free radicals and antioxidants in normal physiological functions and human disease. The international journal of biochemistry & cell biology. 2007;39:44-84.
[6] Tong L, Chuang CC, Wu S, Zuo L. Reactive oxygen species in redox cancer therapy. Cancer letters. 2015;367:18-25.
[7] Nathan C, Cunningham-Bussel A. Beyond oxidative stress: an immunologist's guide to reactive oxygen species. Nature reviews Immunology. 2013;13:349-61.
[8] Bernal W, Wendon J. Acute liver failure. The New England journal of medicine. 2013;369:2525-34.
[9] Zhang R, Zhao J, Han G, Liu Z, Liu C, Zhang C, et al. Real-Time Discrimination and Versatile Profiling of Spontaneous Reactive Oxygen Species in Living Organisms with a Single Fluorescent Probe. Journal of the American Chemical Society. 2016;138:3769-78.
[10] Gomes A, Fernandes E, Lima JLFC. Fluorescence probes used for detection of reactive oxygen species. J Biochem Bioph Meth. 2005;65:45-80.
[11] Yin J, Kwon Y, Kim D, Lee D, Kim G, Hu Y, et al. Cyanine-Based Fluorescent Probe for Highly Selective Detection of Glutathione in Cell Cultures and Live Mouse Tissues. Journal of the American Chemical Society. 2014;136:5351-8.
[12] Jiang XQ, Yu Y, Chen JW, Zhao MK, Chen H, Song XZ, et al. Quantitative Imaging of Glutathione in Live Cells Using a Reversible Reaction-Based Ratiometric Fluorescent Probe. Acs Chem Biol. 2015;10:864-74.
[13] van der Heijden J, Bosman ES, Reynolds LA, Finlay BB. Direct measurement of oxidative and nitrosative stress dynamics in Salmonella inside macrophages. Proc Natl Acad Sci U S A. 2015;112:560-5.
[14] Kuimova MK, Yahioglu G, Levitt JA, Suhling K. Molecular rotor measures viscosity of live cells via fluorescence lifetime imaging. Journal of the American Chemical Society. 2008;130:6672-+.
[15] Zhang R, Song B, Dai ZC, Ye ZQ, Xiao YN, Liu Y, et al. Highly sensitive and selective phosphorescent chemosensors for hypochlorous acid based on ruthenium(II) complexes. Biosensors & bioelectronics. 2013;50:1-7.
[16] Zhang WZ, Zhang R, Zhang JM, Ye ZQ, Jin DY, Yuan JL. Photoluminescent and electrochemiluminescent dual-signaling probe for bio-thiols based on a ruthenium(II) complex. Anal Chim Acta. 2012;740:80-7.

[17] Dai ZC, Tian L, Xiao YN, Ye ZQ, Zhang R, Yuan JL. A cell-membrane-permeable europium complex as an efficient luminescent probe for singlet oxygen. J Mater Chem B. 2013;1:924-7.
[18] Cao L, Zhang R, Zhang W, Du Z, Liu C, Ye Z, et al. A ruthenium(II) complex-based lysosome-targetable multisignal chemosensor for in vivo detection of hypochlorous acid. Biomaterials. 2015;68:21-31.
[19] Hinson JA, Roberts DW, James LP. Mechanisms of acetaminophen-induced liver necrosis. Handbook of experimental pharmacology. 2010:369-405.
[20] Zhai Y, Petrowsky H, Hong JC, Busuttil RW, Kupiec-Weglinski JW. Ischaemia-reperfusion injury in liver transplantation--from bench to bedside. Nature reviews Gastroenterology & hepatology. 2013;10:79-89.
[21] Wang C, Chen K, Xia Y, Dai W, Wang F, Shen M, et al. N-acetylcysteine attenuates ischemia-reperfusion-induced apoptosis and autophagy in mouse liver via regulation of the ROS/JNK/Bcl-2 pathway. PloS one. 2014;9:e108855.
[22] Wang H, Liang X, Mohammed YH, Thomas JA, Bridle KR, Thorling CA, et al. Real-time histology in liver disease using multiphoton microscopy with fluorescence lifetime imaging. Biomed Opt Express. 2015;6:780-92.
[23] Liang X, Grice JE, Zhu Y, Liu D, Sanchez WY, Li Z, et al. Intravital multiphoton imaging of the selective uptake of water-dispersible quantum dots into sinusoidal liver cells. Small. 2015;11:1711-20.
[24] Baggaley E, Gill MR, Green NH, Turton D, Sazanovich IV, Botchway SW, et al. Dinuclear Ruthenium(II) Complexes as Two- Photon, Time- Resolved Emission Microscopy Probes for Cellular DNA. Angew Chem Int Edit. 2014;53:3367-71.
[25] Saito C, Zwingmann C, Jaeschke H. Novel Mechanisms of Protection Against Acetaminophen Hepatotoxicity in Mice by Glutathione and N-Acetylcysteine. Hepatology. 2010;51:246-54.
[26] Jaeschke H, Xie Y, McGill MR. Acetaminophen-induced Liver Injury: from Animal Models to Humans. Journal of clinical and translational hepatology. 2014;2:153-61.
[27] Danielsohn P, Nolte A. Bromobimanes--fluorescent labeling agents for histochemical detection of sulfur containing neuropeptides in semithin sections. Histochemistry. 1987;86:281-5.
[28] Chinn PC, Pigiet V, Fahey RC. Determination of Thiol Proteins Using Monobromobimane Labeling and High-Performance Liquid-Chromatographic Analysis - Application to Escherichia-Coli Thioredoxin. Anal Biochem. 1986;159:143-9.

[29] Motor S, Ozturk S, Ozcan O, Gurpinar AB, Can Y, Yuksel R, et al. Evaluation of total antioxidant status, total oxidant status and oxidative stress index in patients with alopecia areata. Int J Clin Exp Med. 2014;7:1089-93.
[30] Hasegawa T, Malle E, Farhood A, Jaeschke H. Generation of hypochlorite-modified proteins by neutrophils during ischemia-reperfusion injury in rat liver: attenuation by ischemic preconditioning. American journal of physiology Gastrointestinal and liver physiology. 2005;289:G760-7.
[31] Jaeschke H, Woolbright BL. Current strategies to minimize hepatic ischemia-reperfusion injury by targeting reactive oxygen species. Transplantation reviews. 2012;26:103-14.
[32] Van de Bittner GC, Dubikovskaya EA, Bertozzi CR, Chang CJ. In vivo imaging of hydrogen peroxide production in a murine tumor model with a chemoselective bioluminescent reporter. Proc Natl Acad Sci U S A. 2010;107:21316-21.
[33] Choi NW, Verbridge SS, Williams RM, Chen J, Kim JY, Schmehl R, et al. Phosphorescent nanoparticles for quantitative measurements of oxygen profiles in vitro and in vivo. Biomaterials. 2012;33:2710-22.
[34] Chen X, Sun LL, Chen Y, Cheng XL, Wu WJ, Ji LN, et al. A fast and selective two-photon phosphorescent probe for the imaging of nitric oxide in mitochondria. Biomaterials. 2015;58:72-81.
[35] Soh N. Recent advances in fluorescent probes for the detection of reactive oxygen species. Anal Bioanal Chem. 2006;386:532-43.
[36] Chen XQ, Wang F, Hyun JY, Wei TW, Qiang J, Ren XT, et al. Recent progress in the development of fluorescent, luminescent and colorimetric probes for detection of reactive oxygen and nitrogen species. Chem Soc Rev. 2016;45:2976-3016.
[37] Chang MCY, Pralle A, Isacoff EY, Chang CJ. A selective, cell-permeable optical probe for hydrogen peroxide in living cells. Journal of the American Chemical Society. 2004;126:15392-3.
[38] Ding Z, Zu S, Gu J. Evaluating the molecule-based prediction of clinical drug responses in cancer. Bioinformatics. 2016.
[39] Bergamini CM, Gambetti S, Dondi A, Cervellati C. Oxygen, reactive oxygen species and tissue damage. Current pharmaceutical design. 2004;10:1611-26.
[40] Jomova K, Vondrakova D, Lawson M, Valko M. Metals, oxidative stress and neurodegenerative disorders. Molecular and cellular biochemistry. 2010;345:91-104.

[41] Wang H, Li X, Chen T, Wang W, Liu Q, Li H, et al. Mechanisms of verapamil-enhanced chemosensitivity of gallbladder cancer cells to platinum drugs: glutathione reduction and MRP1 downregulation. Oncology reports. 2013;29:676-84.
[42] Li X, Wang H, Wang J, Chen Y, Yin X, Shi G, et al. Emodin enhances cisplatin-induced cytotoxicity in human bladder cancer cells through ROS elevation and MRP1 downregulation. BMC cancer. 2016;16:578.
[43] Lauterburg BH, Corcoran GB, Mitchell JR. Mechanism of action of N-acetylcysteine in the protection against the hepatotoxicity of acetaminophen in rats in vivo. The Journal of clinical investigation. 1983;71:980-91.

Supporting Information

Supplementary Figures

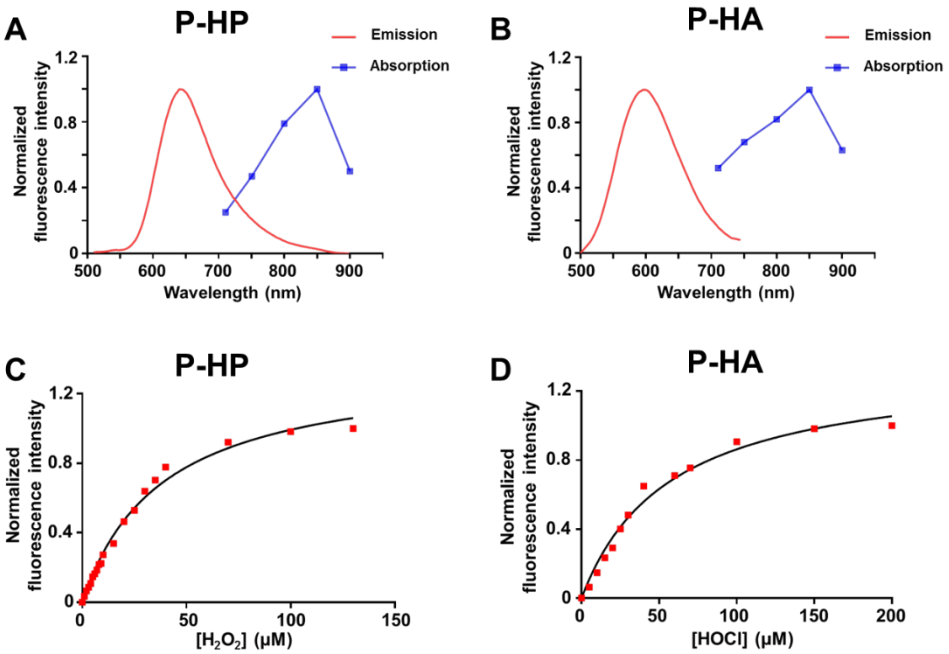

Fig. S4.1. Spectral characterization of P-HP and P-HA *in vitro*. (A, B) Two-photon absorption and emission spectra of P-HP and P-HA reacted with 50 μM of H_2O_2 and 40 μM of HOCl in PBS buffer, respectively. (C, D) Fluorescence response of P-HP and P-HA (10 μM) to varying concentrations of H_2O_2 and HOCl, respectively. Values are the mean for *n* = 5 replicates.

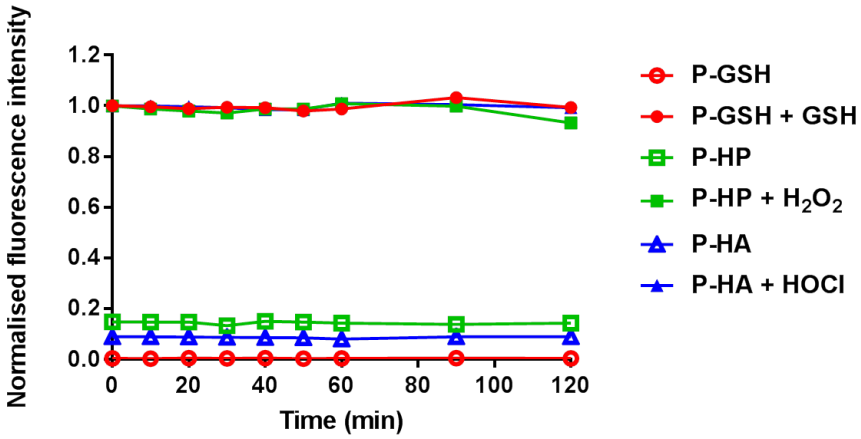

Fig. S4.2. Signal stability of P-GSH, P-HP and P-HA *in vitro*. Probes were incubated in PBS under the irradiation with a 30 W deuterium lamp at room temperature, and fluorescence was assessed over time. There was no significant change in the fluorescence intensity during the 4 hours of irradiation. Values are the mean for *n* = 5 replicates.

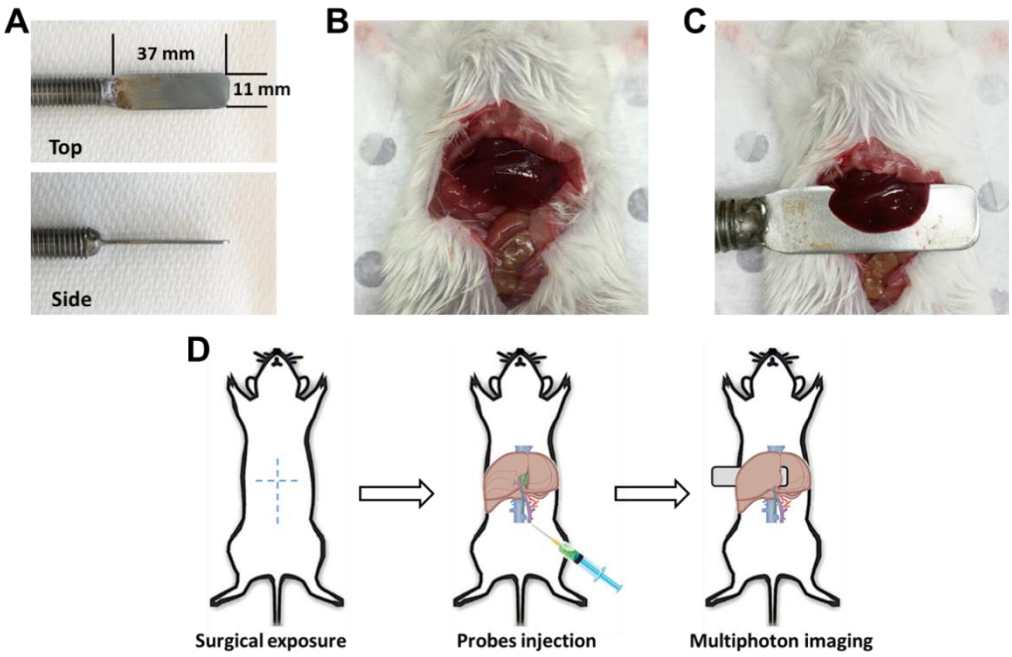

Fig. S4.3. *In vivo* imaging of cellular ROS and GSH in mouse liver. (a) Top and side views of the metal plate for imaging the liver using multiphoton microscopy. (b) A midline laparotomy is performed and the liver is exposed for imaging. (c) For *in vivo* imaging, the left lobe of the liver is placed on the metal plate, which attaches to an adjustable stand that could be elevated or lowered as required. (d) Schema for dual-mode imaging of cellular oxidative stress using metal complex-based probes.

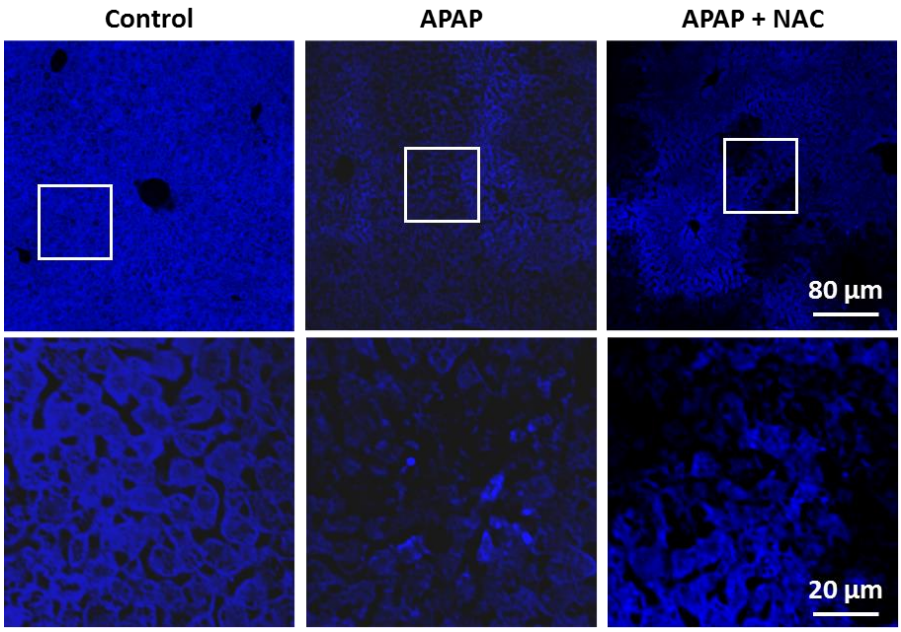

Fig. S4.4. Representative fluorescence intensity images of liver sections stained by Bromobimane (top), with corresponding image enlargements (bottom). The change of GSH intensity was observed after NAC treatment, correlating well with that in vivo detected using our metal complex-based probes.

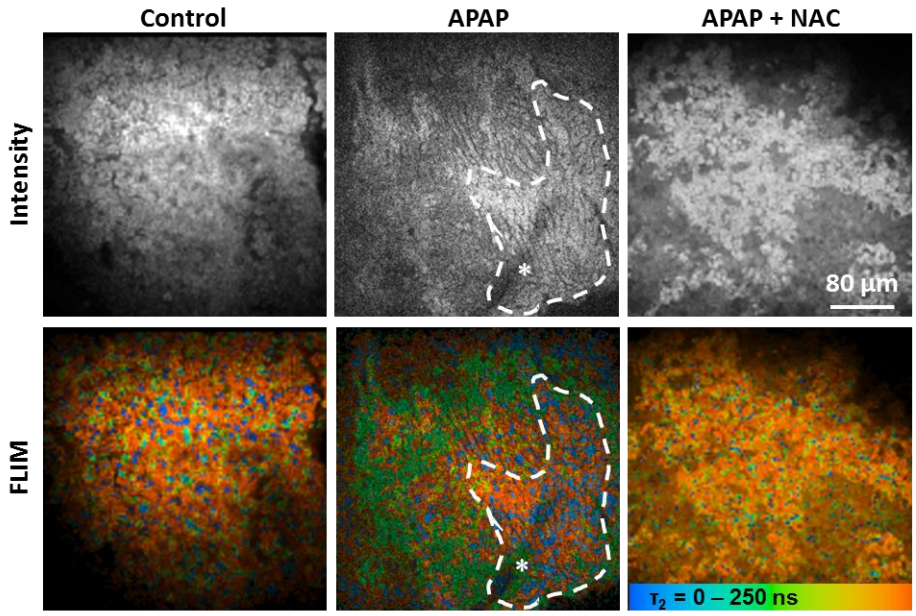

Fig. S4.5. Dual-mode quantitative imaging of the change of GSH in hepatocytes responses to NAC treatment against APAP induced liver injury at low magnification (10×). Hepatocytes around the portal vein (circled area) are less sensitive to APAP-induced GSH decrease. All images were recorded at $\lambda_{Exc}/\lambda_{Em}$: 850/515 to 620 nm. Asterisks indicate portal vein. Scale bar: 20 µm.

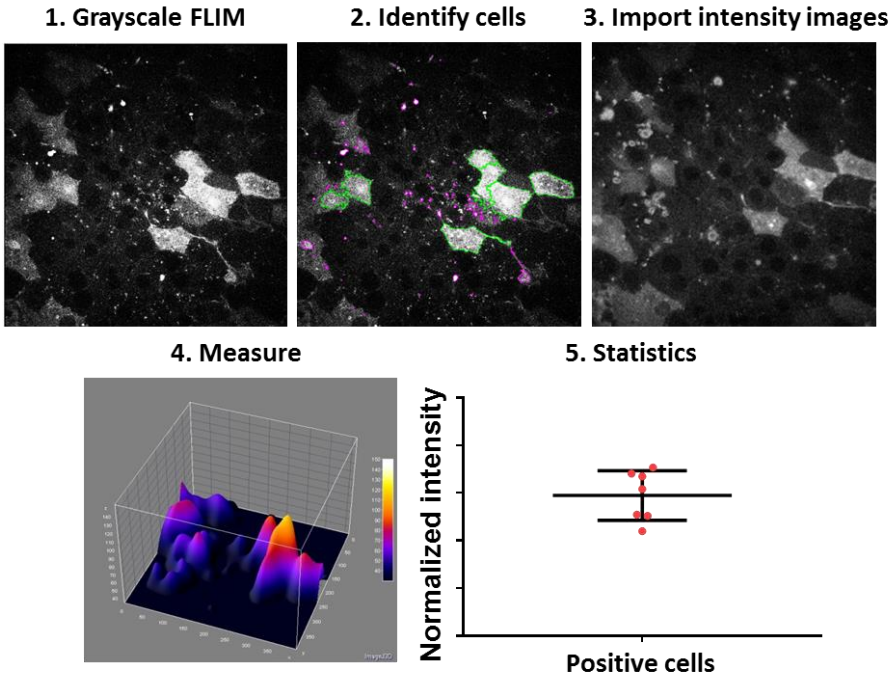

Fig. S4.6. Single-cell analysis of high-resolution fluorescence intensity images.

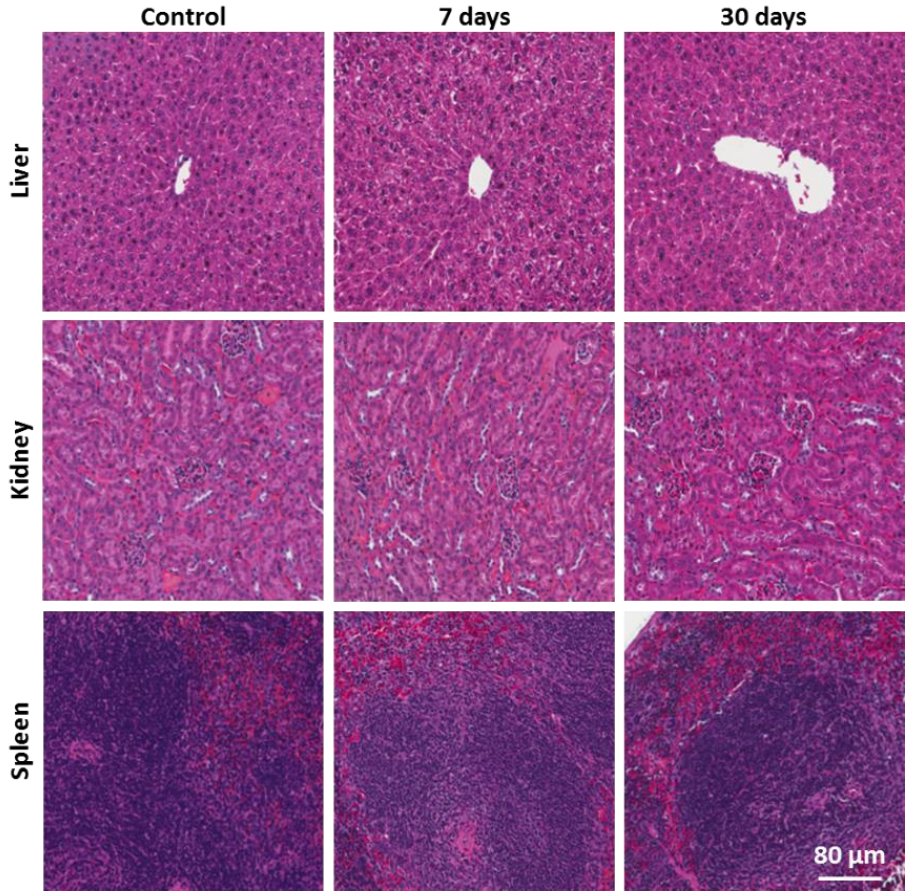

Fig. S4.7. Representative histology (H&E staining) of major organs of mice after injection of 50 μM of probes. No obvious necrosis and abnormity were observed in the sections of liver, kidney and spleen by histological examination. Scale bar: 80 μm.

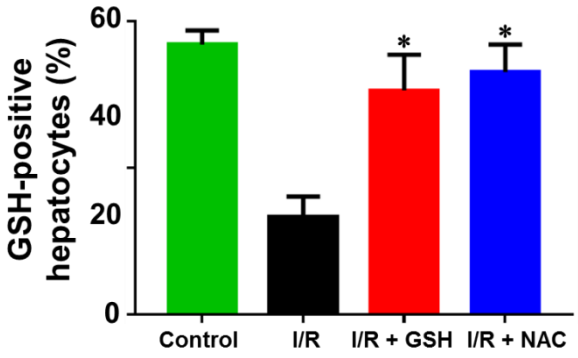

Fig. S4.8. The percentages of GSH-positive hepatocytes in all groups. Values are the mean ± s.d. for n = 5 mice; * p < 0.05, compared with untreated groups.

Supplementary Tables

Table S4.1. Optical characteristics of P-GSH, P-HP and P-HA

Probe	Two-photon absorption peak (nm)	Emission peak (nm)	fluorescence lifetime (ns)
P-GSH	850	612	225
P-HP	850	645	146
P-HA	850	600	90.5

Chapter 5

Visualisation and modelling of the in vivo fate of mesenchymal stem cells for the treatment of liver cirrhosis

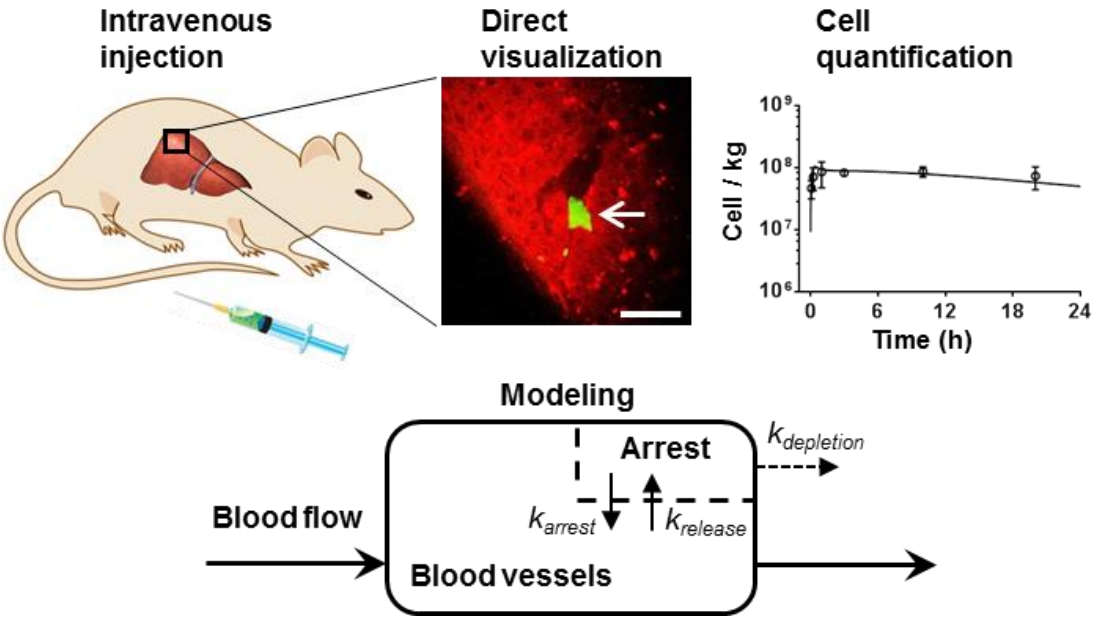

5.1 Synopsis

In this chapter, the spatiotemporal disposition of therapeutic mesenchymal stem cells was directly visualised using intravital multiphoton microscopy. A physiologically based kinetic model was then developed to elucidate the *in vivo* distribution of administered mesenchymal stem cells for the treatment of liver cirrhosis.

The article entitled, “A physiologically based kinetic model for elucidating the *in vivo* distribution of administered mesenchymal stem cells” has been published by *Scientific Reports*, 2016; 6: 22293. The manuscript, figures and tables have been adjusted to fit the overall style of the Thesis and incorporated as this chapter.

5.2 Abstract

Although mesenchymal stem cells (MSCs) present a promising tool in cell therapy for the treatment of various diseases, the *in vivo* distribution of administered MSCs has still been poorly understood, which hampers the precise prediction and evaluation of their therapeutic efficacy. Here, we developed the first model to characterise the physiological kinetics of administered MSCs based on direct visualization of cell spatiotemporal disposition by intravital microscopy and assessment of cell quantity using flow cytometry. This physiologically based kinetic model was validated with multiple external datasets, indicating potential inter-route and inter-species predictive capability. Our results suggest that the targeting efficiency of MSCs is determined by the lung retention and interaction between MSCs and target organs, including cell arrest, depletion and release. By adapting specific parameters, this model can be easily applied to abnormal conditions or other types of circulating cells for designing treatment protocols and guiding future experiments.

Key Words: Mesenchymal stem cells, Liver disease, Distribution, Modelling, Multiphoton microscopy

5.3 Introduction

Mesenchymal stem cells (MSCs), also called multipotent mesenchymal stromal cells, are self-renewing, nonhematopoietic somatic stem cells comparable to embryonic stem cells in terms of their multipotency and proliferative and differentiation potential. Due to their multilineage differentiation potential and immunomodulatory properties, MSCs present a promising tool in cell-based therapy for treatment of various nonhematopoietic diseases, such as myocardial infarction, liver cirrhosis, spinal cord injury, cartilage damage and diabetes [1-3]. After the first clinical trial employing MSCs to treat osteogenesis imperfecta published in 1999 [4], the number of registered clinical trials significantly increased, reaching 344 in 2013 [5]. Restoring the viability and function of MSCs in anatomically complex organs (*e.g.* the liver, heart, and brain) remains a challenge for systematic MSC transplantation. Although functional improvements following the delivery

of MSCs have been extensively explored in various diseases, our current understanding of the in vivo behavior and distribution of administered MSCs is limited, which seems to hamper further transition of MSC transplantation from experimental trials to standard clinical procedures. Previous studies showed that most of MSCs were entrapped in the lung immediately after intravenous injection, with some MSCs undergoing apoptosis [6]. After about 10 min, these trapped MSCs gradually returned to the blood circulation and redistributed to other organs [7]. Finally only a small fraction of MSCs were found to survive, migrate to and engraft in the target organs. Thus, it would be important to characterize the *in vivo* distribution of MSCs following intravascular administration to predict their survival and homing to target organs [6].

A number of published model have the potential to characterize the in vivo behavior of administered stem cells. The long-term replication, differentiation, or apoptosis of stem cells could be predicted by stochastic model [8, 9] or time-variant clustering model [10]. A computational cell motility model has been developed to probe the migration mechanism of cells [11]. And the population dynamics of administered cells may be predicted using a recently developed mathematical model [12]. However, none of the above-mentioned published models could elucidate the concentration-time profiles of administered cells in organs. There is still a lack of a proper model to characterize the *in vivo* distribution of administered stem cells. It has been reported that the dynamics of systematically administered MSCs were similar to that of inert micrometer-scale particles injected into the bloodstream of animals [13]. Therefore the complex, yet regulated, *in vivo* kinetics of administered MSCs are amenable to pharmacokinetic model building and analysis. During the past 30 years, physiologically based kinetic (PBK) models have been successfully applied to analyse the kinetics of small molecules, antibodies, nanoparticles and lymphocytes [14, 15]. Such model is based on the anatomical structure of the living systems, with each important organ regarded as an individual compartment. All compartments are connected by blood flow [14]. Compared to empirical kinetic models, PBK modeling has the potential for interspecies scaling, which allows prediction of compound pharmacokinetics in humans using animal data. By systematically examining the effects of changing individual model parameters, PBK models can identify key parameters and their values, and suggest possible strategies for improvements in biodistribution. Therefore, quantitatively analyzing the in vivo distribution of MSCs with PBK modeling has the potential to identify the barriers to MSCs delivery, and propose designs of new formulations and dosing regimens to maximize the therapeutic activity.

In this study, we developed a simple PBK model to characterise the *in vivo* kinetics of MSCs from biodistribution data of green fluorescent protein (GFP) expressed MSCs intravenously injected into mice. Being the first effort to model the distribution of administered stem cells, this model invoked assumptions based on direct visualization of MSCs in specific organs at the cellular level using high resolution multiphoton microscopy. The utility of the model was examined across species and administration routes by extrapolation of this model to rats and humans, as well as to intra-hepatic arterial injection. The clinical utility of the model was also tested with data obtained from stem cell-based therapies to patients with liver cirrhosis. This PBK model provides a general framework for the study of *in vivo* distribution of therapeutic cells to design treatment protocols and to guide future experiments.

5.4 Materials and Methods

5.4.1 Cell preparations

The mouse GFP-MSCs used in this study were kindly provided by Dr. Mike Doran (Queensland University of Technology). The MSCs were isolated, characterized and cultured from inbred C57BL/6 mice transgenic for GFP under the control of the ubiquitin promoter as previously described [16, 17]. All experiments involving MSCs were performed at passage 8-12, tested negative for mycoplasma contamination, and <80% confluence. The average diameter of suspended MSCs was measured from fifty different cells from twelve representative image fields.

5.4.2 *In vivo* transplantation and imaging of MSCs

Male 20-week-old BALB/c nude mice were purchased from the Animal Resource Centre (Perth, Western Australia). All animal procedures were approved by the Animal Ethics Committee of the University of Queensland and were carried out in accordance with Australian Code for the Care and Use of Animals for Scientific Purposes 8th edition. Mice were anaesthetized initially by an intraperitoneally injection of ketamine hydrochloride (80 mg/kg) and xylazine (10 mg/kg). Body temperature was controlled by placing mice on a heating pad set to 37°C. 150 µl of a suspension of 5×10^5 MSCs was injected with a 27 gauge needle through the tail vein. Prior to injection, the MSCs were maintained at 4°C, and the cells were gently resuspended with a pipette to ensure no aggregation before injection.

MPM was performed using the DermaInspect system (Jen-Lab GmbH, Jena, Germany) equipped with an ultrashort (85 fs pulse width) pulsed mode-locked 80-MHz titanium sapphire laser (MaiTai, Spectra Physics, Mount View, CA, USA). The excitation wavelength was set to 740 nm for organ autofluorescence and 900 nm for GFP signals, with emission signal ranges of 350 to 450 nm and 450 to 515 nm established respectively through the use of BG39 bandpass filters (BG39, Schott glass color filter, Schott MG, Mainz, Germany). Images were recorded with oil-immersion 40× objectives (Carl Zeiss, Germany). The laser power was set to 15 mW for 40×magnification imaging, and the acquisition time for obtaining the images was 7.4 seconds per frame. Intravital imaging of the mouse liver was performed as previously described [18, 19]. Twenty-four images from twelve non-overlapping fields were collected per mouse (n = 5) without the use of randomization and blinding. Normal saline was used to keep the liver and other organs moist and attached to the cover glass throughout the experiment. Analysis and overlay of the fluorescence intensity images was done using ImageJ 1.44p (National Institutes of Health, USA). The diameter of cells was measured along three different arbitrary lines within a cell, and tested on eighteen different cells from six representative image fields.

Organ specimens from sites of MPM imaging were fixed in 4% buffered formalin and embedded in paraffin. Serial sections were obtained for Hematoxylin & Eosin (H&E) stain to evaluate histopathologic features. The OlyVIA software 2.6 (Olympus, Münster, Germany) was used to visualise and scan the slides.

5.4.3 Measurement of donor MSCs in recipient organs

Animals (n = 5) were sacrificed at designated times (5 min, 15 min, 1, 3, 10, and 20 hour post-injection). The blood and major organs were removed and weighed. Red blood cells were lysed and single-cell suspensions of organs were obtained as previously described [20]. The total number of GFP-MSCs in each single-cell suspension of organs was measured and analysed by flow cytometry using a FACS Calibur (Accuri C6, BD, San Jose, CA, USA) as previously described [21]. As negative controls, single-cell suspensions of organs from naive mice were run in parallel. Light scattering parameters were set to exclude dead cells and debris.

5.4.4 Mathematical description of the model

The model structure was based on published PBK models simulating the distribution (using distribution coefficient) and uptake-release-excretion processes (using uptake,

release and excretion rate constant) of inert nanoparticles [22]. The model assumes a fast process of MSCs transported into various levels of blood vessels in organs. The partition coefficient P is used to correlate the concentration of MSCs between the blood within the organ and the venous blood leaving the organ. Given that the microvascular environment varies between organs, the partition coefficient is assumed to be different between organs. The equation describing this correlation is:

$$CV_t = \frac{C_{V\_t}}{P_t} \quad (1)$$

where CV_t (cell/L) is the concentration of MSCs in the venous blood leaving the organ *t*, C_{V_t} (cell/L) is the concentration of MSCs in the vascular space within the organ *t*, P_t (unitless) is the partition coefficient of the organ *t*.

Since a fraction of MSCs could be arrested in organs and isolated from blood circulation, these MSCs are described separately as in the extravascular space of organ. In the blood and organs, elimination of MSCs after depletion occurs as a clearance route from the body. The arrest-release-depletion approach of MSCs was described as a first-order process. The equations describing these processes are:

For vascular space

$$V_{V\_t}\frac{dC_{V\_t}}{dt} = Q_t(C_A - CV_t) - K_{arrest\_t}C_{V\_t}V_{V\_t} + K_{release\_t}A_{E\_t} \quad (2)$$

For the arrested MSCs as in the extravascular space

$$\frac{dA_{E\_t}}{dt} = K_{arrest\_t}C_{V\_t}V_{V\_t} - K_{release\_t}A_{E\_t} - K_{depletion\_t}A_{E\_t} \quad (3)$$

V_{V_t} (L) is the volume of blood vessels in the organ *t*, Q_t (L/h) is the blood flow to the organ *t*, C_A (cell/L) is the concentration of MSCs in the arterial blood, A_{E_t} (cell) is the amount of arrested MSCs and isolated from blood circulation as in the extravascular space of organ *t*, K_{arrest_t} (h^{-1}) is the arrest rate constant of MSCs in the organ *t*, K*release_t* (h^{-1}) is the release rate constant of MSCs in the organ *t*, and $K_{depletion\_t}$ (h^{-1}) is the depletion rate constant of MSCs in the organ *t*. Mass balance equations used in the model are presented in the Supplementary Note.

5.4.5 Implementation and parameterization of the model

The PBK model was implemented in Berkeley Madonna version 8.3.18 (Berkeley, CA, USA). Mass balance equations used in the model are presented in the supplementary. All physiological parameter values (body weight, organ volume, blood volume and blood

flow) were from the literature and are given in Table S1. MSC-specific parameters (partition coefficient, arrest rate constant, release rate constant and depletion rate constant) were optimized by using both curve fitter in Berkeley Madonna automatically and a manual approach to obtain a visually reasonable fit to the experimental biodistribution data of GFP- MSCs intravenously injected into mice.

5.4.6 Sensitivity analyses

To determine the effect of the parameters on the model solution, sensitivity analysis was performed for the parameters in the target organs. The value of each parameter was increased by 0.1%, the model simulations were repeated, and the new MSCs concentrations noted. The relative sensitivity coefficients for significant parameters were calculated using the following equation:

$$\text{Relative sensitivity coefficient} = \frac{dC/C}{dP/P} \quad (4)$$

where C (cell/L) is the concentration of MSCs, and P is the parameter value. A positive RSC indicates a direct association between the model output and the corresponding parameter, while a negative RSC suggests the model output is inversely correlated with the specific parameter. The RSC values with absolute values higher than 0.5 are considered as highly sensitive.

5.4.7 Model evaluation with independent data

The predictive capability of our PBK model was evaluated with external datasets from different species [7, 23-26]. To facilitate comparisons among the various studies, all concentrations were normalized to the number of MSCs per kg of organ. The physiological parameter values of rats and humans were obtained from the literature and are given in Table S1. MSC-specific parameters were assumed to be the same for mice, rats and humans. The overall goodness-of-fit between predicted and measured values was further analyzed with linear regression. To compare the predictive capability of model with different parameters, bias (mean prediction error [MPE]) and precision (mean absolute prediction error [MAPE]) are calculated with 95% confidence intervals (CIs) using the following equation:

$$MPE = \frac{\sum(M_{pred} - M_{obs})}{N} \quad (5)$$

$$MAPE = \frac{\sum|M_{pred} - M_{obs}|}{N} \quad (6)$$

where M_{pred} is the predicted value, M_{obs} is the observed value, and N is number of time points. The statistical analysis was done using GraphPad Prism v 6.04 (GraphPad Software Inc., La Jolla, California).

5.5 Results

5.5.1 Disposition of MSCs at organ level

The spatiotemporal disposition of GFP-MSCs in organs at the cellular level was explored using multiphoton microscopy (MPM). **Fig. 5.1A** and **5.1B** shows representative images of MSCs distribution in lung and liver at 30 min after intravenous injection. The MSCs were quickly observed in the microvessels of the lung and liver, instead of extravascular migrating into the surrounding collagens or alveoli of the lung and parenchyma of the liver. The size of MSCs was determined to be 20.1 ± 1.2 μm in mouse blood using MPM (**Supplementary Fig. S5.1**), and confirmed by bright-field microscopy (22.0 ± 2.6 μm, **Supplementary Fig. S5.2**). Some MSCs became passively entrapped in small-diameter blood vessels, and some were found to accumulate and move in vessels with diameters greater than those of MSCs (**Fig. 5.1B**), suggesting the existence of both passive and active organ retention of MSCs. MSCs with smaller sizes (around 10 μm) were observed in organ capillaries (**Fig. 5.1A**), suggesting the possibility of MSC deformability which has been reported previously [27-29]. Few MSC was detected extravascular migrating up to 24 hours following intravenous injection. Fig. 1C depicts the depletion process of one representative MSC in liver captured by real-time intravital imaging. After entrapped into the junction of the terminal portal venule and sinusoids (30 minutes post-injection), cell fragmentation was gradually observed with reduced fluorescence due to cell depletion.

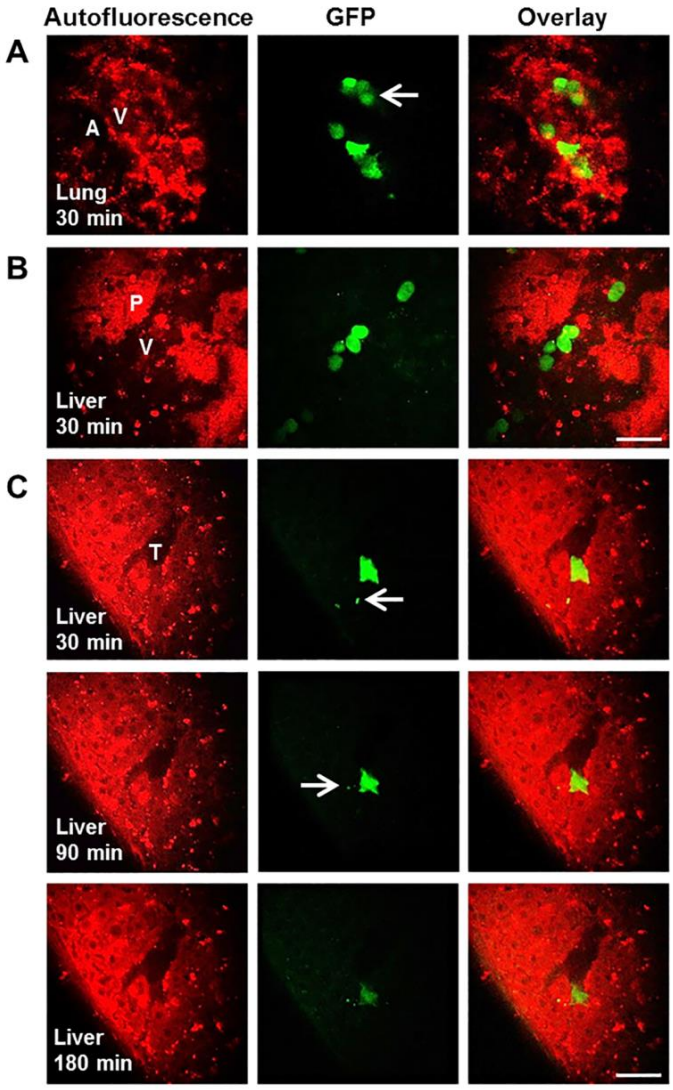

Figure 5.1 Disposition of MSCs at organ level. (A) At 30 minutes post injection, the MSCs were found entrapped in the microvessels of the lung while no cell was found in the surrounding collagens or alveoli in the lung. Some MSCs less than 10 μm in diameter and may pass through the capillaries. (B) At 30 minutes post injection, some MSCs in liver were found accumulated and moving in vessels with diameters greater than those of MSCs and no cell was found extravasate into the liver parenchyma. (C) The depletion of MSC in the liver after intravenous injection. After entrapped at the junction of the terminal portal venule and sinusoids at 30 minutes post-injection, one MSC slowly became fragmented with reduced fluorescence suggestive of depletion. No MSCs was observed to cross the vessel membrane to the liver parenchyma. Images were recorded at $\lambda_{Exc}/\lambda_{Em}$: 740/350 to 450 nm for the endogenous autofluorescence of the lung and liver (red, left column), and $\lambda_{Exc}/\lambda_{Em}$: 900/450 to 515 nm for fluorescence of GFP (green, middle column). The right column represents fused images. Scale bar: 40 μm, and the white arrow points towards the MSCs with smaller sizes. A, alveoli; V, vessels; P, parenchyma; T, terminal portal venule.

5.5.2 Development of PBK model

The PBK model of MSCs in mice was developed based on the above observations and on the published intravital microscopic details of administered MSCs [27-29]. After intravenous injection, MSCs were transported to blood vessels of organs by organ blood flow via the systemic circulation. This process is assumed to be very fast. As shown in Fig. 2A, after reaching the organs, some MSCs became entrapped in microvessels due to their large sizes or temporarily adhered to the endothelial wall. A portion of these entrapped MSCs could be released back to the blood circulation or eliminated after depletion. These arrest-release-depletion processes were assumed to follow first-order kinetics with rate constants of k_{arrest}, $k_{release}$, and $k_{depletion}$, respectively. Tissue integration and differentiation of the arrested MSCs were not included in the model as these processes were much slower [30, 31] and had less impact on the MSC circulation and distribution at the organ level in the short term. All MSCs were assumed to act independently with no intercellular feedback loops or obligatory connections. For example, the entrapment of one MSC would not trigger the apoptosis or release of another. In summary, the in vivo kinetics of MSCs in this model was assumed to be governed by two processes: (1) transport to the organ via systematic circulation; (2) interaction with blood vessels of organs.

To build the PBK model, the whole body was separated into eight compartments: arterial blood, venous blood, lungs, spleen, liver, kidneys, heart and the rest of body. All compartments were interconnected via the systemic blood circulation (**Fig. 5.2B**). Key components included in the model were species-specific physiological parameters (body weight, organ volume and blood flow, given in **Supplementary Table S5.1**) and MSC-specific parameters (partition coefficient, arrest rate constant, release rate constant and depletion rate constant).

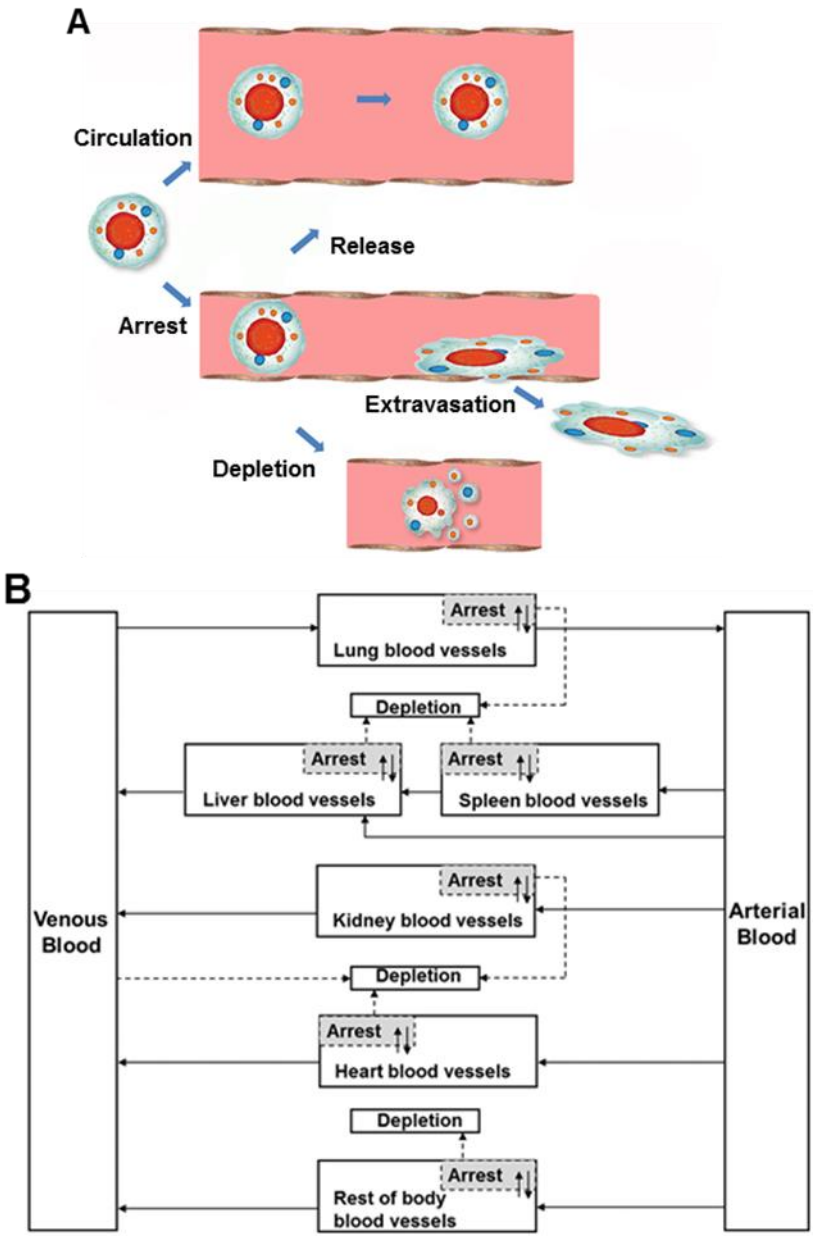

Figure 5.2 Hypothesis and schematic diagram of the PBK model for the *in vivo* fate of MSCs. (A) Assumptions for modeling based on direct visualization of MSCs in specific organs at the cellular level using high resolution multiphoton microscopy. After intravenous injection, MSCs were transported to blood vessels of organs via systemic circulation. After reaching the organs, some MSCs became entrapped in microvessels due to large sizes or adhered to the endothelial wall. These MSCs could be released back to blood circulation or eliminated after depletion. The process of tissue integration and differentiation of the arrested MSCs was much slower extending from 24 to 72 hours post-injection. (B) Schematic diagram of the PBK model for the *in vivo* fate of MSCs. Solid arrows indicate blood flow, dashed grey arrows indicate the depletion of MSCs and grey boxes indicate the arrested MSCs isolated from blood circulation as in the extravascular space of organ.

5.5.3 Comparison of PBK model predictions with experimental data

After intravenous injection, the time profile of MSC levels in venous blood exhibited a two phase decay corresponding to a fast distribution and a relative slow elimination process. Lung, liver, spleen and kidney were major organs of MSC accumulation. MSCs displayed different patterns of concentration-time profiles in these organs. As shown in Fig. 3, the observed time profiles of MSCs concentration in mouse blood and organs were adequately described by the developed PBK model with an overall regression coefficient (R^2) of 0.966 (**Supplementary Fig. S5.3**), indicating high goodness-of-fit of model calibration results. However, despite the adequate overall predictions, it should be noted that the model predicted a rapid decrease of MSC concentration in blood within 5 min after injection. There is a lack of experimental data at this early time point to confirm this, which requires further experiments to either validate this prediction or revise the model accordingly.

Table 1 summarized the MSC-specific parameters for each organ. The highest arrest rate constant was obtained for the lung estimated by curve fitting (5.434 h^{-1}), indicating that MSCs are predominantly entrapped in the lung after *in vivo* administration. Blood showed the highest depletion rate constant (0.636 h^{-1}), suggesting its role as major elimination organ. The depletion rate constant in kidney was found to be highest among all organ compartments (0.151 h^{-1}), which was consistent with the results from whole-body imaging and radioactivity counting of urine after injection of ^{99m}Tc labeled MSCs [24]. Our estimates suggest that about 28% of the transplanted MSCs survive *in vivo* 24 hours after intravenous injection. Similar survival rate have been obtained by intravital imaging of rat cremaster muscle microcirculation to track intraarterially delivered MSCs [27].

To determine the effect of each parameter on the model simulation, a sensitivity analysis was performed. The relative sensitivity coefficient (RSC) for the concentration of MSCs in liver and heart are shown in **Supplementary Fig. S5.4**, because liver cirrhosis and myocardial infarction are two common diseases that have been treated with MSCs clinically. We selected 24 hours post-injection, when the amount of circulating MSCs decreased to a relatively steady state. The concentration of MSCs in the liver at 24 h post injection was highly sensitive to the depletion rate constant of liver, the release rate constant of lung, the partition coefficient and arrest rate constant of liver and lung. Similar effects of these parameters on the heart were observed. The depletion and arrest rate constant of heart, the arrest rate constant of lung, and the partition coefficient of heart and lung had a high impact on the concentration of MSCs in heart at 24 h post injection.

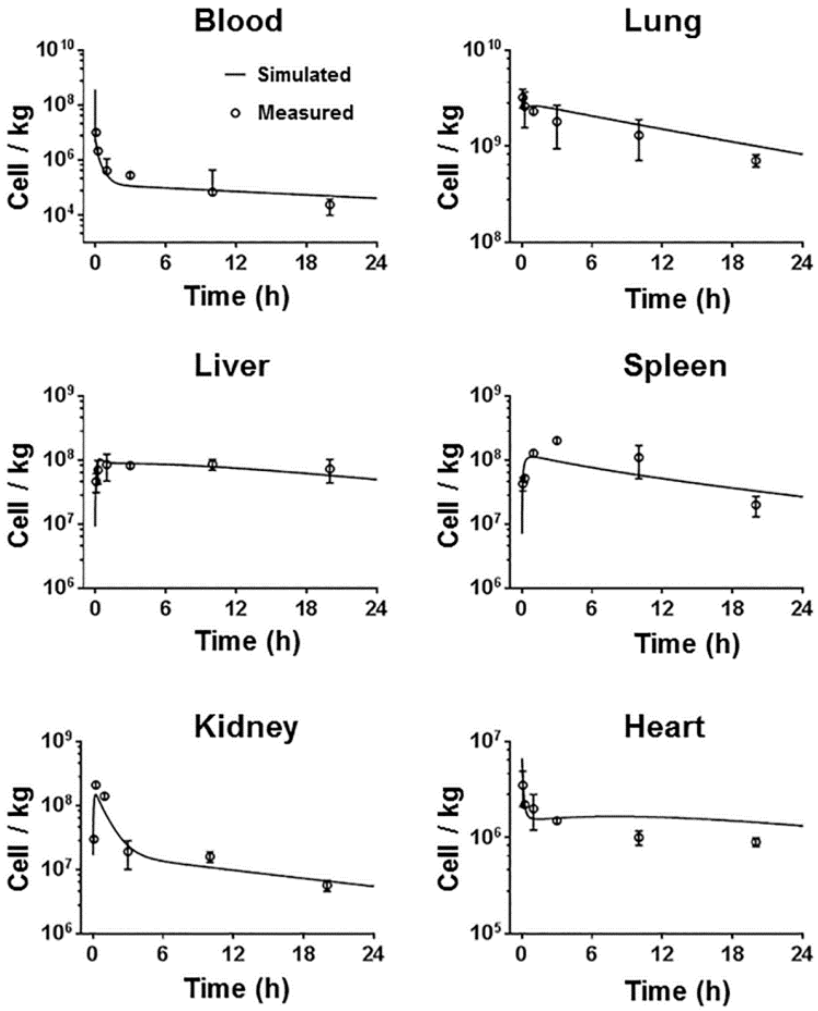

Figure 5.3 Model calibration results with experimental data. Mice were intravenously injected with 5 × 10^5 MSCs (*n* = 5). The solid line in each panel represents the concentration-time profile of the MSCs simulated by the PBK model while the closed circles represent measured biodistribution data. Concentration of the MSCs is expressed as number of cells per kilogram of tissue. The data are expressed as mean ± s.d. The initial concentrations for organs (0 cell/L) are not shown because a base-10 log scale is used for the concentration.

5.5.4 Model evaluation with independent rodent data

The validity of the PBK model was first evaluated with data from Shim *et al*. [26] and Lee *et al*. [7] where MSCs (5 × 10^5 and 2 × 10^6 cells) were intravenously administered to normal and diseased mice. All physiological parameters and MSC-specific parameters in the model were maintained constant. As shown in **Fig. 5.4A**, **C** and **D**, the model adequately predicted the MSC concentrations in blood in normal mice from the dataset of Shim *et al*. [26], and MSC concentrations in lung and heart in normal mice from the dataset of Lee *et al*. [7]. However, as shown in **Fig. 5.4B**, the predicted MSC concentration

in blood only slightly increased at about 3 min post-injection, while Lee *et al.* observed a much more substantial reappearance of MSCs in blood (2% to 3% of administered MSCs) after a lag period about 30 min [7]. A possible reason for this difference could be the different methods of MSC quantification, where the observed data were measured by quantitative assays for DNA of MSCs and our model was based on the data from flow cytometry analysis. Another reason is that mechanistic considerations, such as cell aggregation, changes in flow to organs, were not included in modeling, while these mechanisms might become more relevant to MSC distribution when higher concentration are administered. In the dataset from Shim *et al*. [26], the distribution of MSCs did not differ significantly between normal and osteoarthritis-induced mice. However, the model underestimated the MSC concentration in the heart with myocardial infarction from the dataset of Lee *et al*. [7] (**Fig. 5.4D**), indicating the disease effect on MSC distribution. We then recalibrated the model to data from mice with myocardial infarction [7], to estimate the diseases-specific heart-related parameters (**Supplementary Table S5.2**). As shown in **Fig. 5.4D**, the MSC concentration in the infarcted hearts was more accurately predicted by the same PBK mode with re-estimated diseased-specific parameters than with original parameters (the comparison of precision is shown in **Supplementary Table S5.3**). The re-estimation results indicated that higher concentration of MSC is related to higher arrest and less depletion of MSC in heart in disease status.

To further evaluate the predictive applicability of the PBK model across species, simulations were compared with published experimental data for rat [24]. Physiological parameters of rats (given in **Supplementary Table S5.1**) were obtained from literature [32, 33]. MSC-specific parameters in the model were maintained constant. As shown in **Fig. 5.5**, the MSC concentrations in the lung, liver, spleen, kidneys and heart were predicted adequately by the model, but the blood levels were underestimated. It should be noted that MSCs in that study were ^{99m}Tc labeled and distribution was measured by nuclear imaging. Therefore, residual radioactivity of cell fragments in blood before excretion may result in overestimation of MSC concentration in nuclear imaging. In contrast, our model was based on the data from flow cytometry analysis, which largely reflected the concentration of live cells. Overall, there was a good correlation (R^2 = 0.922) between PBK model estimates and independent rodent data (**Supplementary Fig. S5.5**), indicating that the model shown here is applicable to predict the in vivo distribution of administered MSCs across rodents. However, the time courses of this datasets have only two data points (2 hours and 20 hours) for each organ. More detailed data are needed to adequately evaluate the potential inter-species predictive capability of this model.

Table 5.1 MSC-specific parameters used in the PBK model estimated by curve fitting

Parameter (unit)	Description	Blood	Lung	Liver	Spleen	Kidney	Heart	Rest of body
P (unitless)	Partition coefficients	-	742.733	262.699	1633.24	305.351	3.097	6.765
K_{arrest} (h^{-1})	Arrest rate constant	-	5.434	1.395	0.608	1.727	1.251	0.143
$K_{release}$ (h^{-1})	Release rate constant	-	0.108	0.066	0.856	0.054	0.016	0.957
$K_{depletion}$ (h^{-1})	Depletion rate constant	0.636	0.0589	0.060	0.002	0.151	0.039	0.148

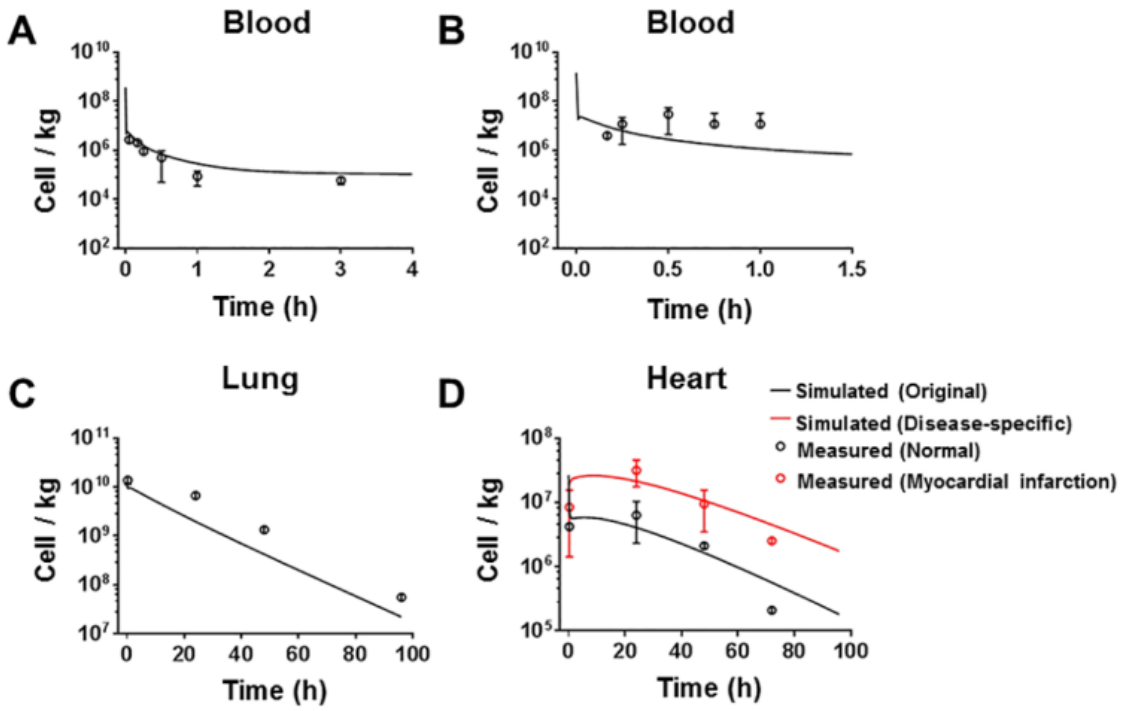

Figure 5.4 Model evaluation results with independent external datasets from mice. (A) Mice were intravenously injected with 5 × 10^5 MSCs [26] (n = 5). (B, C and D) Mice were intravenously injected with 2 × 10^6 MSCs [7] (n = 6). The solid line in each panel represents the concentration-time profile of the MSCs simulated by the PBK model while the closed circles represent measured biodistribution data. Concentration of the MSCs is expressed as number of cells per kilogram of tissue. The data are expressed as mean ± s.d. The initial concentrations for organs (0 cell/L) are not shown because a base-10 log scale is used for the concentration.

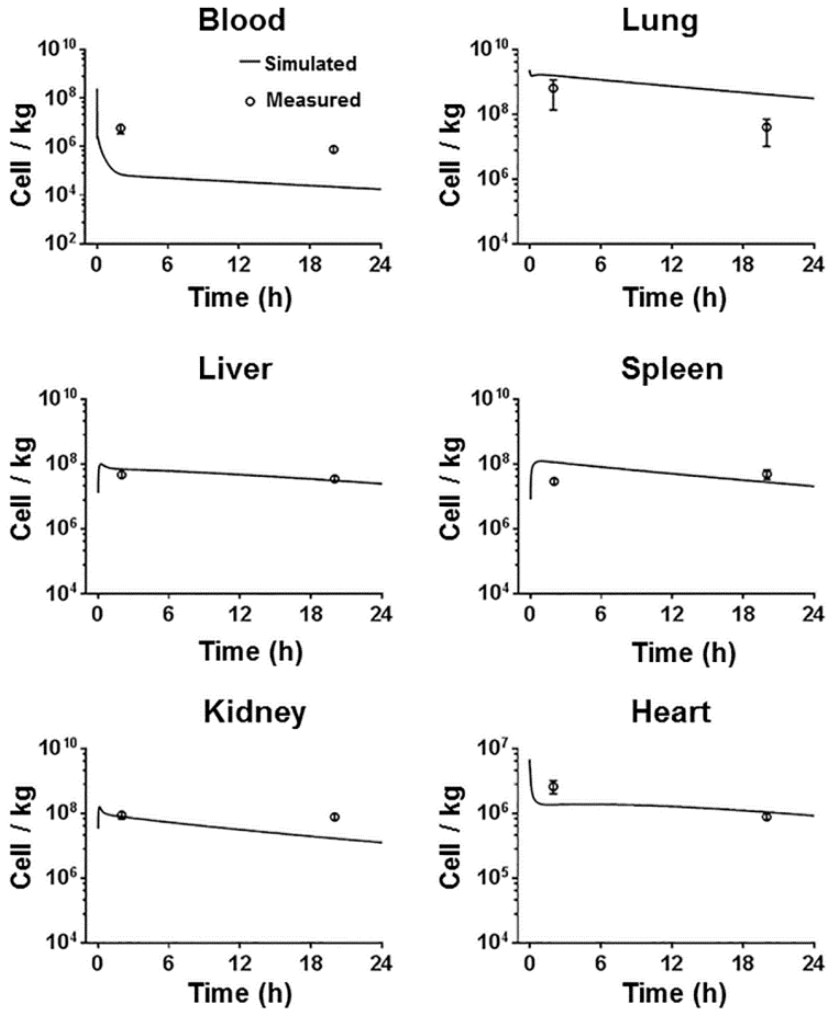

Figure 5.5 Model evaluation results with independent external datasets from rats. Rats were intravenously injected with 3.2×10^6 MSCs [24] (*n*=9). The solid line in each panel represents the concentration-time profile of the MSCs simulated by the PBK model while the closed circles represent measured biodistribution data. Concentration of the MSCs is expressed as number of cells per kilogram of tissue. The data are expressed as mean ± s.d. The initial concentrations for organs (0 cell/L) are not shown because a base-10 log scale is used for the concentration.

5.5.5 Model predicting the *in vivo* distribution of therapeutic stem cells in humans

This model was used to predict the *in vivo* distribution of the therapeutic stem cells in patients with liver cirrhosis after intravenous or intra-hepatic arterial injection. Physiological parameters of humans (given in **Supplementary Table S5.1**) were obtained from literature [32, 33, 34], MSC-specific parameters in the model were maintained constant. As shown in Fig. 6A, our model suggests that the time profiles of MSC concentration in liver significantly differ between patients after intravenous or intra-hepatic arterial injection of the same number (8.5×10^8) of MSCs. The model successfully predicted the proportion of

bone marrow-derived mononuclear cells (BMMCs) in the liver to the whole body at 3 and 24 hours after injection for the data from Couto *et al*. [23] (**Fig. 5.6B**). However, it underestimated the proportion of MSCs in the liver to the whole body after intra-hepatic arterial injection for the data from Gholamrezanezhad *et al*. [25] (**Fig. 5.6C**). We then recalibrated the model to data from human with liver cirrhosis [25], to estimate the diseases-specific liver-related parameters (**Table S5.2**). As shown in **Fig. 5.6D**, the MSC concentration in the cirrhotic liver was more accurately predicted by the same PBK mode with re-estimated diseased-specific parameters than with original parameters (the comparison of precision is shown in **Supplementary Table S5.3**). The re-estimation results indicated that higher concentration of MSC is related to higher partition and arrest of MSC in liver in disease status.

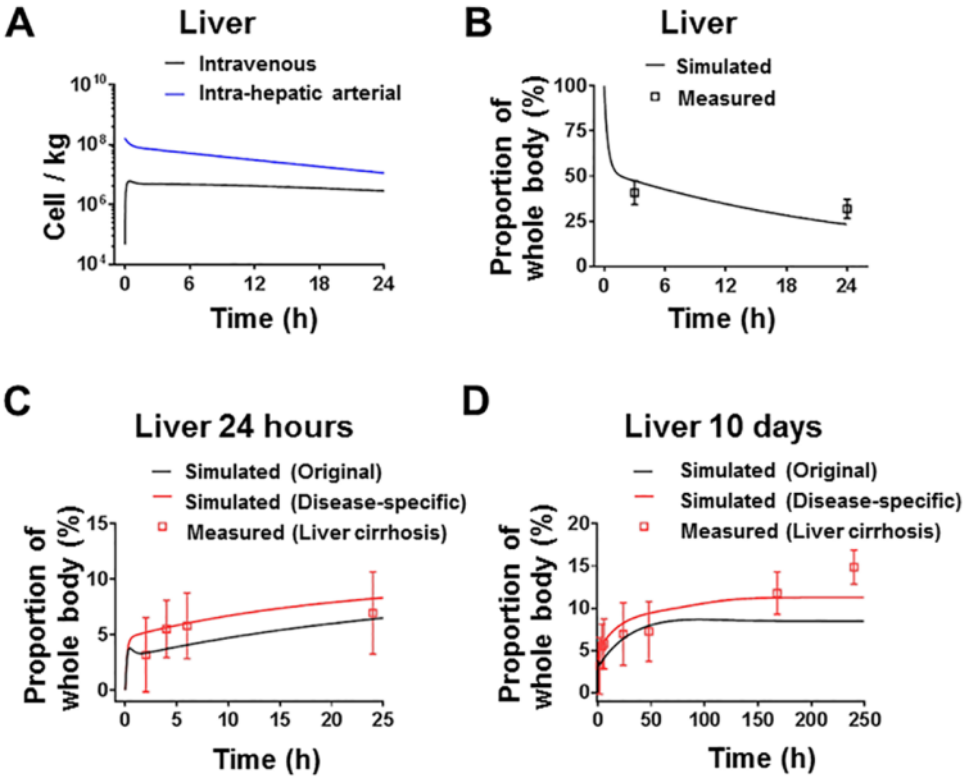

Figure 5.6 Model evaluation results with independent external datasets from humans. (A) The PBK model suggests that the time profiles of MSC concentration in liver significantly differ between patients after intravenous or intra-hepatic arterial injection of the same number (8.5×10^8) of MSCs. (B) Patients were intra-hepatic arterially injected with an average of 8.5×10^8 radiolabeled BMMCs [23] ($n = 8$). (C and D) Patients were intra-hepatic arterially injected with an average of 3.2×10^8 radiolabeled MSCs for 24 hours and 10 days, respectively [25] ($n = 4$). The residual radioactivity in the liver is expressed as the proportion of the whole body radioactivity. The solid line in each panel represents the

concentration-time profile of the cells simulated by the PBK model while the closed squares represent measured biodistribution data. The data are expressed as mean ± s.d.

5.6 Discussion

Although hundreds of studies have reported the cell biodistribution in the field of stem cell-based therapy, no integrating model characterizing the *in vivo* kinetics of these cells has been developed with respect to pharmacological effects and therapeutic thresholds. In the present study, we developed a model based on direct visualization of GFP-labeled MSCs disposition in the mice at the cellular level in specific organs. Importantly, the mouse cells used in this study were expanded to a similar size as the human MSCs currently used in clinical trials. Compared with the previously published PBK model of lymphocytes [15], our model is especially applicable to circulating cells with large sizes (MSCs or cancer cells are 1.5 to 4 times larger than lymphocytes). This model is more useful for clinical applications since a less complicated framework and parameters were employed. In the future, the predictive power of this model is likely to improve with the incorporation of new parameter values or advanced microscopic details as they become available.

One of the advantages of PBK modeling over traditional empirical kinetic modeling is the ability to provide time profiles of cell concentration in individual organs. The *in vivo* distribution of MSCs characterized mathematically in the present study will better inform the dosing regimens of cell-based therapies. For example, it may be expected that higher administered numbers of MSCs should result in more MSC engraftment and better functional outcomes. However, in a rat model of brain injury, no additional enhancement of neurological function was observed after increasing the dose of intravenous injected MSCs by 3-fold [35]. Thus, simply increasing the number of delivered cells may not improve the overall outcome. The sensitivity analysis of our PBK model showed that the accumulation of MSCs in the lung adversely affected the delivery of therapeutic cells to other target organs, evident by the concentrations of MSCs in the target organs were sensitive to changes in the partition coefficient, arrest or release rate constant in the lung. The partition coefficient, arrest and depletion rate constant in target organs also had a high impact on the concentration of MSCs. Thus, instead of increasing the dose, possible strategies to further improve the target efficiency of cell-based therapies would be bypassing the initial lung entrapment and enhancing organ-specific capture by modulating cell surface properties. Our model as well as some published data [7, 24, 26] revealed slow MSC elimination rates in blood, liver, kidney and heart. However, the cell quantity is influenced by the sensitivity and specificity of measurement methods. The background noise of

signals in the recipient organs could be misinterpreted as slow MSC elimination rates. It is critical that future MSC experiments use more advanced measurement methods for modelling.

Administration of MSCs into the arterial supply of the liver was examined in this study as an alternative route of intravenous injection to bypass lung entrapment. The inter-route extrapolation of this PBK model suggests that accumulation of MSCs in the liver significantly differs after intravenous and intra-hepatic arterial injection. Our PBK model confirmed that direct delivery of MSCs to the target organs may improve the therapeutic efficacy by increasing the accumulation of surviving cells in those organs. Compared to intravenous injection, transplantation via hepatic artery or portal vein could increase the amount of MSCs in the liver at 24 hours post-injection by 4-fold in humans (**Fig. 6A**), in agreement with the therapeutic efficacy study of the MSCs treatment of fulminant hepatic failure in pigs [36]. Our PBK model also allows the scale-up from the mice data to humans. In many studies on cell therapy, an accurate concentration of cells in organs is not available from humans [37]. One should be cautious in direct translation of the distribution results from mice to humans due to different concentration-time profiles of MSCs in organs between species. This PBK model could provide more accurate prediction by scaling up the profile from mice to human.

There is substantial evidence that administered MSCs would accumulate within sites of disease or injury. Local changes in microvessels and organ-derived attractants have been reported to affect the arrest and entrapment of MSCs in diseased organs [28], while the time profiles of cell concentrations in unaffected organs may only slightly decrease [24]. Thus, parameter values of diseased organs in the PBK model would be different from normal organs. In the present model, MSC-specific parameters of diseased organs for myocardial infarction and liver cirrhosis were optimized separately from respective datasets, because these parameters were considered to be the most influential in the *in vivo* distribution of MSCs in disease, while other less influential parameters were kept the same. It would be of importance to investigate the MSC-specific parameters of target organs for each main type of diseases in the future.

In summary, we present the first model for characterizing and predicting the *in vivo* distribution of administered MSCs. Key ingredients in the model are species-specific physiological parameters (body weight, organ volume, blood volume and blood flow) and cell-specific parameters (partition coefficient, arrest rate, release rate and depletion rate). This model has been validated with multiple external datasets under widely different conditions and in different species, indicating potential inter-route and inter-species

predictive capability. Based on our analysis, possible strategies to improve efficiency of cell-based therapies include bypassing the initial lung entrapment with administration to the arterial supply of target organs and enhancing organ-specific capture by modulating cell surface properties. This PBK model can be extended to other types of circulating cells by adapting the cell-specific parameters, and provides a general framework for the study of the in vivo distribution of therapeutic cells to design treatment protocols.

References

[1] Fox IJ, Daley GQ, Goldman SA, Huard J, Kamp TJ, Trucco M. Stem cell therapy. Use of differentiated pluripotent stem cells as replacement therapy for treating disease. Science (New York, NY). 2014;345:1247391.

[2] Blade J, Rosinol L, Cibeira MT, Rovira M, Carreras E. Hematopoietic stem cell transplantation for multiple myeloma beyond 2010. Blood. 2010;115:3655-63.

[3] Armstrong JP, Shakur R, Horne JP, Dickinson SC, Armstrong CT, Lau K, et al. Artificial membrane-binding proteins stimulate oxygenation of stem cells during engineering of large cartilage tissue. Nature communications. 2015;6:7405.

[4] Horwitz EM, Prockop DJ, Fitzpatrick LA, Koo WW, Gordon PL, Neel M, et al. Transplantability and therapeutic effects of bone marrow-derived mesenchymal cells in children with osteogenesis imperfecta. Nature medicine. 1999;5:309-13.

[5] Wei X, Yang X, Han ZP, Qu FF, Shao L, Shi YF. Mesenchymal stem cells: a new trend for cell therapy. Acta pharmacologica Sinica. 2013;34:747-54.

[6] Bagi Z, Kaley G. Where have all the stem cells gone? Circulation research. 2009;104:280-1.

[7] Lee RH, Pulin AA, Seo MJ, Kota DJ, Ylostalo J, Larson BL, et al. Intravenous hMSCs improve myocardial infarction in mice because cells embolized in lung are activated to secrete the anti-inflammatory protein TSG-6. Cell stem cell. 2009;5:54-63.

[8] Abkowitz JL, Golinelli D, Harrison DE, Guttorp P. In vivo kinetics of murine hemopoietic stem cells. Blood. 2000;96:3399-405.

[9] Abkowitz JL, Catlin SN, Guttorp P. Evidence that hematopoiesis may be a stochastic process in vivo. Nature medicine. 1996;2:190-7.

[10] Huang W, Cao X, Biase FH, Yu P, Zhong S. Time-variant clustering model for understanding cell fate decisions. Proceedings of the National Academy of Sciences of the United States of America. 2014;111:E4797-806.

[11] Shao D, Levine H, Rappel WJ. Coupling actin flow, adhesion, and morphology in a computational cell motility model. Proceedings of the National Academy of Sciences of the United States of America. 2012;109:6851-6.
[12] Hogan T, Gossel G, Yates AJ, Seddon B. Temporal fate mapping reveals age-linked heterogeneity in naive T lymphocytes in mice. Proceedings of the National Academy of Sciences of the United States of America. 2015;112:E6917-26.
[13] Parekkadan B, Milwid JM. Mesenchymal stem cells as therapeutics. Annual review of biomedical engineering. 2010;12:87-117.
[14] Li M, Al-Jamal KT, Kostarelos K, Reineke J. Physiologically based pharmacokinetic modeling of nanoparticles. ACS nano. 2010;4:6303-17.
[15] Zhu H, Melder RJ, Baxter LT, Jain RK. Physiologically based kinetic model of effector cell biodistribution in mammals: implications for adoptive immunotherapy. Cancer research. 1996;56:3771-81.
[16] Cook MM, Futrega K, Osiecki M, Kabiri M, Kul B, Rice A, et al. Micromarrows--three-dimensional coculture of hematopoietic stem cells and mesenchymal stromal cells. Tissue engineering Part C, Methods. 2012;18:319-28.
[17] Markway BD, Tan GK, Brooke G, Hudson JE, Cooper-White JJ, Doran MR. Enhanced chondrogenic differentiation of human bone marrow-derived mesenchymal stem cells in low oxygen environment micropellet cultures. Cell transplantation. 2010;19:29-42.
[18] Wang H, Liang X, Mohammed YH, Thomas JA, Bridle KR, Thorling CA, et al. Real-time histology in liver disease using multiphoton microscopy with fluorescence lifetime imaging. Biomedical optics express. 2015;6:780-92.
[19] Liang X, Grice JE, Zhu Y, Liu D, Sanchez WY, Li Z, et al. Intravital multiphoton imaging of the selective uptake of water-dispersible quantum dots into sinusoidal liver cells. Small (Weinheim an der Bergstrasse, Germany). 2015;11:1711-20.
[20] Oostendorp RA, Ghaffari S, Eaves CJ. Kinetics of in vivo homing and recruitment into cycle of hematopoietic cells are organ-specific but CD44-independent. Bone marrow transplantation. 2000;26:559-66.
[21] Casiraghi F, Azzollini N, Cassis P, Imberti B, Morigi M, Cugini D, et al. Pretransplant infusion of mesenchymal stem cells prolongs the survival of a semiallogeneic heart transplant through the generation of regulatory T cells. Journal of immunology (Baltimore, Md : 1950). 2008;181:3933-46.
[22] Lin Z, Monteiro-Riviere NA, Riviere JE. A physiologically based pharmacokinetic model for polyethylene glycol-coated gold nanoparticles of different sizes in adult mice. Nanotoxicology. 2015:1-11.

[23] Couto BG, Goldenberg RC, da Fonseca LM, Thomas J, Gutfilen B, Resende CM, et al. Bone marrow mononuclear cell therapy for patients with cirrhosis: a Phase 1 study. Liver international : official journal of the International Association for the Study of the Liver. 2011;31:391-400.
[24] Detante O, Moisan A, Dimastromatteo J, Richard MJ, Riou L, Grillon E, et al. Intravenous administration of 99mTc-HMPAO-labeled human mesenchymal stem cells after stroke: in vivo imaging and biodistribution. Cell transplantation. 2009;18:1369-79.
[25] Gholamrezanezhad A, Mirpour S, Bagheri M, Mohamadnejad M, Alimoghaddam K, Abdolahzadeh L, et al. In vivo tracking of 111In-oxine labeled mesenchymal stem cells following infusion in patients with advanced cirrhosis. Nuclear medicine and biology. 2011;38:961-7.
[26] Shim G, Lee S, Han J, Kim G, Jin H, Miao W, et al. Pharmacokinetics and in vivo fate of intra-articularly transplanted human bone marrow-derived clonal mesenchymal stem cells. Stem cells and development. 2015;24:1124-32.
[27] Toma C, Wagner WR, Bowry S, Schwartz A, Villanueva F. Fate of culture-expanded mesenchymal stem cells in the microvasculature: in vivo observations of cell kinetics. Circulation research. 2009;104:398-402.
[28] Karp JM, Leng Teo GS. Mesenchymal stem cell homing: the devil is in the details. Cell stem cell. 2009;4:206-16.
[29] Teo GS, Yang Z, Carman CV, Karp JM, Lin CP. Intravital imaging of mesenchymal stem cell trafficking and association with platelets and neutrophils. Stem cells (Dayton, Ohio). 2015;33:265-77.
[30] Hass R, Kasper C, Bohm S, Jacobs R. Different populations and sources of human mesenchymal stem cells (MSC): A comparison of adult and neonatal tissue-derived MSC. Cell communication and signaling : CCS. 2011;9:12.
[31] Schmidt A, Ladage D, Steingen C, Brixius K, Schinkothe T, Klinz FJ, et al. Mesenchymal stem cells transmigrate over the endothelial barrier. European journal of cell biology. 2006;85:1179-88.
[32] Brown RP, Delp MD, Lindstedt SL, Rhomberg LR, Beliles RP. Physiological parameter values for physiologically based pharmacokinetic models. Toxicology and industrial health. 1997;13:407-84.
[33] Wiedeman MP. Dimensions of blood vessels from distributing artery to collecting vein. Circulation research. 1963;12:375-8.

[34] Martins PN, Neuhaus P. Surgical anatomy of the liver, hepatic vasculature and bile ducts in the rat. Liver international : official journal of the International Association for the Study of the Liver. 2007;27:384-92.
[35] Wu J, Sun Z, Sun HS, Wu J, Weisel RD, Keating A, et al. Intravenously administered bone marrow cells migrate to damaged brain tissue and improve neural function in ischemic rats. Cell transplantation. 2008;16:993-1005.
[36] Li J, Zhang L, Xin J, Jiang L, Li J, Zhang T, et al. Immediate intraportal transplantation of human bone marrow mesenchymal stem cells prevents death from fulminant hepatic failure in pigs. Hepatology (Baltimore, Md). 2012;56:1044-52.
[37] Togel F, Yang Y, Zhang P, Hu Z, Westenfelder C. Bioluminescence imaging to monitor the in vivo distribution of administered mesenchymal stem cells in acute kidney injury. American journal of physiology Renal physiology. 2008;295:F315-21.

Supporting Information

Supplementary Figures

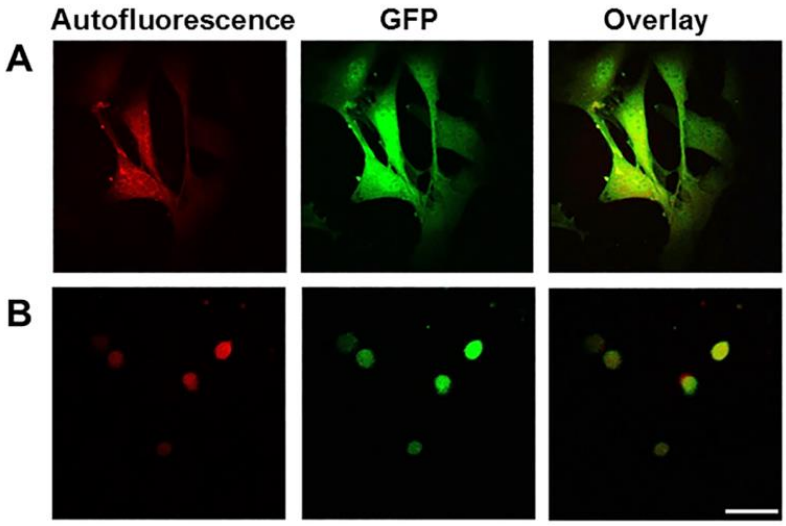

Figure S5.1 Morphology of MSCs *in vitro* imaged by MPM. (A) MSCs proliferated in the culture plate had a typical fibroblast-like morphology and were evenly distributed on the plate. (B) The suspended MSCs in mouse blood. Images were recorded at $\lambda_{Exc}/\lambda_{Em}$: 740/350 to 450 nm for the endogenous autofluorescence of MSCs (red, left column), and $\lambda_{Exc}/\lambda_{Em}$: 900/450 to 515 nm for fluorescence of GFP (green, middle column). The right column represents fused images. Scale bar: 40 μm.

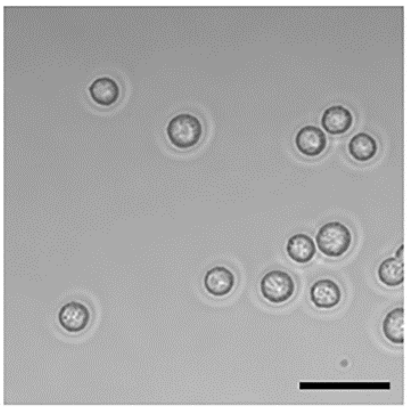

Figure S5.2 Morphology of MSCs *in vitro* imaged by bright-field microscopy. The MSCs were suspended in PBS. Scale bar: 40 μm.

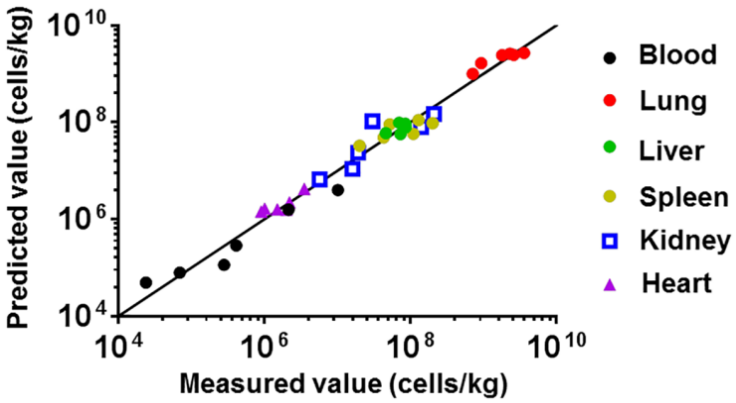

Figure S5.3 Goodness-of-fit plot of model calibration. Model predictions and experimental data were analysed using linear regression. The linear regression coefficient (R^2) is 0.966 (n = 36).

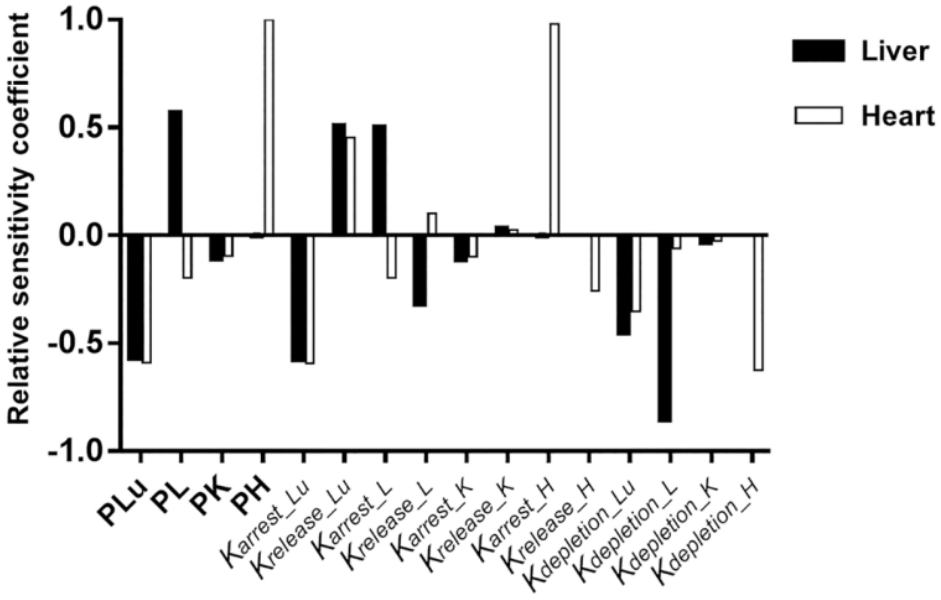

Figure S5.4 Sensitivity analyses for the MSC concentration in mouse liver and heart. Positive values indicate that MSC concentration increases when the parameter value increases, while negative values indicate that MSC concentration decreases when the parameter value increases. P, partition coefficient; K_{arrest}, arrest rate constant; $K_{release}$, release rate constant; $K_{depletion}$, depletion rate constant; Lu, lung; L, liver; K, kidney; H, heart.

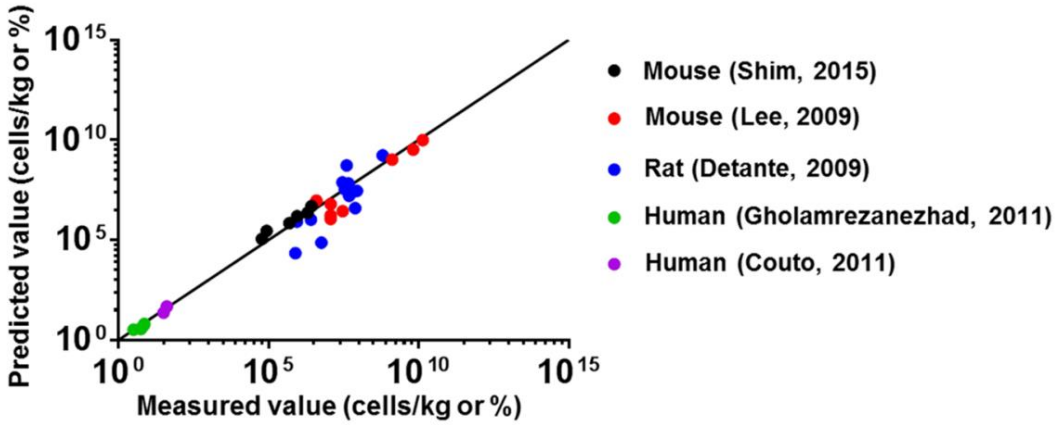

Figure S5.5 Goodness-of-fit plot of model evaluation. Model predictions and experimental data from independent external studies [1-5] were analyzed using linear regression. The linear regression coefficient (R^2) is 0.922 (n = 41).

Supplementary Tables

Table S5.1 Physiological parameters used in the PBK model

Parameter (unit)	Mouse	Rat	Human
Body weight (kg)	0.02	0.25	70
Cardiac output (L/hour/kg$^{0.75}$)	16.5	15	12.89
Blood flow to organ (fraction of cardiac output, unitless)			
Lung	1.00	1.00	1.00
Liver	0.161	0.25	0.227
Spleen	0.011	0.01125	0.01205
Kidney	0.091	0.141	0.175
Heart	0.035	0.035	0.037
Organ volumes (fraction of body weight, unitless)			
Lung	0.007	0.005	0.014
Liver	0.055	0.034	0.026
Spleen	0.005	0.0025	0.0026
Kidney	0.0017	0.007	0.00448
Heart	0.004	0.0022	0.0048
Blood	0.0085	0.074	0.079
Volume fraction of blood in organs (unitless)			
Lung	0.50	0.36	0.30
Liver	0.31	0.21	0.11
Spleen	0.17	0.22	0.51
Kidney	0.24	0.16	0.36
Heart	0.26	0.26	0.07
Rest of body	0.04	0.04	0.01

All values are from the literature [6-8].

Table S5.2 Disease-specific parameters of target organs estimated by curve fitting

Parameter (unit)	Description	Liver (Cirrhosis)	Heart (MI)
P (unitless)	Partition coefficient	376.074	2.311
K_{arrest} (h^{-1})	Arrest rate constant	5.793	6.823
$K_{release}$ (h^{-1})	Release rate constant	0.094	0.025
$K_{depletion}$ (h^{-1})	Depletion rate constant	0.098	0.029

MI: myocardial infarction.

Table S5.3 Predictive capability of the PBK model with original or disease-specific parameters

Variable	Disease	Parameter	Bias (MPE, SEM)	Precision (MAPE, SEM)
MSC concentration of heart	MI	Original	1.079×10^7 (7.898×10^6)	1.113×10^7 (7.659×10^6)
		Disease-specific	2.975×10^6 (4.778×10^6)	7.361×10^6 (4.038×10^5)
Proportion of MSCs in the liver	Cirrhosis	Original	-1.186 (0.3817)	1.242 (0.3343)
		Disease-specific	0.060 (0.3885)	0.690 (0.1812)

MI: myocardial infarction

MPE: mean prediction error

MAPE: mean absolute prediction error

SEM: standard error of the mean

Supplementary equations

Mass balance equations

For venous blood:

$$V_{Vb}\frac{dCV_{Vb}}{dt} = (Q_L CV_L + Q_S CV_L + Q_K CV_K + Q_H CV_H + Q_{Bo} CV_{Bo}) - Q_{Lu} CV_{Vb} - K_{depletion\_v} V_{Vb} CV_{Vb}$$

For arterial blood:

$$V_A\frac{dC_A}{dt} = Q_{Lu}(C_{V\_Lu} - C_A)$$

For lung:

$$CV_{Lu} = \frac{C_{V\_Lu}}{P_{Lu}}$$

For vascular space

$$V_{V\_Lu}\frac{dC_{V\_Lu}}{dt} = Q_{Lu}(CV_{Vb} - CV_{Lu}) - K_{arrest\_Lu} C_{V\_Lu} V_{V\_Lu} + K_{release\_Lu} A_{E\_Lu}$$

For the arrested MSCs as in the extravascular space

$$\frac{dA_{E\_Lu}}{dt} = K_{arrest\_Lu} C_{V\_Lu} V_{V\_Lu} - K_{release\_Lu} A_{E\_Lu} - K_{depletion\_Lu} \times A_{E\_Lu}$$

MSC concentration in the lung is given by:

$$C_{Total\_Lu} = \frac{C_{V\_Lu} V_{V\_Lu} + A_{E\_Lu}}{V_{Lu}}$$

For liver:

$$CV_L = \frac{C_{V\_L}}{P_L}$$

For vascular space

$$V_{V\_L}\frac{dC_{V\_L}}{dt} = Q_L C_A + Q_S C_{V\_S} - (Q_L + Q_S) C_{V\_L} - K_{arrest\_L} C_{V\_L} V_{V\_L} + K_{release\_L} A_{E\_L}$$

For the arrested MSCs as in the extravascular space

$$\frac{dA_{E\_L}}{dt} = K_{arrest\_L} C_{V\_L} V_{V\_L} - K_{release\_L} A_{E\_L} - K_{depletion\_L} \times A_{E\_L}$$

MSC concentration in the liver is given by:

$$C_{Total\_L} = \frac{C_{V\_L}V_{V\_L} + A_{E\_L}}{V_L}$$

For spleen:

$$CV_S = \frac{C_{V\_S}}{P_S}$$

For vascular space

$$V_{V\_S}\frac{dC_{V\_S}}{dt} = Q_S(C_A - CV_S) - K_{arrest\_S}C_{V\_S}V_{V\_S} + K_{release\_S}A_{E\_S}$$

For the arrested MSCs as in the extravascular space

$$\frac{dA_{E\_S}}{dt} = K_{arrest\_S}C_{V\_S}V_{V\_S} - K_{release\_S}A_{E\_S} - K_{depletion\_S} \times A_{E\_S}$$

MSC concentration in the spleen is given by:

$$C_{Total\_S} = \frac{C_{V\_S}V_{V\_S} + A_{E\_S}}{V_S}$$

For kidney:

$$CV_K = \frac{C_{V\_K}}{P_K}$$

For vascular space

$$V_{V\_K}\frac{dC_{V\_K}}{dt} = Q_K(C_A - CV_K) - K_{arrest\_K}C_{V\_K}V_{V\_K} + K_{release\_K}A_{E\_K}$$

For the arrested MSCs as in the extravascular space

$$\frac{dA_{E\_K}}{dt} = K_{arrest\_K}C_{V\_K}V_{V\_K} - K_{release\_K}A_{E\_K} - K_{depletion\_K} \times A_{E\_K}$$

MSC concentration in the kidney is given by:

$$C_{Total\_K} = \frac{C_{V\_K}V_{V\_K} + A_{E\_K}}{V_K}$$

For heart:

$$CV_H = \frac{C_{V\_H}}{P_H}$$

For vascular space

$$V_{V\_H}\frac{dC_{V\_H}}{dt} = Q_H(C_A - CV_H) - K_{arrest\_H}C_{V\_H}V_{V\_H} + K_{release\_H}A_{E\_H}$$

For the arrested MSCs as in the extravascular space

$$\frac{dA_{E\_H}}{dt} = K_{arrest\_H}C_{V\_H}V_{V\_H} - K_{release\_H}A_{E\_H} - K_{depletion\_H} \times A_{E\_H}$$

MSC concentration in the heart is given by:

$$C_{Total\_H} = \frac{C_{V\_H}V_{V\_H} + A_{E\_H}}{V_H}$$

For the rest of the body:

$$CV_{Bo} = \frac{C_{V\_Bo}}{P_{Bo}}$$

For vascular space

$$V_{V\_Bo}\frac{dC_{V\_Bo}}{dt} = Q_{Bo}(C_A - CV_{Bo}) - K_{arrest\_Bo}C_{V\_Bo}V_{V\_Bo} + K_{release\_Bo}A_{E\_Bo}$$

For the arrested MSCs as in the extravascular space

$$\frac{dA_{E\_Bo}}{dt} = K_{arrest\_Bo}C_{V\_Bo}V_{V\_Bo} - K_{release\_Bo}A_{E\_Bo} - K_{depletion\_Bo} \times A_{E\_Bo}$$

MSC concentration in the rest of body is given by:

$$C_{Total\_Bo} = \frac{C_{V\_Bo}V_{V\_Bo} + A_{E\_Bo}}{V_{Bo}}$$

Nomenclature (units)

A_E: Amount of arrested MSCs as in the extravascular space of each compartment (cell)

C_{Total}: Average MSC concentration of each compartment (cell/kg)

C_V: MSC concentration in the vascular space of each compartment (cell/kg)

CV: MSC concentration in the venous blood (cell/kg)

K_{arrest}: Arrest rate constant of MSCs (h^{-1})

$K_{release}$: Release rate constant of MSCs (h^{-1})

$K_{depletion}$: Depletion rate constant of MSCs in the organ (h^{-1})

P: Partition coefficient (unitless)

Q: Blood flow to each organ (L/h)

V: Total volume of each compartment (L)

V_V: Volume of vascular space of each compartment (L)

Subscripts

Vb: Venous blood

A: Arterial blood

Lu: Lung

L: Liver

S: Spleen

K: Kidney

H: Heart

Bo: The rest of body

Supplementary References

[1] Shim G, Lee S, Han J, Kim G, Jin H, Miao W, et al. Pharmacokinetics and in vivo fate of intra-articularly transplanted human bone marrow-derived clonal mesenchymal stem cells. Stem cells and development. 2015;24:1124-32.

[2] Lee RH, Pulin AA, Seo MJ, Kota DJ, Ylostalo J, Larson BL, et al. Intravenous hMSCs improve myocardial infarction in mice because cells embolized in lung are activated to secrete the anti-inflammatory protein TSG-6. Cell stem cell. 2009;5:54-63.

[3] Detante O, Moisan A, Dimastromatteo J, Richard MJ, Riou L, Grillon E, et al. Intravenous administration of 99mTc-HMPAO-labeled human mesenchymal stem cells after stroke: in vivo imaging and biodistribution. Cell transplantation. 2009;18:1369-79.

[4] Gholamrezanezhad A, Mirpour S, Bagheri M, Mohamadnejad M, Alimoghaddam K, Abdolahzadeh L, et al. In vivo tracking of 111In-oxine labeled mesenchymal stem cells following infusion in patients with advanced cirrhosis. Nuclear medicine and biology. 2011;38:961-7.

[5] Couto BG, Goldenberg RC, da Fonseca LM, Thomas J, Gutfilen B, Resende CM, et al. Bone marrow mononuclear cell therapy for patients with cirrhosis: a Phase 1 study. Liver international : official journal of the International Association for the Study of the Liver. 2011;31:391-400.

[6] Brown RP, Delp MD, Lindstedt SL, Rhomberg LR, Beliles RP. Physiological parameter values for physiologically based pharmacokinetic models. Toxicology and industrial health. 1997;13:407-84.

[7] Sterner TR, Ruark CD, Covington TR, Yu KO, Gearhart JM. A physiologically based pharmacokinetic model for the oxime TMB-4: simulation of rodent and human data. Archives of toxicology. 2013;87:661-80.
[8] Zomer A, Maynard C, Verweij FJ, Kamermans A, Schafer R, Beerling E, et al. In Vivo imaging reveals extracellular vesicle-mediated phenocopying of metastatic behavior. Cell. 2015;161:1046-57.

Chapter 6

Conclusion and future directions

6.1 Summary of Findings

The light based systems, multi-photon (MPM) and fluorescence lifetime imaging (FLIM), now provide mini-invasive quantitative imaging of fluorescent molecules in *in situ* and *in vivo* biological tissues and organs - in space (three dimensions), in time, in spectra, in lifetime and in fluorescence anisotropy (total of 7 dimensions). However, currently, their application in the liver is limited. This PhD project has advanced the application of MPM-FLIM for diagnosis of liver diseases and prediction of treatment responses. The main achievements include three aspects:

1. A reliable and standardised method of stain-free and real-time histology for diseased liver has been established based on optical biopsy using MPM-FLIM (**Chapter 3**). Histopathological hallmarks of fibrotic liver, fatty liver, cancerous liver and liver with ischemia-reperfusion injury have been directly visualised by MPM-FLIM *in vivo* without biopsy or administration of fluorescent dyes. The acquired images were comparable with conventional histology, but provided additional information (e.g. redistribution of stellate cell as revealed by autofluorescence and lifetime changes), which cannot be obtained from conventional histology. MPM-FLIM has potential to serve as a diagnostic tool for human liver diseases in the future.

2. The oxidative stress of hepatocytes during liver injury has been quantified *in vivo* using MPM-FLIM (**Chapter 4**). Oxidative stress reflects an imbalance between reactive oxygen species (ROS) and antioxidants. It is an early unifying event in the development and progression of various diseases and as a direct and mechanistic indicator of treatment response. The oxidative stress endpoints can report early and molecular changes induced by treatment, and have potential to serve as powerful biomarkers of drug response. However, highly reactive and short-lived nature of ROS and antioxidant limited conventional detection agents, which are influenced by many interfering factors. In **Chapter 4**, the fluctuations of cellular oxidative stress were visualised during liver injury at the single cell-level resolution using MPM after injection of specific ROS and GSH detection probes. By combining fluorescence intensity imaging and FLIM, the changes of ROS and GSH levels in the injured liver were accurately mapped and quantified without

any possibility of crosstalk from in vivo environmental or instrumental factors. Changes in cellular ROS and GSH precede changes in conventional biochemical and histological assessments in two distinct experimental murine models of liver injury. Therefore, monitoring cellular oxidative stress using MPM-FLIM has significant implications for high-accurate, spatially configured and quantitative assessment of metabolic status and drug response.

3. The *in vivo* fate of administered mesenchymal stem cells (MSCs) has been visualised using MPM to predict the treatment efficacy of liver cirrhosis (**Chapter 5**). A physiologically-based kinetic model was developed to characterise the disposition of administered MSCs based on direct visualization of cell spatiotemporal disposition by MPM. This model was further validated with multiple external datasets, indicating potential inter-route and inter-species predictive capability. These results suggest that the targeting efficiency of MSCs is determined by the lung retention and interaction between MSCs and target organs, including cell arrest, depletion and release. By adapting specific parameters, this model can be easily applied to abnormal conditions or other types of circulating cells for designing treatment protocols and guiding future experiments.

6.2 Future Directions

A better understanding of the liver anatomy, physiology and pharmacology is necessary for developing new diagnostic and therapeutic strategies for liver diseases. This fundamental knowledge can be obtained using various techniques, among which the dynamic imaging tools provided by MPM has emerged as a very powerful option to researchers. FLIM adds the abilities of MPM to detect environmental changes and differentiate fluorophores from biological background according to their lifetimes. Limited infiltration depth is one of the most significant limitations of MPM. Normally, the imaging depth is hundreds of micrometers in MPM. Thus early diseases arising deep in the liver tissue are difficult to be diagnosed with this technique. We anticipate that in the near future the penetration depths of MPM will be further increased, and new infrared dyes will be developed with longer excitation wavelengths that penetrate more deeply due to less absorption and scattering.

Although most of the aforementioned researches are based on animal studies, MPM has already been applied to clinical settings to diagnose and assess liver diseases [1]. Miniaturised laser scanning microscope has been developed, which allows minimal invasive imaging of the liver through keyhole incisions [2]. Endoscope coupled with MPM

has also been developed, which can image the liver through small surgical incision or intrahepatic bile duct as endoscopic retrograde cholangiopancreatography [3]. These minimal invasive imaging techniques have provided the possibility of *in vivo* imaging the human liver. Therefore, we anticipate that in the near future MPM will be evaluated from bench to bedside, and especially be applied to endoscopic or laparoscopic systems, leading to a deep understanding of the anatomy, physiology and pharmacology of the human liver.

References

[1] Gailhouste L, Le Grand Y, Odin C, Guyader D, Turlin B, Ezan F, et al. Fibrillar collagen scoring by second harmonic microscopy: A new tool in the assessment of liver fibrosis. J Hepatol. 2010;52:398-406.

[2] Alencar H, Mahmood U, Kawano Y, Hirata T, Weissleder R. Novel multiwavelength microscopic scanner for mouse imaging. Neoplasia. 2005;7:977-83.

[3] Kim P, Puoris'haag M, Cote D, Lin CP, Yun SH. In vivo confocal and multiphoton microendoscopy. J Biomed Opt. 2008;13.

.

Appendices

Appendix 1

PBK model code for intravenous injection of MSCs in Chapter 5

```
STARTTIME= 0
STOPTIME=24
DTMAX = 0.0005
DTOUT =0.01

; Physiological constants
BW   = 0.02                ; body weight kg

;dose
IV = 500000

{-------Organ volumes as percentages of body weight BW---------}
VLC=0.0549                          ; Liver volume fraction; Brown et al, 1997
VLuC=0.007                          ; Lung volume fraction; Brown et al, 1997
VBoC=1-(VLC+VKC+VSC+VBloodC)    ; Body volume fraction
VKC=0.0167                          ; Kidney volume fraction; Brown et al. 1997
VSC=0.005           ; Spleen volume fraction; Calculated from Davies and Morris 1993
VHC=0.004           ; Heart volume fraction; Calculated from Davies and Morris 1993
VBloodC=0.085         ; Blood volume fraction; Calculated from Davies and Morris 1993

{------------Organ volumes (L)-------------------}
VBlood=VBloodC*BW
VL=VLC*BW     ; Liver
VLu=VLuC*BW   ; Lung
VS=VSC*BW   ; Spleen
VBo=VBoC*BW   ; Muscle (Body)
VK=VKC*BW   ; Kidney
VH=VHC*BW   ; Heart
VA = 0.2*VBloodC*BW                         ; arterial blood
VV = 0.8*VBloodC*BW                         ; venous blood

; Organ blood Volumes
VLuVES = 0.5*Vlu                    ; lung (L)
VLVES = 0.31*VL                             ; liver (L)
VSVES = 0.17*VS                             ; spleen (L)
VKVES = 0.24*VK                             ; kidney (L)
VHVES = 0.26*VH                             ; heart (L)
VBoVES = 0.04*VBo     ; body (L)

QCC=16.5; Cardiac output constant, calculated from Davies and Morris, 1993

{--------Blood flow to organs/tissues as percentages of cardiac output QCC------}
QLC=0.161                   ; Liver blood flow fraction; Brown et al, 1997.
QKC=0.091                   ; Kidney blood flow fraction; Brown et al, 1997
QSC=0.01125                  ; Spleen blood flow fraction; calculated from Davies and Morris, 1993
QHC=0.035                   ; Heart blood flow fraction; Brown et al, 1997
QBoC=1-(QLC+QSC+QKC+QHC)        ; Body blood flow fraction; this compartment designated "Body"

{------------Organ/tissue blood flows (L/hr)------------------}
```

```
QC=QCC*BW^0.75
QLu=QC                  ; Lung
QL=QLC*QC               ; Liver
QS=QSC*QC               ; Spleen
QBo=QBoC*QC             ; Body
QH=QHC*QC               ; Heart
QK=QKC*QC               ; Kidney

; Physico-chemical parameters
PLu = 742.733           ; lung:blood
PL = 262.699            ; liver:blood
PS = 1633.24            ; spleen:blood
PK = 305.351            ; kidney:blood
PH = 3.097              ; heart:blood
PBo = 6.765             ; body:blood

; Biochemical parameters (elimination rate constant)

KBelimination = 0.636
KLuelimination = 0.0589
KLelimination = 0.06
KSelimination = 0.002
KKelimination = 0.151
KHelimination = 0.039
KBoelimination = 0.148

; Biochemical parameters (capillary related constant)

KLuCAPrelease = 0.108    ; Lung
KLuCAPentrap = 5.434
KLCAPrelease = 0.066     ; Liver
KLCAPentrap = 1.395
KSCAPrelease = 0.856     ; Spleen
KSCAPentrap = 0.608
KKCAPrelease = 0.054     ; Kidney
KKCAPentrap = 1.727
KHCAPrelease = 0.016     ; Heart
KHCAPentrap = 1.251
KBoCAPrelease = 0.957    ; Body
KBoCAPentrap = 0.143

; Venous blood concentration
d/dt (AV)  = (QL*CVL+ QS*CVL + QK*CVK + QH*CVH + QBo*CVBo)-(QC*CV) - KBelimination*VV*CV
init AV = IV
CV = AV/VV

; Arterial blood concentration
d/dt (AA)  = QC*(CVLu-CA)
init AA = 0
CA = AA/VA

; Lung
d/dt (ALuVES) = QLu*(CV-CVLu) + KLuCAPrelease*ALuCAP - KLuCAPentrap*ALuVES
init ALuVES = 0
CLuVES = ALuVES/VLuVES
CVLu = CLuVES/PLu

d/dt (ALuCAP) = KLuCAPentrap*ALuVES - KLuCAPrelease*ALuCAP - KLuelimination* ALuCAP
init ALuCAP = 0
CLung = (ALuVES+ALuCAP)/VLu
```

```
; Liver
d/dt (ALVES) = QL*CA+QS*CVS-(QL+QS)*CVL + KLCAPrelease*ALCAP - KLCAPentrap*ALVES
init ALVES = 0
CLVES = ALVES/VLVES
CVL = CLVES/PL

d/dt (ALCAP) = KLCAPentrap*ALVES - KLCAPrelease*ALCAP- KLelimination* ALCAP
init ALCAP = 0
CLiver = (ALVES+ALCAP)/VL

; Spleen
d/dt (ASVES) = QS*(CA-CVS) + KSCAPrelease*ASCAP - KSCAPentrap*ASVES
init ASVES = 0
CSVES = ASVES/VSVES
CVS = CSVES/PS

d/dt (ASCAP) = KSCAPentrap*ASVES - KSCAPrelease*ASCAP- KSelimination* ASCAP
init ASCAP = 0
CSpleen = (ASVES+ASCAP)/VS

; Kidney
d/dt (AKVES) = QK*(CA-CVK) + KKCAPrelease*AKCAP - KKCAPentrap*AKVES
init AKVES = 0
CKVES = AKVES/VKVES
CVK = CKVES/PK

d/dt (AKCAP) = KKCAPentrap*AKVES - KKCAPrelease*AKCAP- KKelimination* AKCAP
init AKCAP = 0
CKidney = (AKVES+AKCAP)/VK

; Heart
d/dt (AHVES) = QH*(CA-CVH) + KHCAPrelease*AHCAP - KHCAPentrap*AHVES
init AHVES = 0
CHVES = AHVES/VHVES
CVH= CHVES/PH

d/dt (AHCAP) = KHCAPentrap*AHVES - KHCAPrelease*AHCAP- KHelimination* AHCAP
init AHCAP = 0
CHeart = (AHVES+AHCAP)/VH

; Body
d/dt (ABoVES) = QBo*(CA-CVBo) + KBoCAPrelease*ABoCAP - KBoCAPentrap*ABoVES
init ABoVES = 0
CBoVES = ABoVES/VBoVES
CVBo = CBoVES/PBo

d/dt (ABoCAP) = KBoCAPentrap*ABoVES - KBoCAPrelease*ABoCAP- KBoelimination* ABoCAP
init ABoCAP = 0
CBody = (ABoVES+ABoCAP)/VBo

AT = AV + AA + ALuVES+ALuCAP + ALVES+ALCAP + ASVES+ASCAP + AKVES+AKCAP +
AHVES+AHCAP + ABoVES+ABoCAP

ALu= ALuVES+ALuCAP
AL= ALVES+ALCAP
AS= ASVES+ASCAP
AK = AKVES+AKCAP
AH= AHVES+AHCAP
ABo= ABoVES+ABoCAP
```

Appendix 2

Ethic Approvals

THE UNIVERSITY OF QUEENSLAND
AUSTRALIA

UQ Research and Innovation
Director, Research Management Office
Nicole Thompson

Animal Ethics Approval Certificate

28-Nov-2014

Please check all details below and inform the Animal Welfare Unit within 10 working days if anything is incorrect.

Activity Details

Chief Investigator:	Mrs Camilla Thompson, Mater Clinical School
Title:	Advanced imaging to define hepatic and intestinal drug disposition in aging and liver diseases
AEC Approval Number:	MED/PAH/521/12/NHMRC
Previous AEC Number:	
Approval Duration:	09-Jan-2013 to 09-Jan-2016
Funding Body:	NHMRC
Group:	Health Sciences
Other Staff/Students:	Xin Liu, Lisa Craig, David Liu, Haolu Wang, Corinne Alberthsen, Sandrine Roy, Kim Brindle, Corinne Alberthsen, Xiaowen Liang, Yian Zhu, Washington Jnr Sanchez, Lisa Foster, Michelle Kappler
Location(s):	PA Hospital - Biological Research Facility PA Hospital - PACE Building PA Hospital Translational Research Institute (TRI)

Summary

Subspecies	Strain	Class	Gender	Source	Approved	Remaining
Mice - genetically modified	FVB.129P2-Abcb4tm1Bor/J (Mdr2 -/-)	Adults	Mix	Commercial breeding colony	154	154
Mice - genetically modified	nude	Adults	Male	Commercial breeding colony	20	20
Mice - Inbred	FVB/N	Adults	Male	Commercial breeding colony	38	38
Mice - Inbred	BALB/c	Adults	Male	Commercial breeding colony	170	146
Rats - Inbred	Fischer 344	Adults	Male	Commercial breeding colony	184	184
Rats - Outbred	Wistar	Adults	Male	Commercial breeding colony	246	221

Permits

Provisos

Proviso:
The AEC has directed that the Consultant Veterinarian of the Animal Welfare Unit monitor this project. Please email m.uren@research.uq.edu.au or notify the AWUC on 52713 at least 7 - 10 days before monitoring is required

Approval Details

Description	Amount	Balance

Mice - genetically modified (FVB.129P2-Abcb4tm1Bor/J (Mdr2 -/-), Mix, Adults, Commercial breeding colony)			
20 Dec 2012	Initial approval	90	90
31 Dec 2013	Use in 2013 (from 2014 MAR)	0	90
17 Jul 2014	Mod #12	20	110
17 Jul 2014	Mod #13	20	130
20 Nov 2014	Mod #16	24	154
Mice - genetically modified (nude, Male, Adults, Commercial breeding colony)			
17 Jul 2014	Mod #11	20	20
Mice - Inbred (BALB/c, Male, Adults, Commercial breeding colony)			
20 Dec 2012	Initial approval	138	138
31 Dec 2013	Use in 2013 (from 2014 MAR)	-24	114
17 Apr 2014	Modification #8	12	126
17 Jul 2014	Mod #12	20	146
Mice - Inbred (FVB/N, Male, Adults, Commercial breeding colony)			
20 Dec 2012	Initial approval	30	30
31 Dec 2013	Use in 2013 (from 2014 MAR)	0	30
17 Sep 2014	Mod #14	8	38
Rats - Inbred (Fischer 344, Male, Adults, Commercial breeding colony)			
20 Dec 2012	Initial approval	160	160
31 Dec 2013	Use in 2013 (from 2014 MAR)	0	160
30 Jul 2014	Mod #9	24	184
Rats - Outbred (Wistar, Male, Adults, Commercial breeding colony)			
20 Dec 2012	Initial approval	180	180
31 Dec 2013	Use in 2013 (from 2014 MAR)	-25	155
16 Jan 2014	Modification #4	24	179
20 Mar 2014	Modification #6	16	195
17 Apr 2014	Modification #8	12	207
17 Jul 2014	Mod #14	8	215
10 Oct 2014	Mod #15	6	221

Please note the animal numbers supplied on this certificate are the total allocated for the approval duration

Please use this Approval Number:

1. When ordering animals from Animal Breeding Houses
2. For labelling of all animal cages or holding areas. In addition please include on the label, Chief Investigator's name and contact phone number.
3. When you need to communicate with this office about the project.

It is a condition of this approval that all project animal details be made available to Animal House OIC.
(UAEC Ruling 14/12/2001)

The Chief Investigator takes responsibility for ensuring all legislative, regulatory and compliance objectives are satisfied for this project.

This certificate supercedes all preceeding certificates for this project (i.e. those certificates dated before 28-Nov-2014)

THE UNIVERSITY OF QUEENSLAND
AUSTRALIA

UQ Research and Innovation
Director, Research Management Office
Nicole Thompson

Animal Ethics Approval Certificate

06-Jun-2016

Please check all details below and inform the Animal Welfare Unit within 10 working days if anything is incorrect.

Activity Details

Chief Investigator: Mrs Camilla Thompson, SOMSouthern - Medicine - Princess Alexandra Hospital

Title: Advanced imaging to define hepatic drug disposition in aging and liver diseases

AEC Approval Number: MED/493/15/NHMRC

Previous AEC Number:

Approval Duration: 26-Feb-2016 to 26-Feb-2019

Funding Body: NHMRC

Group: Health Sciences

Other Staff/Students: Xin Liu, Sandrine Roy, Lisa Foster, Lisa Craig, Xiaowen Liang, Michelle Kappler, Brian Tse, Haolu Wang

Location(s): PA Hospital Translational Research Institute (TRI)

Summary

Subspecies	Strain	Class	Gender	Source	Approved	Remaining
Mice - genetically modified	Mdr2 -/-	Adults	Male	Institutional Breeding Colony	87	87
Mice - non genetically modified	FVB/N	Adults	Male	Institutional Breeding Colony	100	100
Mice - non genetically modified	BALB/c nu/nu	Adults	Male	Commercial breeding colony	40	40
Mice - non genetically modified	BALB/c	Adults	Male	Institutional Breeding Colony	30	30
Rats - non genetically modified	Fisher 344	Adults	Male	Institutional Breeding Colony	60	60
Rats - non genetically modified	Wistar	Adults	Male	Commercial breeding colony	10	10

Permits

Provisos

Approval Details

Description	Amount	Balance
Mice - genetically modified (Mdr2 -/-, Male, Adults, Institutional Breeding Colony)		
18 Feb 2016 Initial approval	75	75
1 Jun 2016 Mod #1	12	87

Animal Welfare Unit
UQ Research and Innovation
The University of Queensland

Cumbrae-Stewart Building
Research Road
Brisbane Qld 4072 Australia

+61 7 336 52925 (Enquiries)
+61 7 334 68710 (Enquiries)
+61 7 336 52713 (Coordinator)

animalwelfare@research.uq.edu.au
uq.edu.au/research

Mice - non genetically modified (BALB/c, Male, Adults, Institutional Breeding Colony)		
18 Feb 2016 Initial approval	30	30
Mice - non genetically modified (BALB/c nu/nu, Male, Adults, Commercial breeding colony)		
18 Feb 2016 Initial approval	40	40
Mice - non genetically modified (FVB/N, Male, Adults, Institutional Breeding Colony)		
18 Feb 2016 Initial approval	100	100
Rats - non genetically modified (Fisher 344, Male, Adults, Institutional Breeding Colony)		
18 Feb 2016 Initial approval	60	60
Rats - non genetically modified (Wistar, Male, Adults, Commercial breeding colony)		
18 Feb 2016 Initial approval	10	10

Please note the animal numbers supplied on this certificate are the total allocated for the approval duration

Please use this Approval Number:

1. When ordering animals from Animal Breeding Houses
2. For labelling of all animal cages or holding areas. In addition please include on the label, Chief Investigator's name and contact phone number.
3. When you need to communicate with this office about the project.

It is a condition of this approval that all project animal details be made available to Animal House OIC.
(UAEC Ruling 14/12/2001)

The Chief Investigator takes responsibility for ensuring all legislative, regulatory and compliance objectives are satisfied for this project.

This certificate supercedes all preceeding certificates for this project (i.e. those certificates dated before 06-Jun-2016)

Appendix 3

Copyright License Agreements

Copyright License Agreement 1 for Figure 2.1 in Chapter 2

License Number	3879700357042
License date	Apr 03, 2016
Licensed content publisher	Royal Society of Chemistry
Licensed content title	Journal of materials chemistry. B, Materials for biology and medicine
Licensed content date	Jan 1, 2012
Type of Use	Journal/Magazine
Requestor type	Publisher, not-for-profit
Format	Print, Electronic
Portion	image/photo
Number of images/photos requested	1
Title or numeric reference of the portion(s)	Diagnostic imaging and therapeutic application of nanoparticles targeting the liver
Title of the article or chapter the portion is from	N/A
Editor of portion(s)	N/A
Author of portion(s)	Haolu Wang
Volume of serial or monograph.	3
Page range of the portion	939â□“958
Publication date of portion	2015
Rights for	Main product
Duration of use	Life of current edition
Creation of copies for the disabled	yes
With minor editing privileges	yes

For distribution to	Worldwide
In the following language(s)	Original language of publication
With incidental promotional use	no
The lifetime unit quantity of new product	More than 2,000,000
Made available in the following markets	acadmic
The requesting person/organization is:	Haolu Wang
Order reference number	None
Author/Editor	Haolu Wang
The standard identifier	1
Title	Visualizing liver anatomy, physiology and pharmacology using multiphoton microscopy
Publisher	Wiley-VCH Verlag GmbH & Co. KGaA
Expected publication date	Jun 2016
Estimated size (pages)	10
Total (may include CCC user fee)	0.00 USD

Copyright License Agreement 1 for Figure 2.2 in Chapter 2

Licensed content publisher	Nature Publishing Group
Licensed content publication	Nature Photonics
Licensed content title	Advances in multiphoton microscopy technology
Licensed content author	Erich E. Hoover, Jeff A. Squier
Licensed content date	Jan 31, 2013
Type of Use	reuse in a journal/magazine
Volume number	7
Issue number	2
Requestor type	academic/university or research institute
Format	print and electronic
Portion	figures/tables/illustrations
Number of figures/tables/illustrations	1
High-res required	no
Figures	Figure 2 Typical optical principle of multiphoton systems and imaging modalities.
Author of this NPG article	no
Your reference number	8
Title of the article	Visualizing liver anatomy, physiology and pharmacology using multiphoton microscopy
Publication the new article is in	Journal of Biophotonics
Publisher of your article	Wiley
Author of the article	Haolu Wang
Expected publication date	Jun 2016
Estimated size of new article (number of pages)	10
Total	0.00 AUD

Copyright License Agreement 1 for Figure 2.5 in Chapter 2

License Number	3841301170285
License date	Apr 03, 2016
Licensed content publisher	Elsevier
Licensed content publication	Journal of Hepatology
Licensed content title	Fibrillar collagen scoring by second harmonic microscopy: A new tool in the assessment of liver fibrosis
Licensed content author	Luc Gailhouste,Yann Le Grand,Christophe Odin,Dominique Guyader,Bruno Turlin,Frédéric Ezan,Yoann Désille,Thomas Guilbert,Anne Bessard,Christophe Frémin,Nathalie Theret,Georges Baffet
Licensed content date	March 2010
Licensed content volume number	52
Licensed content issue number	3
Number of pages	9
Type of Use	reuse in a journal/magazine
Requestor type	author of new work
Intended publisher of new work	Wiley
Portion	figures/tables/illustrations
Number of figures/tables/illustrations	2
Format	both print and electronic
Are you the author of this Elsevier article?	No
Will you be translating?	No
Order reference number	25
Original figure numbers	figures 1 and 5
Title of the article	Visualizing liver anatomy, physiology and pharmacology using multiphoton microscopy
Publication new article is in	Journal of Biophotonics
Publisher of the new article	Wiley
Author of new article	Haolu Wang
Expected publication date	Jun 2016
Estimated size of new article (number of pages)	10
Elsevier VAT number	GB 494 6272 12
Permissions price	0.00 AUD
VAT/Local Sales Tax	0.00 AUD / 0.00 GBP
Total	0.00 AUD

Copyright License Agreement 1 for Figure 2.6 in Chapter 2

Licensed content publisher	Oxford University Press
Licensed content publication	Toxicological Sciences
Licensed content title	Low Dose Acetaminophen Induces Reversible Mitochondrial Dysfunction Associated with Transient c-Jun N-Terminal Kinase Activation in Mouse Liver:
Licensed content author	Jiangting Hu, Venkat K. Ramshesh, Mitchell R. McGill, Hartmut Jaeschke, John J. Lemasters
Licensed content date	03/01/2016
Volume number	150
Issue number	1
Type of Use	Journal/Magazine
Requestor type	Academic/Educational institute
Format	Print and electronic
Portion	Figure/table
Number of figures/tables	2
Will you be translating?	No
Author of this OUP article	No
Order reference number	36
Title of new article	Visualizing liver anatomy, physiology and pharmacology using multiphoton microscopy
Publication the new article is in	Journal of Biophotonics
Publisher of new article	Wiley
Author of new article	Haolu Wang
Expected publication date of new article	Jun 2016
Estimated size of new article (pages)	10
Print Run / Circulation	None
Publisher VAT ID	GB 125 5067 30
Total	0.00 USD

Copyright License Agreement 1 for Figure 2.8 in Chapter 2

April 15, 2016

Haolu Wang
School of Medicine
The University of Queensland
37 Kent St.
Brisbane QLD 4102
Australia

Email: h.wang21@uq.edu.au

Dear Dr. Wang:

This is to grant you permission to reproduce the following figure in a review article titled "Visualizing liver anatomy, physiology and pharmacology using multiphoton microscopy" to appear in the *Journal of Biophotonics* (Wiley):

> Figure 4 from Camilla A. Thorling, Lu Jin, Michael Weiss, Darrell Crawford, Xin Liu, Frank J. Burczynski, David Liu, Haolu Wang, and Michael S. Roberts, Assessing Steatotic Liver Function after Ischemia-Reperfusion Injury by In Vivo Multiphoton Imaging of Fluorescein Disposition, *Drug Metab Dispos* January 2015 43:154-162

Permission to reproduce the figure is granted for worldwide use in all languages, translations, and editions, and in any format or medium including print and electronic. The authors and the source of the materials must be cited in full, including the article title, journal title, volume, year, and page numbers.

Sincerely yours,

Richard Dodenhoff
Journals Director

9650 Rockville Pike | Bethesda | MD | 20814-3995
P: (301) 634-7060 | F: (301) 634-7061 | E: info@aspet.org | www.aspet.org

Copyright License Agreement 1 for Figure 2.9 in Chapter 2

License Number	3841310729851
License date	Apr 03, 2016
Licensed Content Publisher	John Wiley and Sons
Licensed Content Publication	Small
Licensed Content Title	Intravital Multiphoton Imaging of the Selective Uptake of Water-Dispersible Quantum Dots into Sinusoidal Liver Cells
Licensed Content Author	Xiaowen Liang,Jeffrey E. Grice,Yian Zhu,David Liu,Washington Y. Sanchez,Zhen Li,Darrell H. G. Crawford,David G. Le Couteur,Victoria C. Cogger,Xin Liu,Zhi Ping Xu,Michael S. Roberts
Licensed Content Date	Dec 15, 2014
Licensed Content Pages	10
Type of use	Journal/Magazine
Requestor type	Author of this Wiley article
Is the reuse sponsored by or associated with a pharmaceutical or medical products company?	no
Format	Print and electronic
Portion	Figure/table
Number of figures/tables	2
Original Wiley figure/table number(s)	Figure 2, 4
Will you be translating?	No
Circulation	50000
Order reference number	61
Title of new article	Visualizing liver anatomy, physiology and pharmacology using multiphoton microscopy
Publication the new article is in	Journal of Biophotonics
Publisher of new article	Wiley
Author of new article	Haolu Wang
Expected publication date of new article	Jun 2016
Estimated size of new article (pages)	10
Requestor Location	Haolu Wang Princess Alexandra Hospital, Woolloongabba, QLD 4102 Brisbane, Australia Attn:
Billing Type	Invoice
Billing address	Haolu Wang Princess Alexandra Hospital, Woolloongabba, QLD 4102 Brisbane, Australia Attn: Haolu Wang
Total	0.00 USD